Monthly Notices of the ROYAL ASTRONOMICAL SOCIETY

MNRAS **544,** 2946–2986 (2025) https://doi.org/10.1093/mnras/staf1798
Advance Access publication 2025 October 20

Prospects for dark matter observations in dwarf spheroidal galaxies with the Cherenkov Telescope Array Observatory

K. Abe,[1] S. Abe,[2] J. Abhir,[3] A. Abhishek,[4] F. Acero,[5,6] A. Acharyya,[7] R. Adam,[8,9] A. Aguasca-Cabot,[10] I. Agudo,[11] A. Aguirre-Santaella,[12] J. Alfaro,[13] R. Alfaro,[14] C. Alispach,[15] R. Alves Batista,[16] J.-P. Amans,[17] E. Amato,[18] G. Ambrosi,[19] D. Ambrosino,[20,21] F. Ambrosino,[22] L. Angel,[23,24] L. A. Antonelli,[22] C. Aramo,[20] C. Arcaro,[25] K. Asano,[2] Y. Ascasibar,[26] L. Augusto Stuani,[27] M. Backes,[28,29] C. Balazs,[30] M. Balbo,[15] A. Baquero Larriva,[31,32] V. Barbosa Martins,[33] J. A. Barrio,[31] L. Barrios-Jiménez,[34] C. Bartolini,[35,36] P. I. Batista,[37] I. Batković,[38] R. Batzofin,[39] J. Becerra González,[34] G. Beck,[40] J. Becker Tjus,[41] W. Benbow,[42] D. Berge,[43,44] E. Bernardini,[38] J. Bernete,[45] A. Berti,[46] B. Bertucci,[19] V. Beshley,[47] P. Bhattacharjee,[48,49] S. Bhattacharyya,[48] C. Bigongiari,[22,50] A. Biland,[3] E. Bissaldi,[51,52] O. Blanch,[53] J. Blazek,[54] G. Bonnoli,[55,56] A. Bonollo,[35,57] Z. Bosnjak,[58] E. Bottacini,[38] M. Böttcher,[29] T. Bringmann,[59] E. Bronzini,[60] R. Brose,[61,62] G. Brunelli,[60] J. Buces Sáez,[31] M. Bunse,[63] L. Burmistrov,[15] M. Burton,[64,65] P. G. Calisse,[66] A. Campoy-Ordaz,[67] B. K. Cantlay,[68,69] G. Capasso,[70] A. Caproni,[71] R. Capuzzo-Dolcetta,[22,72] P. Caraveo,[73] S. Caroff,[49] R. Carosi,[56] E. Carquin,[74] M.-S. Carrasco,[75] E. Cascone,[70] G. Castignani,[60] A. J. Castro-Tirado,[11] D. Cerasole,[36] M. Cerruti,[76] A. Cerviño Cortínez,[31] P. M. Chadwick,[77] Y. Chai,[2] S. Chaty,[76] A. W. Chen,[40] Y. Chen,[78] M. Chernyakova,[61] A. Chiavassa,[79,80] G. Chon,[46] J. Chudoba,[54] G. M. Cicciari,[81,82] A. Cifuentes,[45] C. H. Coimbra Araujo,[83] M. Colapietro,[70] V. Conforti,[60] J. L. Contreras,[31] B. Cornejo,[84] J. Cortina,[45] A. Costa,[85] H. Costantini,[75] G. Cotter,[86] P. Cristofari,[17] O. Cuevas,[87] Z. Curtis-Ginsberg,[88] G. D'Amico,[53] F. D'Ammando,[89] L. David,[44] F. Dazzi,[90] A. De Angelis,[38] M. de Bony de Lavergne,[75] F. De Frondat Laadim,[17] E. M. de Gouveia Dal Pino,[91] B. De Lotto,[92] M. de Naurois,[9] G. De Palma,[36] V. de Souza,[93] R. Del Burgo,[20] L. del Peral,[94] M. V. del Valle,[91] C. Delgado,[45] D. della Volpe,[15] D. Depaoli,[95] T. Di Girolamo,[20,21] A. Di Piano,[60] F. Di Pierro,[79] R. Di Tria,[52] L. Di Venere,[52] S. Diebold,[96] A. Dinesh,[31] J. Djuvsland,[97] A. Donini,[22] J. Dörner,[41] M. Doro,[38★] C. Duangchan,[39] L. Ducci,[96] V. V. Dwarkadas,[98] J. Ebr,[54] C. Eckner,[48] K. Egberts,[39] D. Elsässer,[99] G. Emery,[11] C. Escañuela Nieves,[95] P. Escarate,[100] M. Escobar Godoy,[101] P. Esposito,[57,73] S. Ettori,[60] D. Falceta-Goncalves,[102] E. Fedorova,[22,103] S. Fegan,[9] Q. Feng,[104] G. Ferrand,[105,106] F. Ferrarotto,[107] E. Fiandrini,[19] A. Fiasson,[49] M. Filipovic,[108] V. Fioretti,[60] L. Foffano,[109] G. Fontaine,[9] F. Frías García-Lago,[34] Y. Fukazawa,[110] Y. Fukui,[111] A. Furniss,[101] G. Galanti,[73] G. Galaz,[13] S. Gallozzi,[22] V. Gammaldi,[26,112] S. García Soto,[45] M. Garczarczyk,[44] C. Gasbarra,[22,113] D. Gasparrini,[113] M. Gaug,[67] S. Germani,[19] A. Ghalumyan,[114] F. Gianotti,[60] J. G. Giesbrecht Formiga Paiva,[115] N. Giglietto,[51,52] F. Giordano,[36] R. Giuffrida,[5,116] J.-F. Glicenstein,[84] J. Glombitza,[37] P. Goldoni,[76] J. M. González,[117] J. Goulart Coelho,[118] T. Gradetzke,[99] J. Granot,[119,120] L. Gréaux,[33] D. Green,[121] J. G. Green,[46] G. Grolleron,[49] L. M. V. Guedes,[24] O. Gueta,[122] D. Hadasch,[123] P. Hamal,[54] W. Hanlon,[42] S. Hara,[124] V. M. Harvey,[125] T. Hassan,[45] K. Hayashi,[2,126] B. Heß,[96] L. Heckmann,[46,76] M. Heller,[15] N. Hiroshima,[2,127] B. Hnatyk,[103] R. Hnatyk,[103] D. Hoffmann,[75] W. Hofmann,[95] D. Horan,[9] P. Horvath,[128] D. Hrupec,[129] S. Hussain,[48] M. Iarlori,[130] T. Inada,[2,131] F. Incardona,[85] S. Inoue,[2,132] Y. Inoue,[106,133] F. Iocco,[20,21] A. Iuliano,[20] Jahanvi,[92] M. Jamrozy,[134] P. Janecek,[54] F. Jankowsky,[135] C. Jarnot,[136] I. Jaroschewski,[84] P. Jean,[136] I. Jiménez Martínez,[46] W. Jin,[78] J. Jurysek,[54] O. Kalekin,[37] V. Karas,[137] J. Kataoka,[138] S. Kaufmann,[77] D. Kazanas,[139] T. Keita,[5]

★ E-mail: michele.doro@unipd.it (MD); francesco.saturni@inaf.it (FGS); gonzalo.rodriguez.fernandez@roma2.infn.it (GRF); aldo.morselli@roma2.infn.it (AM)

D. Kerszberg,[16] D. B. Kieda,[104] R. Kissmann,[140] W. Kluźniak,[141] K. Kohri,[142,143] D. Kolar,[48] N. Komin,[40] P. Kornecki,[11] G. Kowal,[102] H. Kubo,[2] J. Kushida,[1] A. La Barbera,[144] N. La Palombara,[73] B. Lacave,[15] M. Láinez,[31] A. Lamastra,[22] J. Lapington,[145] S. Lazarević,[108] J.-P. Lenain,[16] F. Leone,[146] E. Leonora,[82] Y. Li,[147] E. Lindfors,[148] M. Linhoff,[99,122] S. Lombardi,[22,50] F. Longo,[149] R. López-Coto,[11] M. López-Moya,[31] A. López-Oramas,[34] S. Loporchio,[36] J. Lozano Bahilo,[94] H. Luciani,[149] P. L. Luque-Escamilla,[150] E. Lyard,[151] O. Macias,[147] J. Mackey,[62] P. Majumdar,[152] D. Malyshev,[96] D. Mandat,[54] S. Mangano,[45] G. Manicò,[82,146] A. Marchetti,[55] M. Mariotti,[38] I. Márquez,[11] G. Marsella,[81,82] D. Martín Domínguez,[31] G. A. Martínez,[45] M. Martínez,[53] O. Martinez,[153,154] D. Mazin,[2,46] A. J. T. S. Mello,[83,155] J. Méndez Gallego,[11] S. Menon,[22,156] S. Mereghetti,[73] D. M.-A. Meyer,[123] M. Meyer,[157] D. Miceli,[25] M. Miceli,[81,116] M. Michailidis,[158,159] T. Miener,[15] J. M. Miranda,[154,160] A. Mitchell,[37] M. Molero,[34] C. Molfese,[90] M. Molina Delicado,[31] E. Molina,[34] T. Montaruli,[15] A. Moralejo,[53] A. Moreno Ramos,[154] A. Morselli,[113★] E. Moulin,[84] V. Moya Zamanillo,[31] K. Munari,[85] T. Murach,[44] A. Muraczewski,[141] H. Muraishi,[161] T. Nakamori,[162] R. Nemmen,[91,158] J. P. Neto,[23,24] J. Niemiec,[163] D. Nieto,[31] M. Nievas Rosillo,[34] M. Nikołajuk,[164] K. Nishijima,[165] K. Noda,[2,132] D. Nosek,[166] V. Novotny,[166] S. Nozaki,[2] A. Okumura,[167,168] J.-F. Olive,[136] R. A. Ong,[78] R. Orito,[169] M. Orlandini,[60] E. Orlando,[149] S. Orlando,[116] J. Otero-Santos,[11] I. Oya,[45] M. Ozlati Moghadam,[39] A. Pagliaro,[144] M. Palatiello,[22] A. Pandey,[104] G. Panebianco,[60] D. Paneque,[46] F. R. Pantaleo,[51,52] R. Paoletti,[4] J. M. Paredes,[10] N. Parmiggiani,[60] B. Patricelli,[22,170] M. Pech,[54] M. Pecimotika,[53] M. Peresano,[46] A. Pérez Aguilera,[31] J. Pérez-Romero,[48] G. Peron,[18] F. Perrotta,[70] M. Persic,[171,172] O. Petruk,[47,116] F. Pfeifle,[173] E. Pietropaolo,[174] L. Pinchbeck,[30] F. Pintore,[144] G. Pirola,[46] C. Pittori,[22] F. Podobnik,[4] M. Pohl,[39] V. Poireau,[49] V. Pollet,[49] G. Ponti,[55] C. Pozo González,[11] E. Prandini,[38] G. Principe,[149] M. Prouza,[54] E. Pueschel,[33] G. Pühlhofer,[96] M. L. Pumo,[82,146] A. Quirrenbach,[135] S. Rainò,[36] R. Rando,[38] S. Recchia,[18] M. Regeard,[76] A. Reimer,[140] O. Reimer,[140] I. Reis,[84,93] A. Reisenegger,[13,175] W. Rhode,[99] M. Ribó,[10] C. Ricci,[151,176] T. Richtler,[177] J. Rico,[53] F. Rieger,[95] L. Riitano,[88] C. Ríos,[1] V. Rizi,[174] E. Roache,[42] G. Rodríguez-Fernández,[113★] M. D. Rodríguez Frías,[94] J. J. Rodríguez-Vázquez,[45] P. Romano,[55] G. Romeo,[85] J. Rosado,[31] A. Rosales de Leon,[16] G. Rowell,[125] A. Roy,[178] B. Rudak,[141] A. Ruina,[25] E. Ruiz-Velasco,[49] F. S. Queiroz,[23,24] I. Sadeh,[44] L. Saha,[42] H. Salzmann,[101] M. Sánchez-Conde,[26] P. Sangiorgi,[144] H. Sano,[2,179] R. Santos-Lima,[91] V. Sapienza,[81,116] S. Sarkar,[86] F. G. Saturni,[22★] S. Savarese,[70] V. Savchenko,[180] A. Scherer,[181] F. Schiavone,[36] P. Schipani,[70] F. Schussler,[84] D. Sengupta,[65] O. Sergijenko,[103,182,183] V. Sguera,[60] H. Siejkowski,[184] G. Silvestri,[38] A. Simongini,[90,156] C. Siqueira,[185] V. Sliusar,[151] I. Sofia,[79,95] H. Sol,[17] D. Spiga,[55] S. Spinello,[85] A. Stamerra,[22,121] S. Stanič,[48] T. Starecki,[186] R. Starling,[145] T. Stolarczyk,[5] Y. Suda,[110] H. Tajima,[167,168] M. Takahashi,[167] R. Takeishi,[2] S. J. Tanaka,[187] L. A. Tejedor,[31] M. Teshima,[46] V. Testa,[22] W. W. Tian,[2,188] L. Tibaldo,[136] O. Tibolla,[77] S. J. Tingay,[189] F. Tombesi,[113,156] D. Tonev,[190] F. Torradeflot,[45,191] D. F. Torres,[123] N. Tothill,[108] A. Tramacere,[151] P. Travnicek,[54] A. Trois,[192] S. Truzzi,[4] A. Tutone,[144] M. Vacula,[54,128] C. van Eldik,[37] J. Vandenbroucke,[88] V. Vassiliev,[78] M. Vázquez Acosta,[34] M. Vecchi,[193] S. Ventura,[56] S. Vercellone,[55] G. Verna,[4] I. Viale,[79] A. Viana,[93] N. Viaux,[194] A. Vigliano,[92] J. Vignatti,[194] C. F. Vigorito,[79,80] E. Visentin,[79,80] V. Vitale,[113] V. Voitsekhovskyi,[15] S. Vorobiov,[48] G. Voutsinas,[15] R. Walter,[151] M. Wechakama,[68,69] M. White,[125] A. Wierzcholska,[163] F. Wohlleben,[95] F. Xotta,[48] R. Yamazaki,[187] Y. Yao,[1] T. Yoshikoshi,[2] D. Zavrtanik,[48] M. Zavrtanik,[48] A. Zech,[17] W. Zhang,[123] V. I. Zhdanov,[103] M. Živec[48] and J. Zuriaga-Puig[26]

Affiliations are listed at the end of the paper

Accepted 2025 October 13. Received 2025 October 13; in original form 2025 August 27

ABSTRACT

The dwarf spheroidal galaxies (dSphs) orbiting the Milky Way are widely regarded as systems supported by velocity dispersion against self-gravity, and as prime targets for the search for indirect dark matter (DM) signatures in the GeV-to-TeV γ-ray range owing to their lack of astrophysical γ-ray background. We present forecasts of the sensitivity of the forthcoming Cherenkov Telescope Array Observatory (CTAO) to annihilating or decaying DM signals in these targets. An original selection of candidates is performed from the current catalogue of known objects, including both classical and ultrafaint dSphs. For each, the expected DM content is derived using the most comprehensive photometric and spectroscopic data available, within a consistent framework of analysis. This approach enables the derivation of novel astrophysical factor profiles for indirect DM searches, which are compared with results from the literature. From an initial sample of 64 dSphs, eight promising targets are identified – Draco I, Coma Berenices, Ursa Major II, Ursa Minor, and Willman 1 in the North, Reticulum II, Sculptor, and Sagittarius II in the South – for which different DM density models yield consistent expectations, leading to robust predictions. CTAO is expected to provide the strongest limits above ∼10 TeV, reaching velocity-averaged annihilation cross sections of $\sim 5 \times 10^{-25}$ cm^3 s^{-1} and decay lifetimes up to $\sim 10^{26}$ s for combined limits. The dominant uncertainties arise from the imprecise determination of the DM content, particularly for ultrafaint dSphs. Observation strategies are proposed that optimize either deep exposures of the best candidates or diversified target selections.

Key words: radiation mechanisms: non-thermal – methods: numerical – galaxies: dwarf – Local Group – dark matter – gamma-rays: galaxies.

1 INTRODUCTION

The existence of dark matter (DM; e.g. G. Bertone & D. Hooper 2018, for an historical perspective) in our Universe is well established, but its nature is at present still unknown. Astrophysical observations suggest that the matter in the Universe consists not only of particles of the standard model (SM) of particle physics, but also new non-baryonic particle candidates that must be advocated (e.g. J. L. Feng 2010). Observations of galaxy cluster dynamics and mergers (e.g. D. Clowe et al. 2006; D. Harvey et al. 2015) and galactic rotation curves (e.g. T. S. van Albada & R. Sancisi 1986; F. Lelli, S. S. McGaugh & J. M. Schombert 2016), primordial light element abundances left over by the big bang nucleosynthesis (Particle Data Group 2020; see also F. Iocco et al. 2009), or the spectral shape of the cosmic microwave background (Planck Collaboration I 2014) point to a substantial fraction – around 85 per cent (Planck Collaboration XIII 2016) of the Universe's matter density – being in a form of matter that does not interact significantly with SM particles. Numerical simulations of large-scale structures also support this conclusion, requiring non-relativistic (cold) DM in order to be consistent with observations (see e.g. M. Cirelli, A. Strumia & J. Zupan 2024, and references therein).

For a long time, supersymmetry (SUSY, e.g. J. M. Maldacena 1998) has been generally accepted as a promising extension of the SM, since it naturally solves the hierarchy problem at the same time providing a *natural* DM candidate with its lightest supersymmetric particle (LSP). The LSP has the characteristics of a weakly interacting massive particle (WIMP). One prototypical WIMP particle is the lightest neutralino. The characteristic feature of WIMPs is that they were in thermal equilibrium with ordinary matter in the early universe, but acquired an abundance from thermal freeze-out that matches the observed DM abundance. The minimal SUSY standard model (MSSM; e.g. H. Baer & X. Tata 2022) is a useful framework with which to test current ideas about detection, both in DM direct- or indirect-detection experiments. This model contains many features which are expected to be universal for any WIMP model. WIMP DM candidates also appear in many non-SUSY extensions to the SM – e.g. little Higgs models (e.g. A. Birkedal et al. 2006) or universal extra dimensions (e.g. D. Hooper & S. Profumo 2007). However, simplified templates that rely only on a few free parameters, like the constrained MSSM (G. Jungman, M. Kamionkowski & K. Griest 1996) or the minimal supergravity (L. Alvarez-Gaumé, J. Polchinski & M. B. Wise 1983), are already strongly constrained with data from the Large Hadron Collider (LHC; T. Aaltonen et al. 2012; V. Khachatryan et al. 2015; G. Aad et al. 2016). These results hint at pushing the DM mass scale up to the TeV and multi-TeV range, where particles belonging to the WIMP family such as the wino (J. Hisano, S. Matsumoto & M. M. Nojiri 2004; M. Beneke et al. 2016) or the Higgsino (N. Arkani-Hamed & S. Dimopoulos 2005) are plausible DM candidates.

In these frameworks, WIMPs can pair-annihilate (Y. B. Zeldovich et al. 1980) or decay (A. Ibarra, D. Tran & C. Weniger 2013). Both scenarios would lead to the generation of SM products that in turn generate final-state photons in the γ-ray domain (L. Bergström, P. Ullio & J. H. Buckley 1998). Coupled with the hypothesized DM thermal production mechanisms and the limits on the age of the Universe, respectively, this would yield a DM velocity-averaged annihilation cross section $\langle \sigma_{ann} v \rangle \sim 2/3 \times 10^{-26}$ cm^3 s^{-1} (the so-called thermal relic cross-section; B. W. Lee & S. Weinberg 1977; P. Gondolo & G. Gelmini 1991; G. Steigman, B. Dasgupta & J. F. Beacom 2012; J. Smirnov & J. F. Beacom 2019), respectively, a lifetime at least larger than the *Hubble* time for decaying DM. A debated claim for detection of γ-rays from DM interactions towards the Galactic Centre (GC) direction has been made in the $1 - 60$ GeV energy range, thanks to the availability of deep data from the Large Area Telescope on board of the *Fermi* Gamma-ray Space Telescope (Fermi-LAT; T. Daylan et al. 2016; M. Ackermann et al. 2017); however, despite a thorough modelling of the expected DM emission from the innermost regions of the Milky Way (MW) halo (F. Calore, I. Cholis & C. Weniger 2015; I. Cholis et al. 2022), the interpretation of this GeV excess as a WIMP signal is still controversial (E. Carlson & S. Profumo 2014; J. Petrović, P. D. Serpico & G. Zaharijaš 2014; Q. Yuan & B. Zhang 2014; I. Cholis et al. 2015; R. Bartels, S. Krishnamurthy & C. Weniger 2016; S. K. Lee et al. 2016; S. Abdollahi et al. 2017; O. Macias et al. 2018).

The potential production of γ-ray signals thus makes DM indirectly detectable through appropriate astronomical facilities, including satellite-borne pair-production experiments (e.g. *Fermi*-LAT in the MeV–GeV regime), ground-based imaging atmospheric Cherenkov telescopes in the TeV regime (IACTs; e.g. M. de Naurois & D. Mazin 2015) and shower front detector in the TeV–PeV regime – e.g. the High-Altitude Water Cherenkov (HAWC)

Observatory, the Large High-Altitude Air Shower Observatory (LHAASO), or the future Southern Wide-Field Gamma-ray Observatory (SWGO). Focus of this work are IACTs, which detect very-high energy (VHE; >100 GeV) γ-rays through the Cherenkov emission in particle showers generated in the Earth's atmosphere by through-going γ-rays (T. C. Weekes et al. 1989). DM searches in VHE γ-rays have been carried out in the past decades with all of the major existing IACTs – the Major Atmospheric Gamma-ray Imaging Cherenkov (MAGIC) Telescopes, the High Energy Stereoscopic System (H.E.S.S.), and the Very Energetic Radiation Imaging Telescope Array System (VERITAS) – in the energy range 0.1/100 TeV (see M. Doro, M. A. Sánchez-Conde & M. Hütten 2021; M. Hütten & D. Kerszberg 2022; A. Montanari & E. Moulin 2024, for a recent comprehensive review of all these observations). The construction of the next-generation IACT array, the Cherenkov Telescope Array Observatory (CTAO[1]), will allow more sensitive searches for γ-ray emission from annihilating or decaying DM for WIMP in this range.

A wide DM-oriented program is considered for CTAO (CTAO Consortium 2019), diversified on several targets:

(i) the GC, and in general, the entire MW halo with a very high DM content ($\gtrsim 10^{12}$ $M_\odot$; F. Iocco & M. Benito 2017; E. V. Karukes et al. 2020, but see T. Lacroix et al. 2016; G. Iorio et al. 2023), is the closest known DM target; these characteristics point towards a relatively high DM signal (see Section 2) and were investigated in CTAO Consortium (2021b);
(ii) the most nearby galaxy clusters are suited for the searches of γ-ray signals from DM decay; CTAO prospects were investigated in CTAO Consortium (2024b);
(iii) the Large Magellanic Cloud (LMC), the largest disrupted satellite galaxy of the MW and one of the closest DM-dominated targets, whose CTAO prospects were investigated in CTAO Consortium (2023);
(iv) narrow-line emission associated to specific DM annihilation or decay modes that are incontrovertible signatures of DM, for which CTAO prospects were investigated in CTAO Consortium (2024a).

In this work, we focus on the dwarf spheroidal galaxies (dSphs; see, e.g. L. E. Strigari et al. 2008; L. Mayer 2010; A. W. McConnachie 2012). In contrast to regions already known for hosting γ-ray emitting sources from ordinary astrophysics processes, such as the GC, galaxy clusters, and the LMC, dSphs are in fact almost completely free of any significant background (but see R. M. Crocker et al. 2022), thus making a γ-ray detection from their direction a highly compelling signature for evidence of DM annihilation or decay in their DM haloes.

The Lambda (Λ)-CDM model (A. G. Riess et al. 2004), where CDM stands for 'cold dark matter', predicts that the formation of visible structures has been guided by gravitational accretion of baryons onto previously formed hierarchical DM overdensities – from MW-sized haloes to satellite subhaloes – whose subsequent evolution occurred in different ways. In particular, at galactic and subgalactic scales, the process depends on the initial DM halo parameters, such as the halo mass and the mass density profile, the evolution history, and conditions set by the local galactic environment in which this evolution takes place (see e.g. E. Bertschinger 1998, and references therein). As a result, less massive DM clumps could have evolved into invisible objects, constituting at present DM overdensities purely observable in γ-rays or secondary CRs emerging from CDM interactions. While in principle secondary emission from inverse Compton or synchrotron scattering processes (dependent on ambient photons and magnetic fields, respectively) could produce diffuse multiwavelength (MWL) signatures, classic MWL survey techniques have not been proven sufficiently sensitive for their detection yet (see e.g. A. Kar et al. 2019, and references therein). On the other hand, the subhaloes that were sufficiently massive for accreting enough baryons to initiate star formation have evolved into the variety of satellite galaxies that we actually observe in the MW halo; in this scenario, in-falling baryonic matter settling into the innermost parts of the most massive DM subhaloes could have originated the dSphs (L. E. Strigari et al. 2008).

First discovered in 1938 (H. Shapley 1938), the dSphs are galaxies supported against gravity by the stellar velocity dispersion, possessing a spherical or elliptical appearance and containing $\mathcal{O}(10^2)$ stars (the so-called ultrafaint dSphs) up to $\mathcal{O}(10^7)$ stars (the 'classical' dSphs; A. W. McConnachie 2012). The most striking property of the dSphs is related to their matter content, which appears strongly dominated by the DM content, as opposed to the baryonic content. If in fact such systems are old enough to be in gravitational equilibrium – typically reached in ∼100 Myr (M. G. Walker et al. 2009c) – and following the virial theorem[2] and assuming spherical symmetry and isotropic velocity distribution, one gets a total gravitational mass $M_{\rm tot}$ that is proportional to both the system's virial size $R_{\rm vir}$ and the measured radial velocity dispersion[3] σ_r of their components:

$$M_{\rm tot} = 3\frac{R_{\rm vir}\sigma_r^2}{G}\,, \tag{1}$$

where G is the gravitational constant. The mass derived in this way is ∼10 to $\gtrsim$1000 times larger than that obtainable from the integrated dSph luminosity, which implies mass-to-light ratios $10\ M_\odot/L_\odot \lesssim M/L \lesssim 10^4\ M_\odot/L_\odot$; in contrast, a baryon-dominated system would exhibit $M/L < 10\ M_\odot/L_\odot$ at most (see A. W. McConnachie 2012, and references therein). This places the dSphs among the most DM-dominated objects in the local Universe; however, they are rather light in terms of absolute amount of DM hosted in their haloes ($M_{\rm tot} \lesssim 10^8\ M_\odot$) if compared to e.g. the GC, and their distances are typically larger than that of the GC (∼10 kpc), ranging from few tens to hundreds of kpc. Ultrafaint dSphs share properties with globular clusters, but with more compact size and lower luminosity. Due to their strong gravitational potential, they retain material ejected by stars, resulting in a stellar population with wider metallicity spread than globular clusters (B. Willman & J. Strader 2012).

To date, there are more than 50 MW satellites classified as dSphs, with many of them already targeted as DM sources by current IACTs (M. Doro et al. 2021; M. Hütten & D. Kerszberg 2022). Some of them were observed over several hundreds of hours (see e.g. V. A. Acciari et al. 2022), with no detection achieved. Thanks to the availability of data from recently concluded (E. Sánchez & DES Collaboration 2016) and current survey projects (A. Drlica-Wagner et al. 2016), the number of known confirmed dSphs and candidates is expected to increase with time to >200 objects in the next years. In this work, we present updated determinations of the CTAO performance in detecting the expected photon yield emitted by DM annihilation or decay in dSph haloes. Such prospects are based on novel calculations of the DM amount in the most promising dSphs,

[1]See www.ctao.org for details.

[2]Note, however, that the large velocity dispersion measured in these objects might be biased, leading to significant overestimates of the virial mass (see e.g. M. G. Walker, M. Mateo & M. G. Olszewski 2009a; M. G. Jones et al. 2021; C. Pianta, R. Capuzzo-Dolcetta & G. Carraro 2022).
[3]Assuming a perfectly spherical symmetry, one gets $\sigma_{\rm tot}^2 = 3\sigma_r^2$.

Table 1. Parameters of the Northern (CTAO-N) and Southern (CTAO-S) baseline installations of CTAO (the so-called `Alpha` configuration) of relevance for this work.

	CTAO-N	CTAO-S
Location	ORM	Cerro Paranal
Latitude	28°45′ N	24°41′ S
Altitude	∼2200 m	∼2150 m
Energy threshold	0.02 TeV	0.07 TeV
Angular resolution at 1 TeV	0.058°	0.055°
Energy resolution at 1 TeV	8 per cent	7 per cent
Sensitivity at 1 TeV (50 h)	1.8×10^{-13} erg cm^{-2} s^{-1}	1.3×10^{-13} erg cm^{-2} s^{-1}
Total no. of telescopes	13	51
Number of LSTs	4	0
Number of MSTs	9	14
Number of SSTs	0	37

Notes. ORM stands for Observatorio del Roque de los Muchachos (La Palma, Spain), whereas Paranal stands for the Cerro Paranal observing site (Chile). The information presented here, retrieved from publicly available data (the so-called `prod5` performance release; CTAO Consortium 2021a), may be subject to updates as the telescope layout and data pipelines are being fine-tuned.

taking advantage of the availability of stellar velocity measurements and robust mathematical procedures such as the Jeans analysis of the kinematics of their member stars (N. W. Evans, F. Ferrer & S. Sarkar 2004), which we apply following V. Bonnivard et al. (2015a).

CTAO will be a world-class instrument to perform VHE γ-ray astronomy and will be composed of two arrays of telescopes, one in the Northern hemisphere (CTAO-N) and one in the Southern hemisphere (CTAO-S). Table 1 reports some basic facts about these two installations which are hereafter shortly discussed.[4] CTAO-N will be located in the *Roque de los Muchachos* Observatory (ORM; 28°45′ N 17°53′ W, 2396 m a.s.l) in La Palma (Canary Islands, Spain). The site already hosts the MAGIC telescopes as well as several other installations.[5] Due to its location, CTAO-N is best suited for off-Galactic plane observations, in particular of extra-Galactic targets. For this reason, it is sensitive to the lowest energies – of the order of ∼20 GeV – achievable with the Cherenkov technique. This is obtained with two classes of telescopes of different size: the Large-Sized Telescopes (LSTs), which have 23-m diameter parabolic dishes (LST Coll. 2019), and the Medium-Sized Telescopes (MSTs), equipped with Davies–Cotton dishes of 12-m diameter (J. A. Barrio et al. 2020). Both telescopes have tessellated primary mirrors and photomultiplier (PMT) based focal plane instrumentation. There are currently 4 LSTs and 9 MSTs planned for construction in CTAO-N (so-called `Alpha` configuration, R. Zanin et al. 2022).

CTAO-S will be located close to the ESO Paranal site in Chile (24°41′ S 70°18′ W, 2635 m a.s.l.), near the ESO VLT (Very Large Telescope) and E-ELT (European Extremely Large Telescope) facilities. The location grants an optimal view of the GC and Galactic plane. To detect γ-rays from PeV cosmic-ray and γ-ray sources in the Galaxy (the so-called PeVatrons; e.g Z. Cao et al. 2021; E. de Oña Wilhelmi et al. 2024), CTAO-S requires an improved sensitivity in the highest achievable energies – up to $\mathcal{O}(100)$ TeV: this is obtained through a sparse array, covering ∼km^2 area, of Small-Sized Telescopes (SSTs), 4-m diameter Schwarzschild–Couder telescopes with segmented primary mirrors, monolithic secondary mirrors and silicon-photomultiplier-based focal plane instrumentation (G. Tagliaferri et al. 2022).

The exact characteristic of the arrays are still being fine-tuned. This, along with evolving event reconstruction tools, determines its expected performance.[6] The most up-to-date expected performance of CTAO is publicly released in the form of FITS and ROOT instrument response functions (IRFs; CTAO Consortium 2021a) that are intended to be used together with the CTAO public analysis pipeline software GAMMAPY (F. Acero et al. 2024) for estimating the CTAO capabilities in detecting γ-ray signals from several classes of VHE emitters. Besides the sensitivity, the most important instrumental characteristics which affects the searches for DM signals are: (i) the energy resolution, that determines the ability to discriminate a potential DM spectrum from an astrophysical one, and (ii) the angular resolution, which allows better discrimination of regions with higher DM content. Above 1 TeV, both CTAO-N and CTAO-S have energy resolutions of the order of 6 per cent−7 per cent and angular resolutions of the order of 0.055 − 0.057 deg; both resolutions tend to worsen toward lower energies.

This paper is organized as follows: in Section 2, we present the physical framework for the computation of the expected γ-ray flux from DM annihilation and decay, including a novel computation of the DM content for a selection of best candidate dSphs; in Section 3, we describe the adopted methodology for determining the CTAO sensitivity to indirect DM searches towards in these targets; in Section 4, we present our results for several combinations of important features – spectral models, DM density profile shapes, combining different sources; in Section 5, we compare our findings with the current results from other facilities for γ-ray observations, and discuss them in the context of future surveys aimed at discovering new dSphs; and finally, in Section 6 we give a summary of our work and its main conclusions. Furthermore, Appendix A reports further details on the computation of the DM content in dSphs and Appendix B outlines a quantitative study of the systematics.

2 THE γ-RAY FLUX FROM ANNIHILATING AND DECAYING DARK MATTER IN DSPH HALOES

The expected γ-ray flux (Φ_γ) from DM annihilation and decay processes depends on the microscopic nature of the DM particle, often called the particle-physics factor (discussed in Section 2.1), and on a model for the astrophysical DM distribution – the so-called astrophysical factor[7] (discussed in Section 2.2, N. W. Evans et al. 2004). While the former factor is calculable within a general particle-physics DM framework, the computation of the astrophysical factor requires supporting astrophysical data. We briefly describe our method for estimating the amount of DM in dSph haloes in Section 2.2, focusing on the main concepts; further details are deferred to Appendix A.

[4]The interested reader may find a complete report on CTAO in CTAO Consortium (2013).

[5]See https://www.iac.es/en/observatorios-de-canarias/roque-de-los-muchachos-observatory for details.

[6]We recommend to check https://www.cta-observatory.org/science/cta-performance/ for updates.

[7]This is true in the case of velocity-independent DM interactions, and should be modified if e.g. the Sommerfeld effect (N. Arkani-Hamed et al. 2009; J. L. Feng et al. 2010) or higher partial waves (p- and d-wave) are relevant. In such cases, equation (2) should be replaced by a formulation with a velocity-weighed astrophysical factor.

Depending on the case of annihilating or decaying DM particles, two different expressions define the expected Φ_γ:

$$\frac{\mathrm{d}\Phi_\gamma}{\mathrm{d}E_\gamma} = \begin{cases} \dfrac{\langle\sigma v\rangle}{8k\pi\, m_{\rm DM}^2} \sum_i \mathrm{BR}_i \dfrac{\mathrm{d}N_\gamma^i}{\mathrm{d}E_\gamma} \cdot J_{\rm ann}(\Delta\Omega) & \text{Annihilating DM} \\ \dfrac{1}{4\pi\, m_{\rm DM}} \sum_i \Gamma_i \dfrac{\mathrm{d}N_\gamma^i}{\mathrm{d}E_\gamma} \cdot J_{\rm dec}(\Delta\Omega) & \text{Decaying DM} \end{cases} \quad (2)$$

In the above expressions, $m_{\rm DM}$ the DM particle mass, $\langle\sigma v\rangle$ is the velocity-averaged DM annihilation cross-section in case of annihilating DM, BR_i is the branching ratio (BR) for the ith SM channel, and $\mathrm{d}N_\gamma^i/\mathrm{d}E_\gamma$ is the number of photons (yield) produced during one annihilation at a given energy E_γ into that channel; $k = 1(2)$ for a Majorana (Dirac) DM particle. In the decay case, $\Gamma_i = 1/\tau_i$ are the decay amplitudes – i.e. the inverse of the particle lifetimes τ_i – for the specific ith channel. The astrophysical factor $J(\Delta\Omega)$ accounts for the signal intensity observable on Earth depending on the density of DM toward a target, integrated over the line of sight (l.o.s.) and the aperture $\Delta\Omega$. We label as $J_{\rm ann}$ the parameter for annihilating DM and $J_{\rm dec}$ that for decaying DM. The two, in turn, take the explicit form:

$$J(\Delta\Omega) = \begin{cases} J_{\rm ann}(\Delta\Omega) = \int_{\Delta\Omega} \int_{\rm l.o.s.} \rho_{\rm DM}^2(\ell, \Omega)\, \mathrm{d}\ell\, \mathrm{d}\Omega & \text{Annihilating DM} \\ J_{\rm dec}(\Delta\Omega) = \int_{\Delta\Omega} \int_{\rm l.o.s.} \rho_{\rm DM}(\ell, \Omega)\, \mathrm{d}\ell\, \mathrm{d}\Omega & \text{Decaying DM} \end{cases} \quad (3)$$

For distant objects, the two integrals in equation (3) reduce to volume integrals over the source halo divided by the squared distance (see e.g. equation 4.3 from T. Bringmann, M. Doro & M. Fornasa 2009). There are therefore four factors that affect the signal for DM annihilation or decay: $m_{\rm DM}$, $\langle\sigma v\rangle$ (or $1/\tau_i$), $\mathrm{d}N_\gamma^i/\mathrm{d}E_\gamma$ and $J_{\rm ann}$ (or $J_{\rm dec}$). Out of these, the WIMP mass $m_{\rm DM}$ and the (differential) number of particles per annihilation or decay process $\mathrm{d}N_\gamma/\mathrm{d}E_\gamma$ are defined by the DM particle model. Since $J_{\rm ann}$ or $J_{\rm dec}$ linearly increases the signal yield, it is of utmost relevance to clearly assess the magnitude of the astrophysical factor in order to infer DM properties from positive detection, or to provide strong constraints in case of null detection. We discuss the computation of these factors in Section 2.1 (particle-physics factor) and Section 2.2 (astrophysical factor), respectively.

2.1 Dark matter particle models

Primary products of the WIMP annihilation and decay processes are SM particles such as quarks, gauge bosons, or leptons. After production, quark and bosons hadronize and then decay, generating neutral pions which in turn decay into photons with continuous energies up to $m_{\rm DM}$ for DM annihilation, or up to half this value for DM decay. Regardless the specific SM channel, the γ-ray spectra expected in these cases are very similar. For leptonic decay modes, π^0 are only found for $\tau^+\tau^-$ final states, and most photons are produced as final-state radiation directly off the leptons. We note that the BR_i defined in equation (2) may in principle depend on the incoming DM kinetic energy, but this contribution is subdominant and is neglected here.[8]

A widely used parametrization of DM γ-ray spectra is that provided by M. Cirelli et al. (2011, also called PPPC4 DM ID, hereafter PPPC), that computes γ-ray spectra for different DM masses including electroweak corrections. PPPC is adopted as the reference parametrization for this work; however, one should notice that, for WIMPs different from an electroweak singlet or where virtual internal bremsstrahlung effects are relevant (T. Bringmann et al. 2017), the PPPC parametrization is less accurate. The same is also true for DM particles with $m_{\rm DM} \gg 10$ TeV. Furthermore, PPPC relies on the `PYTHIA` event generator, which exhibits known discrepancies with respect to other generators such as `Herwig` (J. A. R. Cembranos et al. 2013). Recently, refined computations of $\gamma-$ray spectra were explored (e.g. C. W. Bauer, N. L. Rodd & B. R. Webber 2021; C. Arina et al. 2024); however, these new parametrization should have a minor impact on our results, and limited to DM mass values above 10 TeV.

The resulting spectral energy distribution is normally discriminated between a continuous part and a line-like one, the latter arising in processes like DMDM $\rightarrow \gamma\gamma$ or DMDM $\rightarrow \gamma Z_0$. Such a line-like emission would produce an almost monochromatic signal, broadened by the mass of the neutral particle but mostly by the finite energy resolution of the instrument. Line-like signals constitute a clear DM identification, because there is hardly an astrophysical process able to mimic such spectral shapes of the emission, at these energies. However, primary γ-rays can only be produced via second-order loop processes, which are typically reduced by α^2 (α being the fine-structure constant) with respect to the cross-section expected from thermal freeze-out (T. Bringmann & C. Weniger 2012). The search for narrow-line DM signatures in CTAO is investigated in another work (CTAO Consortium 2024a); here, we focus on continuous γ-ray spectra.

The validity of the WIMP freeze-out scenario relies upon the assumption of explaining the observed DM abundance at present day through an (inverse) annihilation process (M. Srednicki, R. Watkins & K. A. Olive 1988; P. Gondolo & G. Gelmini 1991); nevertheless, here we test both the WIMP annihilation and decay possibilities. Furthermore, since each DM model has its γ-ray spectrum defined by equation (2), the overall spectral shape of the annihilation (decay) signal is determined by the branching ratios BR_i (decaying amplitudes Γ_i) to the specific SM channels. In principle, to cast a limit on such models one should know all BR_i (or Γ_i) together with the γ-ray yields for each channel. Knowing all BR_i requires a complete modelling of the DM particle interactions, which is in general useful only if a specific DM particle rather than a class are searched for; it is therefore convenient, and has become a practice in the field, to use a 'benchmark' approach in which one selectively sets $\mathrm{BR}_i = 1$ for the ith channel and zero for all other channels (or $\Gamma_j = 0$ for all channels $j \neq i$ in the case of DM decay).

Widely used spectra in the literature are those corresponding to DM annihilation (or decay) into the $b\bar{b}$, W^+W^-, $\tau^+\tau^-$, and $\mu^+\mu^-$ channels; we display some of the corresponding photon yields for the annihilating DM case for a DM particle of 0.5, 5, and 50 TeV mass in Fig. 1. Changes in the WIMP mass introduce small modifications in the spectral shape of the resulting DM photon yield, although this may not be general. Two of the spectra plausibly bracket the uncertainty on the true annihilation: the $b\bar{b}$ spectrum is a prototype of a soft DM spectrum that peaks at $E_\gamma \sim m_{\rm DM}/20$, while the $\tau^+\tau^-$ spectrum is a prototype of a hard DM spectrum which peaks at $E_\gamma \sim m_{\rm DM}/3$. Some other spectra are shown in Fig. 1 for comparison. PPPC provides such γ-ray spectra for a large set of DM masses. Similar considerations hold for the decaying DM case where the cut-off happens at $m_{\rm DM}/2$, but the spectral shape is preserved.

2.2 Modelling of the astrophysical factor and selection of the optimal dSphs

The procedure for estimating the DM astrophysical factor of a dSph has an ample literature. Different methods and assumptions lead to

[8] In the case of CDM with typical velocities $v \sim 10^{-3}c$ and s-wave annihilation, the kinetic energy of the incoming DM particles is of order $\sim 10^{-6} m_{\rm DM}$, resulting in changes to the branching ratios of $\lesssim$1 per cent except near sharp kinematic thresholds or resonances.

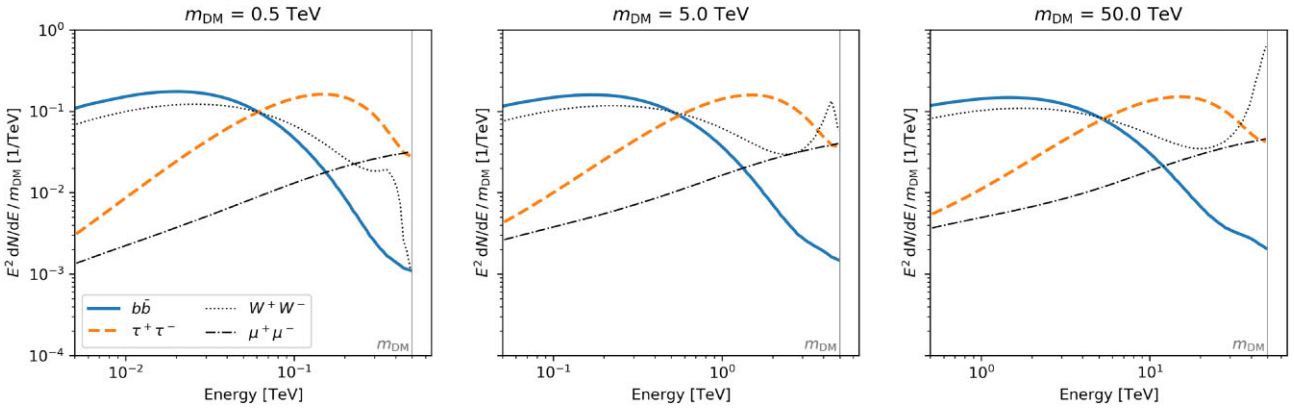

Figure 1. DM γ-ray spectra as a function of the DM mass for pure WIMP annihilation into specific channels, obtained with GAMMAPY (F. Acero et al. 2024) and based on the PPPC parametrization by M. Cirelli et al. (2011). We compare three values of $m_{\rm DM} = 0.5,\ 5,$ and 50 TeV (grey solid lines) to show that the photon yield and spectral differences as a function of the mass are minor, with the exception of the W^+W^- where electroweak loop corrections and final-state radiation significantly affect the high-energy tail of the spectrum. The $b\bar{b}$ and $\tau^+\tau^-$ channels are selected as representative examples of the theoretical DM photon yields, the former being the softest with a signal peak at $m_{\rm DM}/20$ and the latter being the hardest with a peak at $m_{\rm DM}/3$. In the case of DM decay, the major difference is that the cut-off happens at $m_{\rm DM}/2$ – while preserving the spectral shape.

mild incompatibilities (in most cases) or vigorous ones for some debated targets. This computation becomes particularly relevant for the case of CTAO which, as opposed to other wide field of view (FoV) instruments, will only be able point to a selection of dSphs for deep observations, very likely starting with those with the highest – and possibly most accurately determined – predicted values of the astrophysical factor. Considering the relevance of the astrophysical factor for the computation of detection limits of γ-ray signals from DM annihilation or decay (see equation 2), we provide our own estimates based on a consistent treatment of all the dSphs considered here.

Previous attempts to compute the astrophysical factor for large samples of dSphs can be found in the literature (N. W. Evans et al. 2004; V. Bonnivard et al. 2015b; A. Geringer-Sameth, S. M. Koushiappas & M. Walker 2015; G. D. Martinez 2015; K. Hayashi et al. 2016). In these works, the authors adopted a variety of methods to determine $J_{\rm ann}$ and $J_{\rm dec}$ of dSphs from observed quantities (e.g. surface brightness and stellar kinematics). For instance, L. E. Strigari et al. (2008) perform maximum-likelihood fits to the dSph stellar l.o.s. velocities to derive scale densities, radii, and indices of the DM haloes; A. Geringer-Sameth et al. (2015) apply the agnostic modelling of DM density profiles from stellar spectrophotometric data also described in A. Charbonnier et al. (2011) and G. D. Martinez (2015) computes DM halo parameters through hierarchical mass modelling of dSphs; finally, V. Bonnivard et al. (2015b) and K. Hayashi et al. (2016) rely on different applications of the Jeans analysis to compute posterior distributions of halo parameters from observable data.

Others like e.g. the *Fermi*-LAT-based studies (M. Ackermann et al. 2015; A. Drlica-Wagner et al. 2015a; A. Albert et al. 2017; A. McDaniel et al. 2024), make use of astrophysical factor estimates primarily based on *distance* measurement, using the universality of dSph properties discussed by e.g. L. E. Strigari et al. (2008). This is also motivated by the fact that several dSphs in the FoV of *Fermi*-LAT did not have astrometry-based measurements available. M. Ackermann et al. (2015), A. Drlica-Wagner et al. (2015a), and A. Albert et al. (2017) used a relation between $J_{\rm ann}$ and the dSph distance $d_\odot$ with uncertainties up to ∼0.8 dex. More recently, A. B. Pace & L. E. Strigari (2019) introduced a novel scaling relation which not only included the distance, but also the l.o.s. velocity spread σ_v as well as the stellar half-light radius $r_{1/2}$ to more accurately compute the $J_{\rm ann}$ enclosed within 0.5°, obtaining:

$$J_{\rm ann}(<0.5^\circ) = 10^{17.87}\left(\frac{\sigma_v}{5\ {\rm km s^{-1}}}\right)^4\left(\frac{d_\odot}{100\ {\rm kpc}}\right)^{-2}\left(\frac{r_{1/2}}{100\ {\rm pc}}\right)^{-1} \quad (4)$$

with claimed uncertainties on the level of $\lesssim$0.1 dex. Recently, A. McDaniel et al. (2024) used such scaling relations to provide *Fermi*-LAT legacy limits on 50 dSphs, one of the largest sample ever used. In fig. 1 of A. McDaniel et al. (2024), they classify the dSphs in three groups: 'Measured' includes dSphs for which astrometric data are available in the literature, 'Benchmark' includes also the dSphs for which only an estimate of $J_{\rm ann}$ from equation (4) can be obtained, and 'Inclusive' also contains the controversial dSphs. We compare our own catalogue with this work throughout this paper.

Our calculations of the dSph astrophysical factors are based on the procedure described in V. Bonnivard et al. (2015b), that makes use of the publicly available CLUMPY code (A. Charbonnier, C. Combet & D. Maurin 2012; V. Bonnivard et al. 2016a; M. Hütten, C. Combet & D. Maurin 2019). CLUMPY allows the execution of a Markov Chain Monte Carlo (MCMC) dynamical analysis of the dSphs' DM haloes. In detail, the galaxy is treated as a steady-state, collisionless systems in spherical symmetry (but not necessarily isotropic) and with negligible rotation, in which the contribution of the stellar component to the total mass can be also neglected (see V. Bonnivard et al. 2015a, for a comprehensive discussion on these assumptions). The MCMC analysis relies on the solution of the second-order spherical Jeans equation (J. Binney & S. Tremaine 2008):

$$\frac{1}{n^*(r)}\left\{\frac{\rm d}{{\rm d}r}\left[n^*(r)\overline{v_r^2}\right]\right\} + 2\beta_{\rm ani}(r)\frac{\overline{v_r^2}}{r} = -\frac{G}{r^2}\left[M^*(r) + M_{\rm DM}(r)\right] \simeq -\frac{GM_{\rm DM}(r)}{r^2}, \quad (5)$$

where $n^*(r)$ is the stellar number density, $\overline{v_r^2}$ is the average squared radial velocity, and $\beta_{\rm ani}(r) = 1 - \overline{v_\theta^2}/\overline{v_r^2}$ is the velocity anisotropy of the dSph (with $\overline{v_\theta^2}$ the average squared tangential velocity).

Such quantities are fed to CLUMPY as either a parametric fixed input (the stellar number density), a set of discrete input values with which the MCMC is computed (the stellar kinematics data that determine the velocity dispersion) or a set of free parameters that

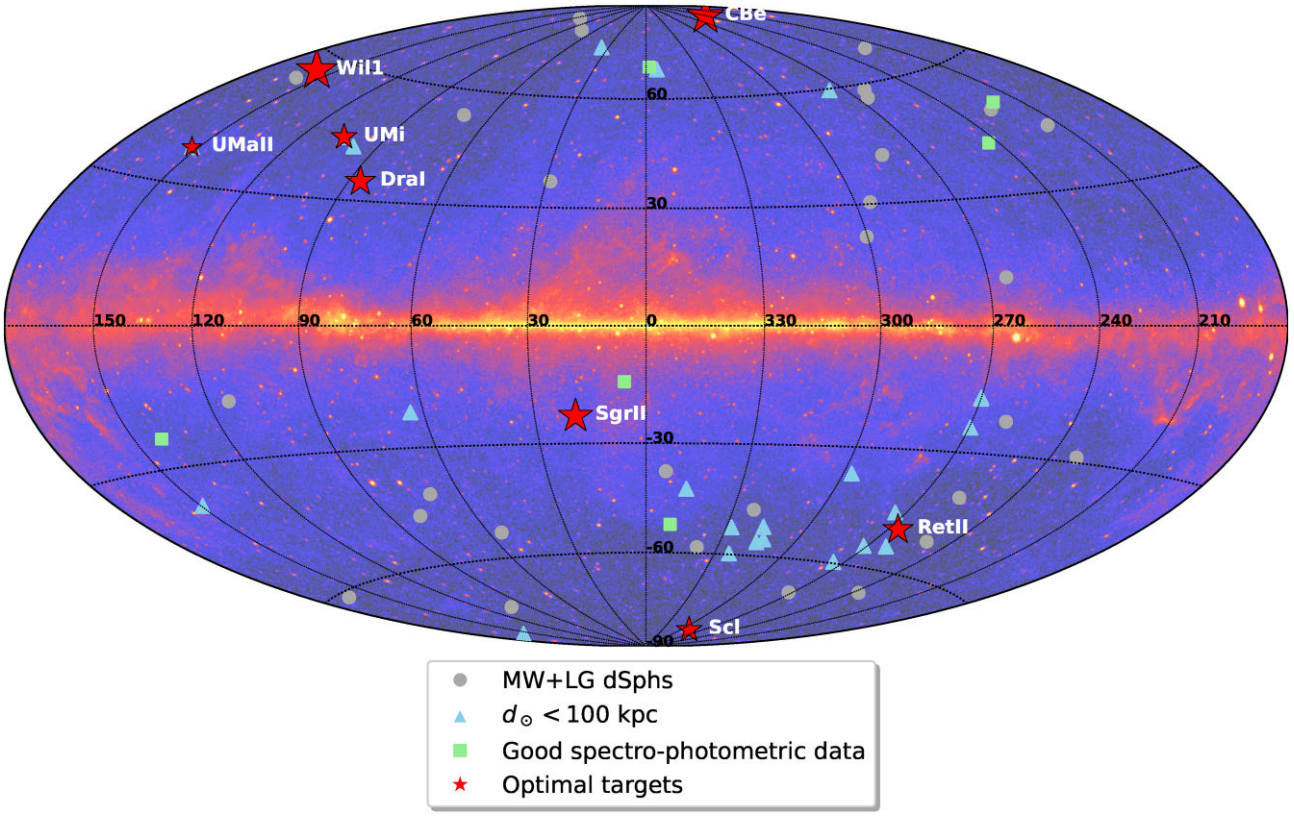

Figure 2. Sky distribution of known MW satellites and LG dSphs, superimposed to the *Fermi*-LAT γ-ray background (credits: NASA/DOE/*Fermi*-LAT Collaboration). All of the targets from Table A1 are reported, along with the sources from Table 2 (i.e. those passing the first selection cut on distance) and those objects passing the second selection (availability of good spectral and photometric data). The optimal targets are highlighted with symbols of increasing size, proportional to the value of their log $J_{\rm ann}(< 0.1^\circ)$ (see Table A5).

describe the adopted profile (the DM density $\rho_{\rm DM}$ and the velocity anisotropy profile). In such conditions, the Jeans equation can be solved to obtain $\rho_{\rm DM}(r)$ along the object's 3D radial coordinate r. The complete procedure that we adopted is described in more details in Appendix A; here, we report the main results, that are based on the use of the best input of dSph currently available in the literature and of the latest CLUMPY version (v3).

2.2.1 *Initial catalogue of dSphs and selection criteria*

We collect from the literature the basic positional data (equatorial coordinates and distance) for a complete sample of MW and Local Group (LG) classical and ultrafaint dSph satellites known to date, merging catalogues of already known targets (A. W. McConnachie 2012) and results from recent surveys (K. Bechtol et al. 2015; A. Drlica-Wagner et al. 2015b, 2020; S. E. Koposov et al. 2015a; B. P. M. Laevens et al. 2015b, a; N. F. Martin et al. 2015). From their equatorial coordinates, we compute the culmination zenith angles (ZAs) of each target in both hemispheres at the CTAO-N and CTAO-S sites. In this way, we identify 64 targets, whose sky distribution is shown in Fig. 2. All dSphs analysed in A. McDaniel et al. (2024) appear in our catalogue. Since it is not possible to accurately model the DM content of all the 64 dSphs (see Appendix A for a discussion), we narrow down the best candidates following consecutive selection steps:

(i) We apply a distance selection $d_\odot \leq 100$ kpc to remove those dSphs for which we expect very low values of $J_{\rm ann}$ based on equation (4) (35 remaining targets).

(ii) For the surviving dSphs, we investigate the availability and quality of spectrophotometric data sets in the literature and discard those with missing or unreliable data (14 remaining targets).

(iii) We select the dSphs with the highest values of $J_{\rm ann}$ for further signal modelling and computation of prospects with CTAO observations (eight remaining targets).

2.2.2 *Distance-based selection*

The first selection is done according to the target distance $d_\odot \leq 100$ kpc, on the basis of the scaling relation equation (4). After the application of this first cut, we end up with 35 remaining candidates, that we report in Table 2, and 29 discarded dSphs that we report in Table A1. We indicate their names with the corresponding abbreviation, the dSph type ('*cls*' for the classical dSphs and '*uft*' for the ultrafaint ones[9]), their J2000 right ascension (RA) and declination (Dec.), their distance, and their culmination ZA ($ZA_{\rm culm}$) at the CTAO-N and CTAO-S sites, together with the culmination month. Out of these, 13 are visible for CTAO-N and 22 for CTAO-S. All the dSphs in our catalogue that were not reported in A. McDaniel et al. (2024) do not pass the distance cut, except for the Sculptor dSph which is excluded by A. McDaniel et al.

[9]This classification is not physical, since it is mostly based on the discovery of dSphs before the SDSS (D. G. York et al. 2000) for the classical objects and after for the ultrafaint targets. However, it is useful to use a crude separation between objects with hundreds to thousands of member stars (the classical dSphs), and few to tens (the ultrafaint case).

Table 2. Basic properties of the MW dSph satellites and those of the LG not associated to major galaxies that satisfy our first selection cut (heliocentric distance <100 kpc), separated between Northern (upper section) and Southern hemisphere (lower section). In both sections, objects indicated with 'cls' are 'classical' dSphs, whereas 'uft' stands for 'ultrafaint', and dashes in the culmination columns indicate objects that do not rise above the horizon for the CTAO array in the relevant hemisphere.

Name	Abbr.	Type	RA (hh mm ss)	Dec. (dd mm ss)	Distance (kpc)	ZA_{culm} N (deg)	ZA_{culm} S (deg)	Month	Ref.
CTAO-N candidate dSphs									
Boötes I	BooI	uft	14 00 06.0	+ 14 30 00	65 ± 3	14.3	39.1	Apr	1,2
Boötes II	BooII	uft	13 58 00.0	+ 12 51 00	39 ± 2	15.9	37.5	Apr	1,3
Boötes III	BooIII	uft	13 57 12.0	+ 26 48 00	46 ± 2	2.0	51.4	Apr	1,3
Coma Berenices	CBe	uft	12 26 59.0	+ 23 54 15	42 ± 2	4.9	48.5	Mar	1,4
Draco I	DraI	cls	17 20 12.4	+ 57 54 55	75 ± 4	29.2	82.5	Jun	1,5
Draco II	DraII	uft	15 52 47.6	+ 64 33 55	20 ± 3	35.8	89.2	May	6
Laevens 3	Lae3	uft	21 06 54.3	+ 14 58 48	67 ± 3	13.8	39.6	Aug	7
Segue 1	Seg1	uft	10 07 04.0	+ 16 04 55	23 ± 2	12.7	40.7	Feb	1,8
Segue 2	Seg2	uft	02 19 16.0	+ 20 10 31	36 ± 2	8.6	44.8	Oct	1,9
Triangulum II	TriII	uft	02 13 17.4	+ 36 10 42	30 ± 2	7.4	60.8	Oct	10
Ursa Major II	UMaII	uft	08 51 30.0	+ 63 07 48	35 ± 2	34.4	87.8	Feb	1,11
Ursa Minor	UMi	cls	15 09 08.5	+ 67 13 21	68 ± 2	38.5	–	May	1,12
Willman 1	Wil1	uft	10 49 21.0	+ 51 03 00	38 ± 7	22.3	75.7	Mar	1,8
CTAO-S candidate dSphs									
Carina II	CarII	uft	07 36 26.3	−58 00 00	36 ± 1	86.7	33.3	Jan	13
Carina III	CarIII	uft	07 38 31.2	−57 54 00	28 ± 2	86.7	33.3	Jan	13
Cetus II	CetII	uft	01 17 52.8	−17 25 12	30 ± 3	46.2	7.2	Oct	14
Eridanus III	EriIII	uft	02 22 45.5	−52 16 48	95 ± 27	81.0	27.7	Oct	15
Grus II	GruII	uft	22 04 04.8	−46 26 24	53 ± 5	75.2	21.8	Aug	14
Horologium I	HorI	uft	02 55 28.9	−54 06 36	87 ± 13	82.9	29.5	Oct	15
Horologium II	HorII	uft	03 16 26.4	−50 03 00	78 ± 8	77.5	26.7	Nov	16
Hydrus I	HyiI	uft	02 29 33.7	−79 18 36	28 ± 1	–	53.3	Oct	17
Indus I	IndI	uft	21 08 48.1	−51 09 36	69 ± 16	79.9	26.5	Aug	15
Phoenix II	PheII	uft	23 39 57.6	−54 24 36	95 ± 18	83.2	29.8	Sep	15
Pictor II	PicII	uft	06 44 43.1	−59 54 00	45 ± 5	88.3	35.8	Jan	18
Reticulum II	RetII	uft	03 35 40.9	−54 03 00	32 ± 2	82.8	29.4	Nov	15
Reticulum III	RetIII	uft	03 45 26.3	−60 27 00	92 ± 13	89.2	35.8	Nov	19
Sagittarius I	SgrI	cls	18 55 19.5	−30 32 43	31 ± 1	59.3	5.9	Jul	1,20
Sagittarius II	SgrII	uft	19 52 40.5	−22 04 05	67 ± 5	50.8	2.6	Jul	7
Sculptor	Scl	cls	01 00 09.4	−33 42 33	84 ± 2	62.5	9.1	Oct	1,21
Sextans	Sex	cls	10 13 03.0	−01 36 53	84 ± 3	30.4	23.0	Feb	1,22
Tucana II	TucII	uft	22 52 16.7	−58 33 36	58 ± 6	87.3	33.9	Sep	15
Tucana III	TucIII	uft	23 56 35.9	−59 36 00	25 ± 2	88.4	35.0	Sep	14
Tucana IV	TucIV	uft	00 02 55.3	−60 51 00	48 ± 4	89.6	36.2	Sep	14
Tucana V	TucV	uft	23 37 23.9	−63 16 12	55 ± 9	–	38.3	Sep	23
Virgo I	VirI	uft	12 00 09.1	−00 40 52	87 ± 11	40.0	24.2	Mar	24

Notes. References: [1]A. W. McConnachie (2012), [2]S. Okamoto et al. (2012), [3]B. Sesar et al. (2014), [4]I. Musella et al. (2009), [5]N. Hernitschek et al. (2016), [6]B. P. M. Laevens et al. (2015b), [7]B. P. M. Laevens et al. (2015b), [8]J. T. A. de Jong et al. (2008), [9]E. Boettcher et al. (2013), [10]B. P. M. Laevens et al. (2015a), [11]M. Dall'Ora et al. (2012), [12]C. Ruhland et al. (2011), [13]G. Torrealba et al. (2018), [14]A. Drlica-Wagner et al. (2015b), [15]K. Bechtol et al. (2015), [16]D. Kim & H. Jerjen (2015), [17]S. E. Koposov et al. (2018), [18]A. Drlica-Wagner et al. (2016), [19]A. Drlica-Wagner et al. (2015b), [20]A. T. Valcheva et al. (2015), [21]C. E. Martínez-Vázquez et al. (2015), [22]G. E. Medina et al. (2018), [23]B. C. Conn et al. (2018), and [24]D. Homma et al. (2016).

(2024) due to source confusion with 4FGL J0059.5−3338, and Triangulum II for the tension between the value of J_{ann} derived from its available astrometric data and that obtained from the distance relations. From fig. 1 of A. McDaniel et al. (2024), we check the conservativeness of this cut by noting that the targets lying right beyond the distance limit (Aquarius II, Carina I, and Ursa Major I) have values of $J_{ann} \lesssim 3 \times 10^{18}$ GeV^2 cm^{-5}. All the farther ones either have $J_{ann} < 10^{18}$ GeV^2 cm^{-5}, or do not posses kinematic data sets. These would not have passed our further selection criteria.

2.2.3 *Stellar data quality selection*

A second step is based on the quality and availability of photometric and spectroscopic data sets, which are required in order to compute well-defined astrophysical factors. The complete methodology is reported in Appendix A and here we only shortly recall that the starting point is obtaining the brightness density profiles $n^*(r)$ of each dSph for which literature data exist. During this step, we discard 16 targets: Boötes III, Carina II, Carina III, Draco II, Laevens 3, Cetus II, Eridanus III, Horologium I, Horologium II, Hydrus I, Indus I, Pictor I, Phoenix II, Reticulum III, Tucana V, and Virgo I, since such targets have no spectroscopic measurements over adequately populated samples of member stars (e.g. A. Koch et al. 2009; S. E. Koposov et al. 2015b; A. Drlica-Wagner et al. 2015a) and we end up with 19 dSphs. The stellar brightness density profiles of these surviving dSphs are then fitted with a 3D ZhaoṇHernquist profile (see Appendix A; L. Hernquist 1990; H. Zhao 1996), projected onto the corresponding circularized 2D surface brightness profile (see Fig. A1); at this level, we remove five additional dSphs – Segue 2, Tucana II, Tucana III, Tucana IV, and

Boötes II – for lacking 2D brightness data (see Appendix A for further details).

We perform such fits using the IDL package MPFIT (C. B. Markwardt 2009); in this way, we are left with a list composed by 14 candidates, reported now in Table 3 along with the number of member stars, the average velocity and spread, and the references for data. We also report our estimation of their tidal radius, discussed below (see also Appendix A2.5). We note that these objects are well distributed between both hemispheres, thus providing CTAO with a balanced pool of choice for both sites. The stellar surface brightness profiles for these targets are reported in Fig. A1. Next, we study the stellar kinematics of the remaining dSphs: to this aim, we collect the most updated and complete samples of stars for each source that are provided in the literature (see references reported in Table 3). The advantage of using such samples lies in their cleanliness from problematic data, e.g. binary stars (M. E. Spencer et al. 2017), thanks to the analyses performed by their respective authors (see e.g. E. N. Kirby et al. 2017). The distribution of stellar velocities for each sample of stars that fall within the sky extension of a given dSph is shown in Fig. A1. For the treatment of the velocity anisotropy, we use the Baes & van Hese profile (see equation A2; M. Baes & E. van Hese 2007). In Table A2, we also report the V-band integrated dSph magnitude, eccentricity, brightness scale radius and density, and the stellar membership statistics for each target.

Lacking any direct information on the DM density distribution in each target, an underlying functional form must be assumed to model its profile. Broadly speaking, there are two classes derived from N-body simulations: a cuspy DM profile – strongly peaked towards the centre – and a cored DM profile – flat towards the centre. We investigate both scenarios, by adopting the Einasto profile (J. Einasto 1965) witht hree free parameters (DM scale density ρ_s, DM scale radius r_s, and DM inner slope α) for the cuspy case, and the Burkert profile (A. Burkert 1995) with two free parameters (scale density and radius) for the cored case:

$$\rho_{\rm DM}(r) = \begin{cases} \rho_s \exp\left\{-\frac{2}{\alpha}\left[\left(\frac{r}{r_s}\right)^{\alpha} - 1\right]\right\} & \text{Einasto} \\ \dfrac{\rho_s}{\left(1+\frac{r}{r_s}\right)\left[1+\left(\frac{r}{r_s}\right)^2\right]} & \text{Burkert} \end{cases} \tag{6}$$

We opt for the Einasto profile as representative of the class of cuspy DM density profiles, since it is known from the literature that different choices of cuspy parametrizations – e.g. the Navarro–Frenk–White (NFW) shape (J. F. Navarro, C. S. Frenk & S. D. M. White 1997) – have no impact on the calculation of $J_{\rm ann}$ and $J_{\rm dec}$ for the case of dSphs (V. Bonnivard et al. 2015b) and, in general, when integrating signals up to angular sizes comparable to the instrumental point spread function (PSF) in the γ-ray energy regime (M. Ackermann et al. 2015).

Due to interaction with the gravitational field of the MW, dSphs are expected to lose the outer rims of the DM halo due to tidal interaction (see e.g. R. Errani et al. 2022). The exact value of the tidal radius is known with some uncertainties and subject to assumptions. As made by V. Bonnivard et al. (2015b), we compute for each dSph the tidal radius $R_{\rm tid}$, iteratively solving the tidal equation (see equation A3, V. Springel et al. 2008; P. Mollitor, E. Nezri & R. Teyssier 2015), and report it for both the Einasto and the Burkert profiles in Table 3. Finally, within the main DM halo of the dSph, smaller DM substructures called DM subhaloes can retain significant amounts of clumped DM. The contribution of DM subhaloes to the total astrophysical factor has been subject to strong debates in the past (M. A. Sánchez-Conde et al. 2011; M. A. Sánchez-Conde & F. Prada 2014; S. Ando, T. Ishiyama & N. Hiroshima 2019); such a contribution can be factorized into a boost factor $\mathcal{B}$ to $J_{\rm ann}$ and $J_{\rm dec}$. $\mathcal{B}$ has the effect of increasing the expected DM γ-ray flux due to inclusion of the contributions from the DM subhaloes within the main halo (see equation A4). Following results in the literature (M. A. Sánchez-Conde & F. Prada 2014; Á. Moliné et al. 2017), we conservatively assume $\mathcal{B} = 0$. A more in-depth discussion is deferred to Appendix A2.6.

2.2.4 *Dark matter density profiles for selected dSphs*

With these ingredients, we are able to compute the parametrized DM density profiles $\rho_{\rm DM}(r)$ for each of the selected dSphs by running 200 independent CLUMPY MC chains of 10^5 realizations each for every target; for all the free parameters considered in the MCMC Jeans analysis, we adopt the conservative priors determined by V. Bonnivard et al. (2015a). Out of the resulting posterior distributions of the fitted parameters, we derive the astrophysical factor profiles for both the Einasto and Burkert DM profiles using equation (3), along with the median value and the corresponding uncertainties at 68 per cent confidence level (CL). The Einasto and Burkert profiles for annihilating and decaying DM can be found in the Online Material (CTAO Consortium 2025). In Fig. 3, we present such DM density profiles for the 14 selected dSphs, for both the Einasto (J. Einasto 1965) and Burkert (A. Burkert 1995) profiles, also displaying the corresponding tidal radii (see equation A3).

Overall, there is a good agreement between the two profiles in the central region before the halo scale radius, with larger discrepancies in the inner regions for the classical dSphs DraI, Sex, and SgrI as well as for the ultrafaint GruII and Seg1 – where the Einasto profile deviates from the central plateau of the Burkert profile – whereas SgrII displays larger differences at the outer radii. We also note that the tidal radii computed for both DM profiles reported in Table 3 always agree well for all of the classical dSphs, and within uncertainties for the ultrafaint ones. In Fig. 4, we report the uncertainty on the tidal radius of CBe and RetII to graphically show this compatibility. The future availability of expanded stellar samples will be crucial to allow more accurate estimates of the gravitational properties of such objects; however, we remark that inaccuracies on the determination of quantities such as tidal radii only have a minor impact on the calculation of $J_{\rm ann}$ and $J_{\rm dec}$, given that the bulk of the expected γ-ray flux comes from the innermost regions of the dSph haloes and the signal saturation has already been reached at the tidal radius.

2.2.5 *Signal robustness selection*

In order to select the most promising dSphs as CTAO targets, we now compute the astrophysical factor following equation (3), which requires a double integral over the DM density profile (square for annihilating DM). We use the CLUMPY methods also to derive these quantities. This allow us to have a sample of astrophysical factor (median and 68 per cent containment values) for 30 equally spaced angular distances from 0.01° to 10°. All such tables are reported in the Online Material (CTAO Consortium 2025). The astrophysical factor profiles of the 14 targets are reported as a function of the instrumental integration angle[10] $\alpha_{\rm int}$ – for both Einasto (cuspy) and Burkert (cored) DM density profiles – in Fig. 4 for the annihilation

[10]Equivalent to a solid angle element $\Delta\Omega = 2\pi(1 - \cos\alpha_{\rm int})$ in equations (2) and (3).

Table 3. Kinematic properties of the dSphs surviving our first and second selection cuts. In the table, we report: the dSph short name; the best CTAO site for observation; the adopted method for the stellar classification – 'EM' denotes the application of the expectation–maximization algorithm by M. G. Walker et al. (2009b) to determine individual stellar membership probabilities, whereas 'bin' indicates the adoption of the binary memberships reported in the literature (see Appendix A); the number of stars surviving the selection over the total number of input stars; the average radial velocity and dispersion; the reference for the stellar kinematic data. We also report the tidal radii computed with CLUMPY assuming two shapes for the DM density profiles.

Name	Site	Membership	$N_{\rm mem}/N_{\rm tot}$	$\langle v_r \rangle$ (km s^{-1})	σ_v (km s^{-1})	Ref.	$R_{\rm tid}^{\rm (Ein)}$ (kpc)	$R_{\rm tid}^{\rm (Bur)}$ (kpc)
BoöI	N	bin	37/113	100.6	4.3	1	$5.1^{+10.7}_{-2.2}$	$15.1^{+30.4}_{-9.6}$
CBe	N	bin	59/102	97.8	5.8	2	$6.3^{+9.5}_{-3.4}$	19^{+55}_{-16}
DraI	N	EM	466/1565	−292.4	9.5	3	$4.83^{+1.16}_{-0.84}$	$4.30^{+0.86}_{-0.54}$
GruII	S	bin	21/235	−109.8	1.8	4	$0.35^{+1.01}_{-0.32}$	$\lesssim 9.5$
RetII	S	bin	18/38	64.0	3.6	5	$1.66^{+4.46}_{-0.97}$	$5.8^{+19.3}_{-5.3}$
Scl	S	EM	1120/1541	111.5	9.1	6	$2.95^{+0.55}_{-0.30}$	$3.71^{+0.30}_{-0.18}$
Seg1	N	EM	154/522	206	15	7	$0.43^{+3.23}_{-0.35}$	$\lesssim 28$
Sex	S	EM	356/947	224	11	6	$7.8^{+4.4}_{-2.9}$	$9.9^{+5.7}_{-3.4}$
SgrI	S	EM	288/503	140	17	8	$1.56^{+0.34}_{-0.73}$	$\lesssim 1.7$
SgrII	S	bin	21/26	−175.7	5.0	9	$3.7^{+13.9}_{-2.7}$	$4.2^{+36.4}_{-2.8}$
TriII	N	bin	13/33	−381.7	2.5	10	$0.36^{+3.20}_{-0.35}$	$\lesssim 56$
UMaII	N	bin	20/54	−116.1	8.1	2	$2.15^{+1.69}_{-0.99}$	$2.23^{+6.48}_{-0.98}$
UMi	N	EM	467/973	−247	12	11	$14.7^{+6.6}_{-4.1}$	$15.3^{+8.6}_{-3.9}$
Wil1	N	bin	40/97	−13.6	6.3	12	$1.20^{+4.08}_{-0.51}$	$1.35^{+26.35}_{-0.48}$

Notes. References: [1]S. E. Koposov et al. (2011); [2]J. D. Simon & M. Geha (2007); [3]M. G. Walker, E. W. Olszewski & M. Mateo (2015a); [4]J. D. Simon et al. (2020); [5]M. G. Walker et al. (2015b); [6]M. G. Walker et al. (2009a); [7]J. D. Simon et al. (2011); [8]R. A. Ibata et al. (1997); [9]N. Longeard et al. (2020); [10]E. N. Kirby et al. (2017); [11]M. E. Spencer et al. (2018); and [12]B. Willman et al. (2011).

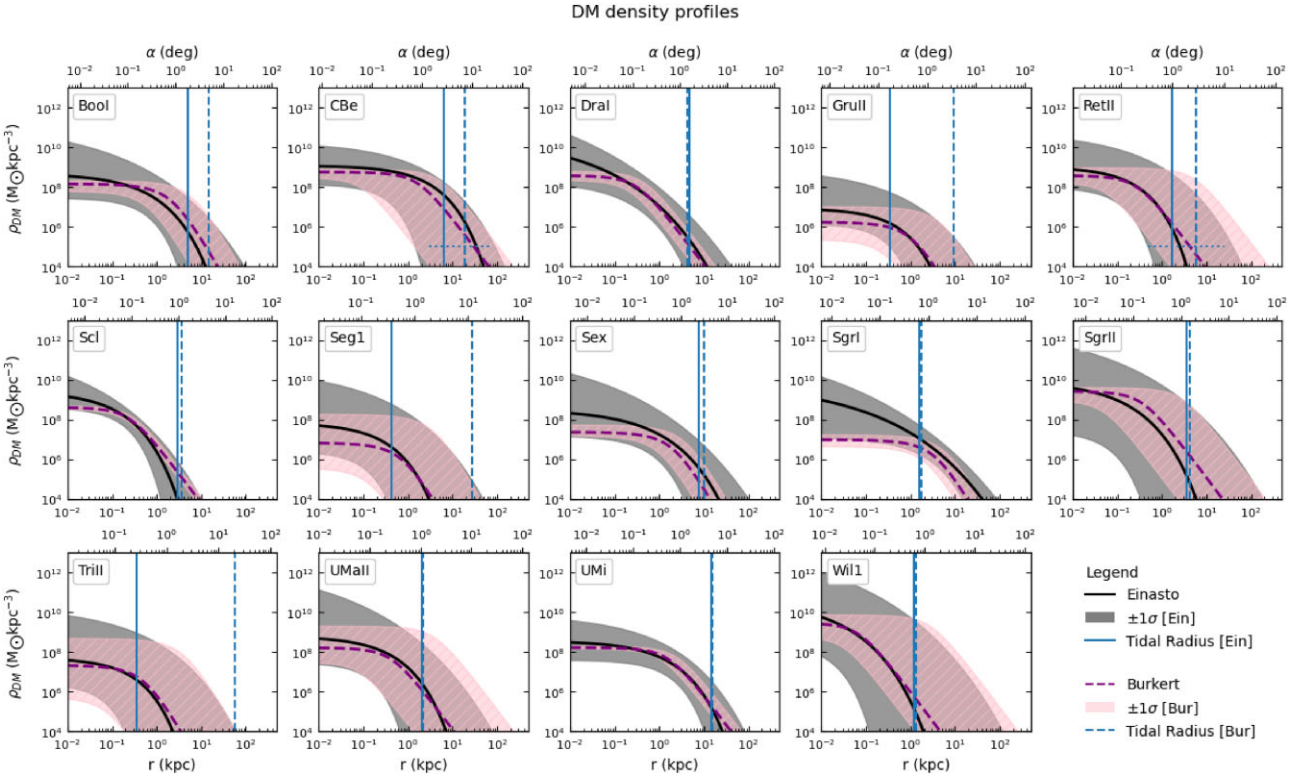

Figure 3. DM density profiles of the 14 optimal dSphs for both cored (A. Burkert 1995) and cuspy models (J. Einasto 1965), along with the corresponding uncertainties at 68 per cent CL . In all panels, the tidal radius (see the text for details) for the Einasto and Burkert profile is also indicated, along with the typical uncertainty for the representative cases of CBe and RetII.

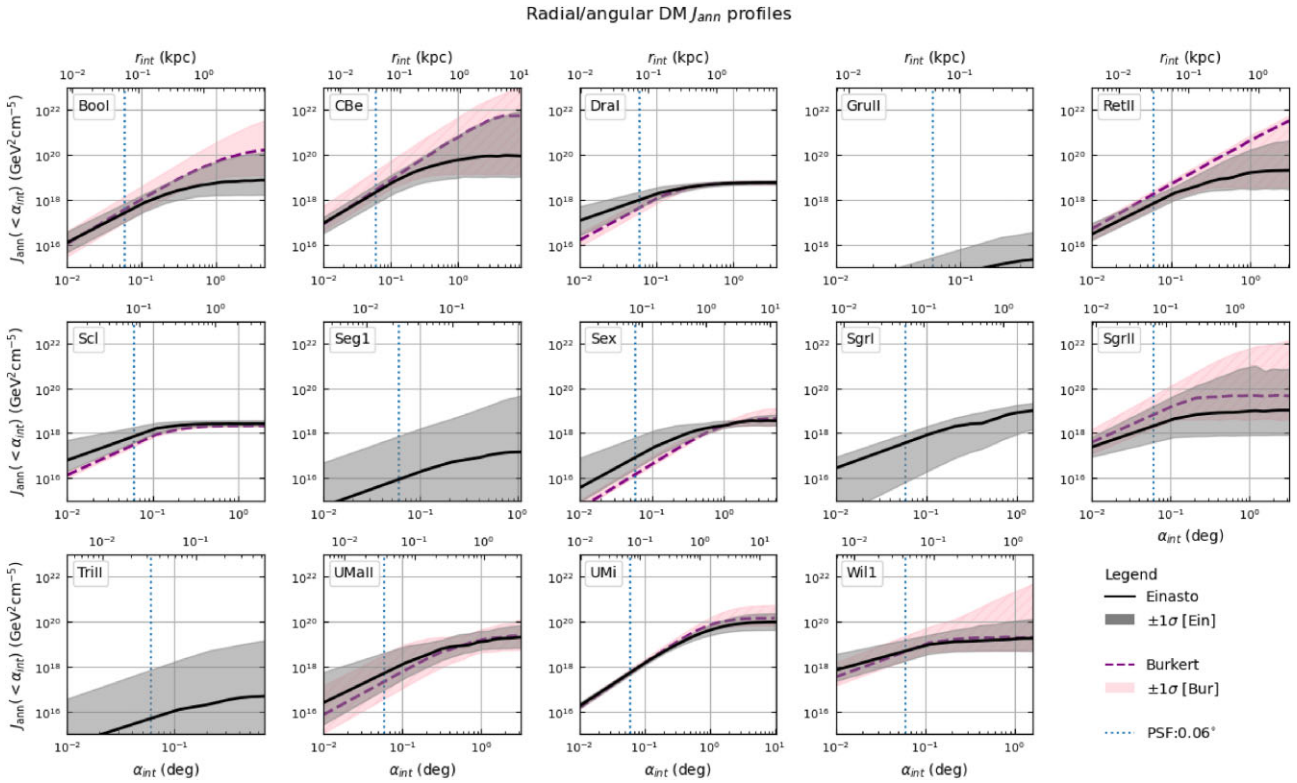

Figure 4. Astrophysical factors for DM annihilation $J_{\rm ann}(<\alpha_{\rm int})$ as functions of the integration angle $\alpha_{\rm int}$ (or the equivalent integration distance from the dSph centroid $r_{\rm int}$) for the best Northern and Southern dSphs. In all panels, the median astrophysical factor profiles for both cuspy (Einasto) and cored (Burkert) DM density profiles are plotted alongside the relative uncertainties at 1σ CL. The integration angles corresponding to an instrumental PSF of 0.06° are also indicated. Each profile is truncated at the corresponding dSph tidal radius for the Einasto profile (see equation A3 and Table A2). The Burkert profiles for GruII, Seg1, SgrI, and TriII are not reported because no finite integration could be obtained.

mode and Fig. 5 for the decay mode. In these figures, we also report the CTAO average angular resolution to show that all targets appear between moderately and very extended if integrated out of their rims.

Figs 4 and 5 show that the median profiles and also their uncertainties do not significantly vary between the two cases of cored and cuspy DM distribution, at least for the classical dSphs DraI and Scl and for the ultrafaint dSphs UMaII, UMi, and Wil1. The similarity between the resulting DM density profiles computed with CLUMPY for different choices of the DM density functional profile shape was already highlighted by V. Bonnivard et al. (2015b) for the class of cuspy profiles – that also comprises those of NFW (J. F. Navarro et al. 1997) and the Zhao–Hernquist one (L. Hernquist 1990; H. Zhao 1996) – and by M. Ackermann et al. (2015) for the class of cored profiles (see their fig. 7). For GruII, Seg1, SgrI, and TriII in the $J_{\rm ann}$ case, with the addition of RetII in the $J_{\rm dec}$ one, we do not report the Burkert profile because of numerical integration failures in the MC chains that prevented us to obtain finite non-null median values of the astrophysical factor. In addition, for CBe and SgrII, we find a bigger discrepancy between the Einasto and Burkert profiles than for the other targets. We argue that such issues could be caused by the MCMC Jeans analysis being unable to correctly fit the stellar velocity dispersion in these targets with a Burkert density profile, due to either choices of non-optimal priors on the free profile parameters (see V. Bonnivard et al. 2015a), or to the data actually preferring a cuspy DM distribution over a cored one (see also Section 4.1). A detailed study of the optimal parameter priors to be associated with each choice of fitting DM density profile is out of scope in this paper, and is therefore deferred to a future publication; here, we focus on those targets whose $J_{\rm ann}$ and $J_{\rm dec}$ profiles do not exhibit features of major integration issues.

Out of the 14 dSphs selected in the previous steps, we further narrow down our choice to the top candidates per site. Such a choice is justified by the reasons that (i) CTAO will not likely observe more than a few candidates in the initial years of observation; (ii) the meaningful targets to be observed are those with the highest – and possibly more precisely determined – astrophysical factors; and (iii) the DM detection limits scale linearly with the astrophysical factor[11] – it is therefore easy to estimate obtainable limits for alternative dSphs by considering the appropriate difference in $J_{\rm ann}$ or $J_{\rm dec}$. Motivated by the fact that the dSphs appear as extended targets with respect to the CTAO angular resolution (see Table 1), we select those dSphs with the highest $J_{\rm ann}(<0.1^\circ)$ and $J_{\rm ann}(<0.5^\circ)$ using the $J_{\rm ann}(<\alpha_{\rm int})$ profiles; out of the two possibilities, we prioritize those objects with $J_{\rm ann}(<0.1^\circ)\gtrsim 10^{18}$ GeV^2 cm^{-5}.

As a result, we find eight dSphs satisfying this criterion; the final sample of most promising dSphs to be observed with CTAO is therefore composed by:

(i) DraI, UMi (classical), CBe, UMaII, and Wil1 (ultrafaints) for CTAO-N;
(ii) Scl (classical), RetII and SgrII (ultrafaints) for CTAO-S.

[11]This is true only at a first approximation, i.e. only in case the acceptance is the same for different targets. Such an assumption is not completely true in case of e.g. targets observed at different ZAs or with different spatial extensions.

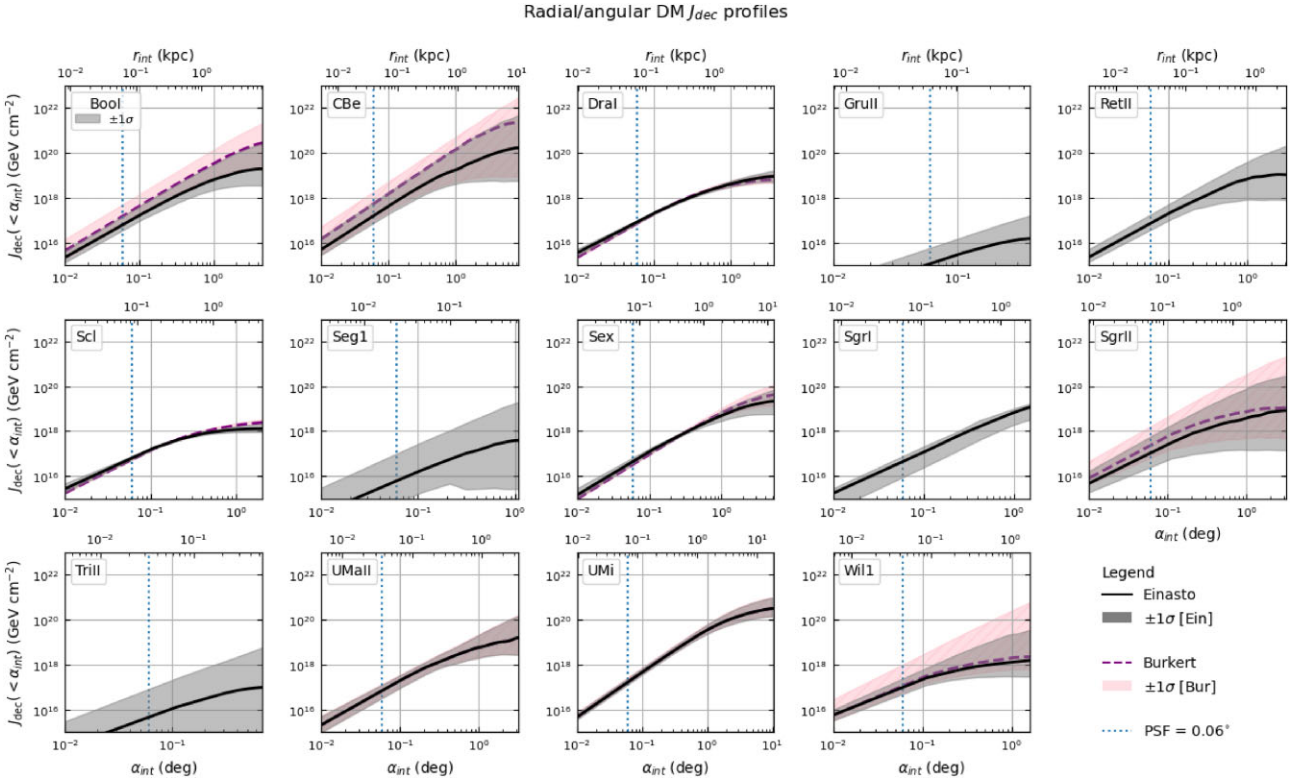

Figure 5. Same as Fig. 4, but for the case of DM decay. In this case, also the Burkert profile for RetII is excluded due to a non-finite integration.

This selection yields the same objects when selecting for either $J_{\rm ann}(<0.1^\circ)$ or $J_{\rm ann}(<0.5^\circ)$, except for BooI – that has $J_{\rm ann}(<0.1^\circ) < 10^{18}$ GeV^2 cm^{-5} – and SgrI – whose $J_{\rm ann}$ profile is however affected by large uncertainties due to its altered stellar dynamics by several gravitational interactions with the innermost regions of the MW potential well. Due to the inclusion of additional targets when integrating up to larger angular sizes, we further investigate the robustness of this selection criterion by performing a scan of additional integration angles, namely 1° and $\alpha_{\rm tid} = \arctan(R_{\rm tid}/{\rm d}_\odot)$. We discuss the ranking for different integration angles in Section A4. In Appendix B2, we also report the amount of change in the expected DM signal intensity when the full DM density profile is integrated taking into account a model for tidal stripping in the dSph halo outer rims (e.g. J. Peñarrubia et al. 2010; R. Errani & J. F. Navarro 2021).

2.2.6 *Comparison with literature results*

In order to validate our results, we perform a comparison with previous literature estimates. Often, solely the astrophysical factors computed through equation (3) at specific integration radii – normally $J(<0.1^\circ)$ or $J(<0.5^\circ)$ – are reported. Only in some cases (e.g. V. Bonnivard et al. 2015a), the full astrophysical profile is reported. For such reasons we show the comparison between our obtained values of $J_{\rm ann}(<0.1^\circ)$ and those from the literature[12] in Fig. 6. This figure reveals a very good agreement between our determinations and those from the literature; furthermore, we are able to provide calculations of $J_{\rm ann}$ and $J_{\rm dec}$ for the recently discovered SgrII dSph that are based on its stellar kinematics – whereas only estimates from scaling relations were previously available for this target (A. McDaniel et al. 2024).

We also confirm that, prior to the analysis by V. Bonnivard et al. (2015c), the astrophysical factor of Seg1 was overestimated by a factor of >100 due to the inclusion in its member sample of the spurious stellar population with $\langle v_r \rangle \sim 300$ km s^{-1} (see Fig. A1). An even more severe overestimation by >4 orders of magnitude was made for TriII, due to poorly determined kinematics of its member stars (E. N. Kirby et al. 2017). The need for selecting clean kinematic samples in dSph haloes to obtain a reliable measurement of the DM amount is well exemplified by the case of SgrI, which would be classified as a DM-dominated source ($J_{\rm ann} \gtrsim 10^{18}$ GeV^2 cm^{-5}; A. Viana et al. 2012; A. Abramowski et al. 2014) if the gravitational disturbance due to its proximity to the dense Galactic bulge were not known (e.g. T. A. A. Venville et al. 2024).

The outer rims of dSphs can in fact be tidally disrupted by the gravitational field of the MW (R. Errani et al. 2022); in particular, the interaction of the dSph haloes with the deepest regions of the Galactic potential spuriously increases the stellar velocity dispersion, often causing its misinterpretation as due to a large DM content (A. Geringer-Sameth et al. 2015). In detail, Table A5 contains at least three debated dSphs, namely SgrI (R. A. Ibata et al. 1997), UMaII (R. R. Muñoz et al. 2010), and Wil1 (B. Willman et al. 2011), in which tidal disruption is potentially underway. Although we are aware that the inclusion of objects with disturbed kinematics due to this process may lead to severely overestimating their DM content, we decide to keep such targets in our final sample to show how this bias affects the analysis in case of disrupted dSphs, with the only exception of SgrI

[12] A comparison between our $J_{\rm ann}(<0.5^\circ)$ estimates and the literature is reported in Fig. A2, and leads to similar conclusions.

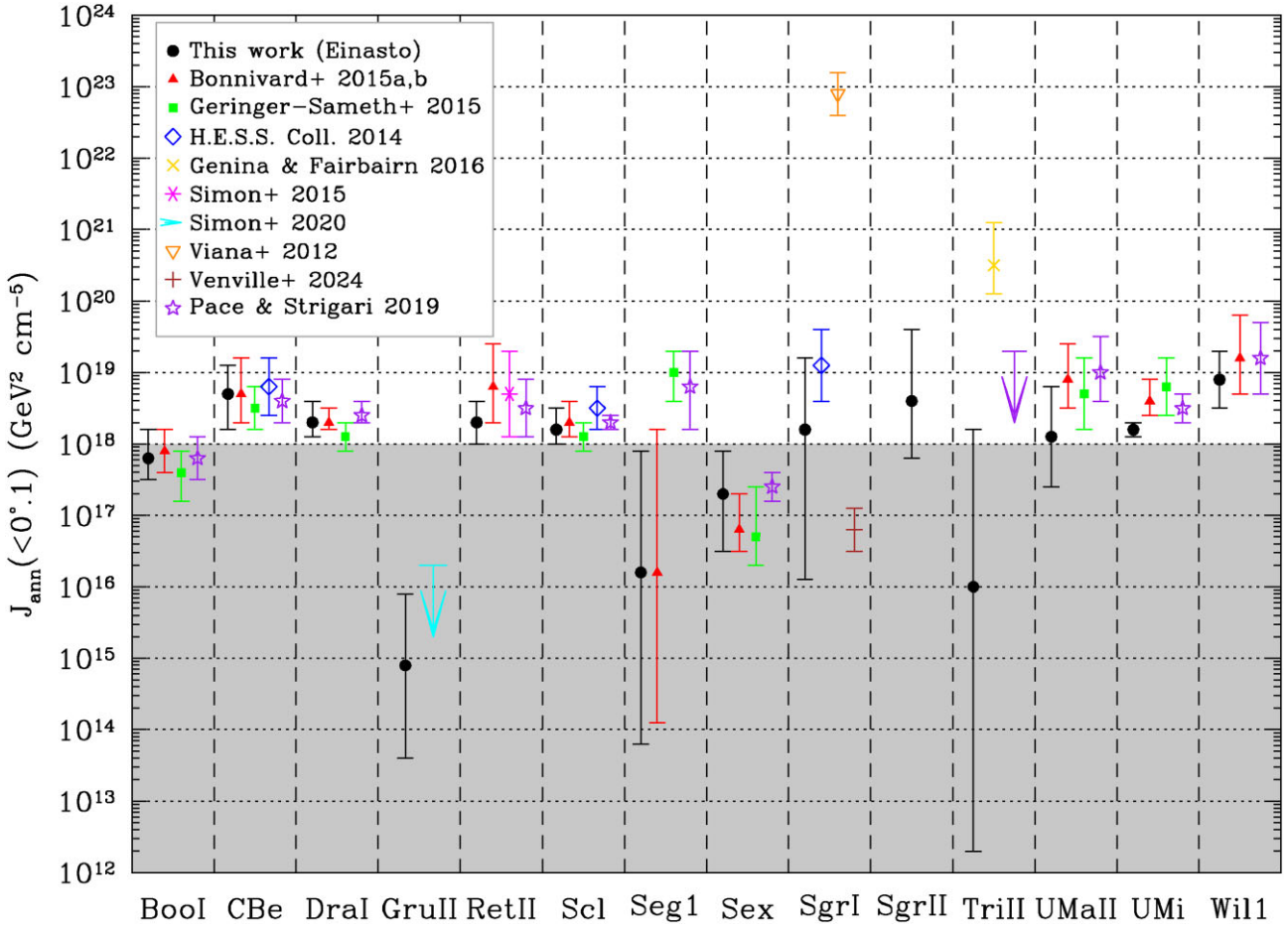

Figure 6. Comparison of the astrophysical factors computed in this work for DM annihilation (Einasto density profile) within 0.1° of integration $J_{\rm ann}(<0.1^\circ)$ (black dots) with similar estimates from the literature (see the legend A. Viana et al. 2012; A. Abramowski et al. 2014; V. Bonnivard et al. 2015b; A. Geringer-Sameth et al. 2015; J. D. Simon et al. 2015, 2020; A. Genina & M. Fairbairn 2016; A. B. Pace & L. E. Strigari 2019; T. A. A. Venville et al. 2024). The range that has been excluded for identifying optimal targets for CTAO based on their $J_{\rm ann}(<0.1^\circ)$ values (grey area) is marked. A similar comparison for $J_{\rm ann}(<0.5^\circ)$ is made in Fig. A2.

due to its (weak) γ-ray background emission[13] potentially associated with canonical astrophysical sources (R. M. Crocker et al. 2022).

Finally, compared to A. McDaniel et al. (2024), our catalogue includes TriII and Scl as mentioned before, but excludes HorI, TucII, DraII, TucIV, HyiI, BooII, and CarII from among their 'Measured' sample. Nevertheless, all these dSphs show low or uncertain values of $J_{\rm ann}$ in their work. We also exclude all of their 'Benchmark' dSphs due to their lack of astrometric data, with the exception of GruII (data from A. Drlica-Wagner et al. 2015b; J. D. Simon et al. 2020). Finally, we remove BooIII, HorII, and VirI with respect to their 'Inclusive' sample again due to missing astrometric data, but we keep SgrI and Wil1 that satisfy our selection cuts (data from S. R. Majewski et al. 2003; R. A. Ibata et al. 1997 and N. F. Martin et al. 2008; B. Willman et al. 2011, respectively).

[13]See CTAO Consortium (2024a) for a detailed discussion of the γ-ray emission from this target. The CTAO capabilities in observing sources lying close to the Galactic plane are presented in CTAO Consortium (2024c).

3 ANALYSIS METHODOLOGY

In order to predict the significance of the γ-ray emission for CTAO pointing at the selected dSphs, we follow methodologies that are commonly adopted in the literature (see e.g. M. Ackermann et al. 2015). We make use of the open source code GAMMAPY V1.2 (F. Acero et al. 2024; A. Donath et al. 2023), which is the official CTAO analysis code and is publicly available together with the up-to-date IRFs (CTAO Consortium 2021a). For this work, we use the PROD5-V0.1 release. IRFs encompass the energy resolution $f_E(E'|E, P)$, the angular resolution $f_P(P'|E, P)$, the effective area $A_{\rm eff}(E, P)$, and the estimated residual background rate. In these definitions, (E, E') stand for true and reconstructed energy, and (P, P') for the true and reconstructed direction. At the moment, all these functions and parameters are estimated via MC simulations of the CTAO detectors, before the actual instruments are built. We also present a cross-check of our results made with the public codes CTOOLS (J. Knödlseder et al. 2016) and SWORDFISH (T. D. P. Edwards & C. Weniger 2017; T. D. P. Edwards & C. Weniger 2018), obtaining compatible results (see Appendix B). The results obtained in this paper are reproducible from the Online Material (CTAO Consortium 2025).

Our analysis defines a signal model following equation (2), assuming $\langle\sigma v\rangle$ or τ as parameter of interest for annihilating or decaying DM models and lognormal uncertainty distributions associated to

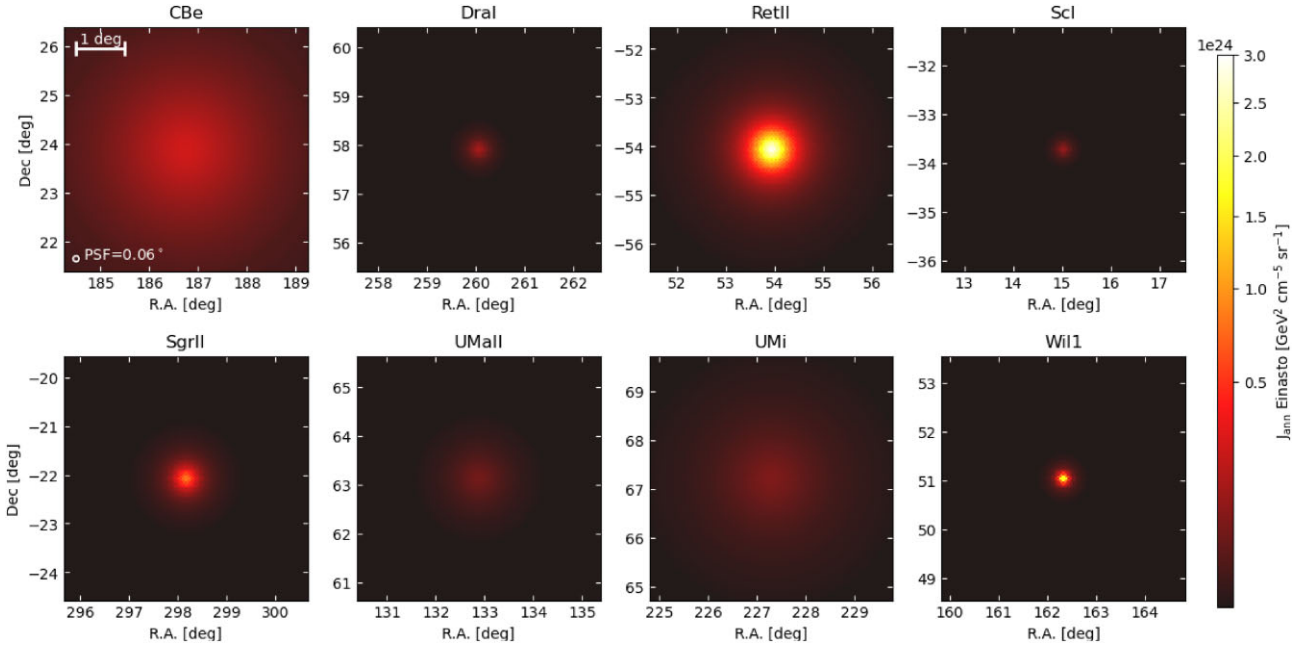

Figure 7. 2D distributions of the astrophysical factors of the selected dSphs obtained with CLUMPY for an Einasto profile. The CTAO PSF (white circle) is indicated in the first panel.

the astrophysical factors computed with CLUMPY. The background model is estimated in energy and radial bins assuming the appropriate CTAO IRFs. We compute the excess counts over 10^4 realization of the signal and background models. In all cases, we find that the event excess is not significant over the background; therefore, we compute ULs at 95 per cent CL on $\langle \sigma v \rangle$ or 95 per cent CL lower limits (LLs) on τ using the profiles of the likelihood ratio equation (9) and the Wilks theorem for the definition of coverage. All pipelines can be found in the Online Material CTAO Consortium (2025). In the remainder of the section, we go into more details on the specificity on the analysis, while the results are reported in the next section.

3.1 Signal spectra and morphology

In order to compute the sensitivity we need to input a spectral and spatial model for the signal. We therefore integrate the DM density profiles of Fig. 3 over increasing radial/angular distances up to the tidal radius defined by equation (A3). The integration is done with CLUMPY utilities, but it can also be done independently. In Fig. 4, we report the annihilating DM profiles, and in Fig. 5, the decaying DM profiles.[14] In each figure, we report the median value and the 68 per cent containment region. We also report a benchmark value for the angular resolution of CTAO for graphical comparison.

From Figs 4, 5, and 7, one can see that some dSphs, especially the classical, and namely dSphs DraI, Scl, UMi, and partly Wil1 have a better defined astrophysical factor, whereas CBe, RetII, SgrII, and UMaII show larger uncertainties that also depend on the integration angle. When comparing with the CTAO angular resolution, there is in addition a wide spread in the halo extension, with none of the sources appearing as point-like. In Table 4, we investigate the fraction of signal encompassed at different integration angle. The fact that

Table 4. Signal fraction enclosed within a determined integration angle for annihilating and decaying DM profiles computed with the Einasto model. The ratio between the astrophysical factor at a given angle and that at the 'saturation' level computed at the tidal radius (see equation A3) is reported.

	Annihilating DM			Decaying DM		
Name	$< 0.1°$ (per cent)	$< 0.5°$ (per cent)	$< 1.0°$ (per cent)	$< 0.1°$ (per cent)	$< 0.5°$ (per cent)	$< 1.0°$ (per cent)
CBe	0.5	8.2	19.4	0.2	4.3	10.2
DraI	3.5	34.5	70.3	2.3	22.6	46.0
RetII	1.0	14.2	33.6	1.8	27.3	64.5
Scl	16.0	33.5	44.7	2.3	68.9	91.8
SgrII	2.4	20.6	35.7	3.0	26.5	46.0
UMaII	0.9	11.2	24.8	1.4	17.6	39.3
UMi	0.4	8.7	28.2	0.1	2.9	9.5
Wil1	1.2	5.1	7.0	14.5	60.1	82.8

the targets are extended has implications on the sensitivity: larger regions of interest (RoIs), where the signal is searched, imply larger contribution from the irreducible background. Given the fact that the signal intensity is not flat but decreasing toward larger distance from the centre (see Figs 4 and 5), it is likely that the outer rims of the targets will not contribute to the signal as much as the inner parts. In ON/OFF searches, where the background is estimated from a control region,[15] the exact determination of the RoI is relevant (see e.g. MAGIC Collaboration 2020). However, our analysis is based on the so-called *template background* method, in which we model the background acceptance over the entire FoV.

The morphological and physical similarities among different dSph haloes are at the basis of modelling their properties; e.g. L. E. Strigari et al. (2008) already found that typical dSphs appear to be hosted at the core of DM haloes of approximately the same mass and intrinsic

[14]The tables of the astrophysical factor profiles integrated over larger apertures, together with their uncertainties, can be found in the Online Material (CTAO Consortium 2025).

[15]We define as 'ON/OFF' observations both the case where the telescope points at the true source position, and when the control region is in a slightly offset position (false-source or *Wobble* method; V. P. Fomin et al. 1994).

properties, thus leading to similar expected γ-ray luminosities and hence to the determination of distance-dependent scaling relations, discussed in Section 2. Our conclusion is thus that the DM haloes around dSphs are concentrated enough such that the two profiles are similar. For this reason, we will concentrate only in Einasto profiles in the remainder of this work. We remark again that while this is sound for those targets with less uncertain astrophysical factor, we assume this to be true also for the entire sample. A future detailed study of the differences between the cuspy and cored DM density profiles will greatly benefit from improved spectrophotometric data sets, that will be collected by next-generation surveys and facilities before the start of the actual CTAO observations (see a dedicated discussion in Section 5.1).

In Fig. 7, we report the 2D skymaps for the selected dSphs for the annihilating DM case and a Einasto profile. These are also computed with CLUMPY, but can be generated independently. They are the 2D representation of Fig. 4 and are one of the morphological inputs for the subsequent analysis.[16] In the plots, the angular resolution is also shown. One can clearly see again how some dSphs are more extended than others. FITS files for these skymaps can also be found in the Online Material, together with those generated for the decaying DM scenario.

3.2 Computation of the background

The principal source of background is due to misclassified events coming from primary cosmic rays, especially protons, electrons and helium nuclei. To some extent they contribute to an irreducible background, depending on the primary energy and direction. The template prepares a background model sampled in spatial and energy bins, and randomized according to a Poissonian distribution when generating an actual background instance accounting for integration time, energy, angular offset, and bin-by-bin acceptance estimated via MC simulations.

In the template method, for the $i-$th energy bin and $j-$th angular bin, the modelled counts can therefore be written as:

$$n_{ij}(\alpha_s, \alpha_b) = \alpha_s\, n^s_{ij} + \sum_b \alpha_b\, n^b_{ij} \tag{7}$$

where α_s are the set of parameters influencing the signal count (those in equation 2 and those from the IRFs) and α_b are the set of parameters influencing the background counts. Once a background instance is generated, we proceed to model the signal for annihilating DM by considering $\langle\sigma v\rangle$ as the parameter of interest and treating all others as nuisance. Analogue consideration can be made for decaying DM replacing τ as parameter of interest.

In case of only Poissonian fluctuations on n_{ij}, the combined likelihood of having n_{ij} counts in all energy and spatial bins assuming our model with $\langle\sigma v\rangle$ as parameter of interest and nuisance parameters ν can be written as:

$$\mathcal{L}(\langle\sigma v\rangle; \boldsymbol{\nu}|\boldsymbol{D}) = \prod_{i=1}^{N_E}\prod_{j=1}^{N_P} \frac{\mu_{ij}^{n_{ij}}\, e^{-\mu_{ij}}}{n_{ij}!}\,, \tag{8}$$

where $\mu_{ij} = \alpha_s\, \mu^{(s)}_{ij} + \sum_b \alpha_b\, \mu^{(b)}_{ij}$ is the Poissonian mean of the expected signal (s) and background (b) counts for each energy and spatial bin, and $\boldsymbol{D}$ is the simulated data set.

[16] In order to cast the CLUMPY skymaps into GAMMAPY-readable 2D maps in FITS format, one can use the script `makeFitsImage.py` available in the Online Material (CTAO Consortium 2025).

According to the Neyman–Pearson lemma (J. Neyman et al. 1933), the test statistics that rejects false hypotheses with higher power is the (inverse of the) likelihood ratio between the absolute maximum-likelihood estimation (MLE) of the parameters of interest and nuisance combined $\hat{\boldsymbol{\alpha}}$; $\hat{\nu}$ and the MLE of the parameter of interest setting the nuisance parameters as those obtained before. The ratio of the ln likelihoods can be thus written as:

$$-\,2\ln\lambda(\langle\sigma v\rangle|\boldsymbol{D}) = \frac{\mathcal{L}(\langle\sigma v\rangle; \hat{\hat{\nu}}|\boldsymbol{D})}{\mathcal{L}(\widehat{\langle\sigma v\rangle}; \hat{\nu}|\boldsymbol{D})} \tag{9}$$

Equation (9) is distributed as a χ^2 probability distribution with one degree of freedom corresponding to our parameter of interest, according to the S. S. Wilks (1938) theorem. If the target is not detected, we produce one-sided upper limits (ULs) at 95 per cent CL by solving the equation $-2\ln\lambda(\langle\sigma v\rangle) = 4$, with $\langle\sigma v\rangle$, τ restricted to the physical region (i.e. positive).

3.3 Uncertainties on the astrophysical factor

The most relevant contribution to systematic uncertainties stems from the computation of the astrophysical factor. As shown in Figs 4 and 5, the uncertainties in the profiles can be larger than 1 dex especially in the case of ultrafaint dSphs; furthermore, the uncertainty depends on the integration angle, generally increasing with the aperture (an example of posterior distribution for different integration angles is shown in Fig. A3). This means that, in principle, one should compute a different posterior distribution for each spatial bin of equation (8), which may significantly complicate the computation. To overcome this issue, we modify the likelihood equation (9) following the approach of (CTAO Consortium 2024a), i.e. including in equation (8) the distributions of astrophysical factor realizations $\mathcal{G}(\tilde{J}, \sigma_J)$ parametrized as a lognormal (see Appendix B1):

$$\mathcal{L}(\boldsymbol{\alpha}; \boldsymbol{\nu}|\boldsymbol{D}, J) = \mathcal{L}(\boldsymbol{\alpha}; |n_{ij}(\boldsymbol{\nu}), J) = \prod_{i=1}^{N_E}\prod_{j=1}^{N_P} \frac{\mu_{ij}^{n_{ij}}\, e^{-\mu_{ij}}}{n_{ij}!} \cdot \ln\mathcal{G}(\tilde{J}, \sigma_J) \tag{10}$$

We then re-run our simulations, using equation (10) with 10^4 trials for each target. Throughout this work, we compare the results obtained with and without the extra term for the astrophysical factor uncertainties in equation (10), since this plays a fundamental role in both the characterization of the DM exclusion limits and the choice of optimal targets.

3.4 Other systematic uncertainties

The discussion of additional systematics is deferred to Appendix B. Here, we provide a brief summary. Overall, all other systematics are largely subdominant with respect to the uncertainty in the astrophysical factor:

(i) As discussed, we used a template-background approach. An alternative method, based on the so-called ON/OFF analysis, in which the background is estimated from a background control (OFF) region and applied to the signal region (ON) may produce different constraints. The change is around 10 per cent at 300 GeV and less then 2 per cent above 300 GeV, see upper left Fig. B2.

(ii) The use of GAMMAPY rather than alternative reconstruction tools, such as the public software CTOOLS (J. Knödlseder et al. 2016) or the Asimov dataset-based sensitivity code SWORDFISH (T. D. P. Edwards & C. Weniger 2017; T. D. P. Edwards & C. Weniger 2018)

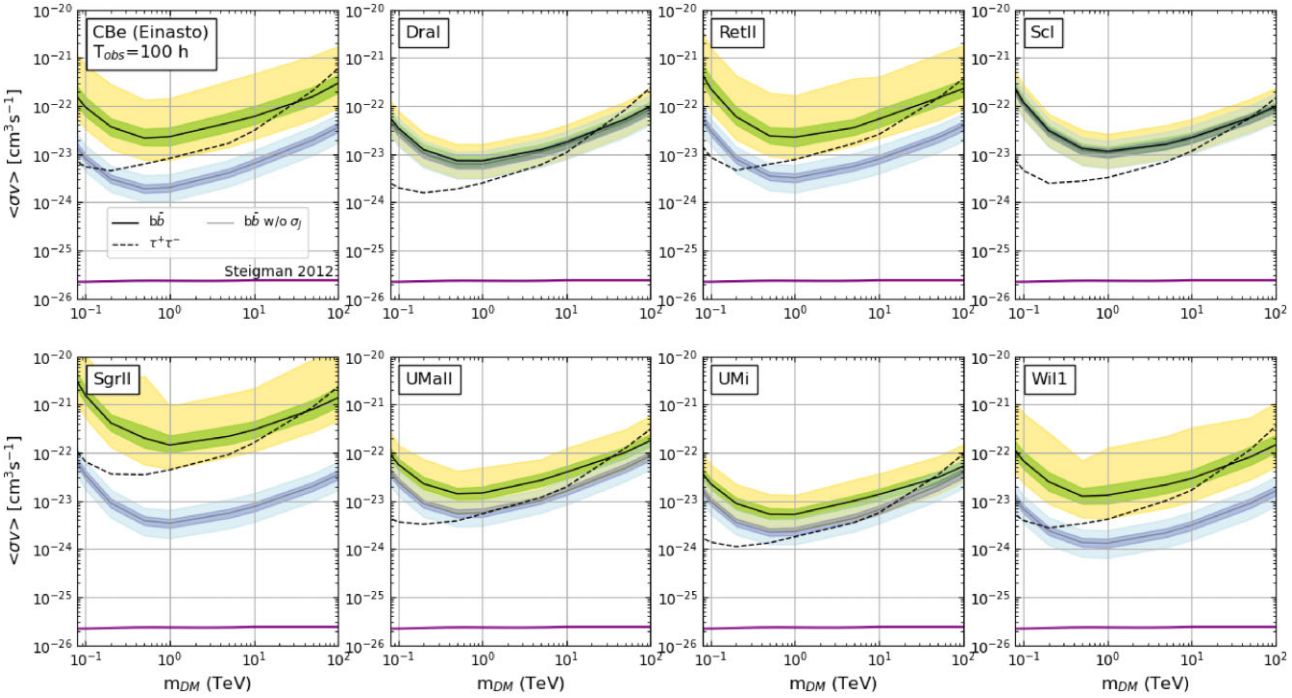

Figure 8. ULs on $\langle \sigma v \rangle$ for annihilating DM for the eight optimal targets, with astrophysical factors computed from the Einasto DM density profile. The median limits (black solid and dashed lines), along the corresponding 1σ (green shaded areas) and 2σ (yellow shaded areas) statistical uncertainties, are computed assuming 100-h observations of each source and DM annihilating into either the $b\bar{b}$ (black solid lines) or the $\tau^+\tau^-$ (black dashed lines) channel and including the uncertainties on $J_{\rm ann}$ as in equation (10). The same limits obtained by excluding that uncertainty (solid grey lines and blue/light-blue shaded areas) are also shown. In all panels, the thermal relic value from G. Steigman et al. (2012, purple solid line) is indicated.

provide differences of less than 10 per cent throughout the DM mass range.

(iii) The uncertainties on the IRFs, obtained by bracketing the IRFs, introduce a difference of less than 2 per cent; See Appendix B for more information.

(iv) In our analysis, we neglected the contribution of other sources of γ-rays, such as those coming from the diffuse γ-ray background. The amount of such contribution depends on the Galactic latitude and is increasing toward the GC plane. At the latitude of the dSphs into consideration, this contribution is negligible.

Similar systematic uncertainties are found in other DM-oriented CTAO searches (CTAO Consortium 2019, 2024b, a).

4 RESULTS

In the case of no detection for any combination of the DM channels and celestial targets presented above, we can compute the CTAO expected limits at 95 per cent CL to the DM parameters using the procedure described in Section 3. To this end, we consider $\langle \sigma v \rangle$ and τ as free parameters in equation (9) and maximize the likelihood of equation (10) that includes the uncertainties on the astrophysical factor. We organize the results as follows: in Section 4.1, we present the ULs for DM annihilation considering cuspy DM density profiles for the optimal targets defined in our study (see Fig. 8); in Section 4.2, we show the LLs on the particle lifetime for models of decaying DM (see Fig. 9); in Section 4.3, we discuss the CTAO sensitivity for the case of a combined likelihood analysis of multiple sources (see Fig. 10). In all of these subsections, we consider the cases of DM annihilation and decay into the $b\bar{b}$ and $\tau^+\tau^-$ channels, taken as representative examples of a soft and a hard DM γ-ray spectrum, respectively (see Section 2.1). Furthermore, we show how the cross-section limits change when considering other annihilation channels such as W^+W^- and $\mu^+\mu^-$ (see Fig. 11). These results are put into context and discussed in Section 5. We provide numerical values for all limits in the Online Material (CTAO Consortium 2025).

4.1 Upper limits to the cross-section for DM annihilation

In Fig. 8, we report the ULs on the velocity-averaged annihilation cross section for the eight optimal dSphs, assuming 100-h observations with the respective CTAO array (either CTAO-N for Northern sources, or CTAO-S for Southern targets) and annihilation in the $b\bar{b}$ or the $\tau^+\tau^-$ channels. For the $b\bar{b}$ channel, we also report the 1σ and 2σ statistical uncertainties along with the comparison of the limits with those that would have been obtained by neglecting the astrophysical factor uncertainty – i.e. using equation (8) in place of equation (10). DraI and UMi provide the strongest constraints considering such an uncertainty, replaced by Wil1 and CBe if we only consider the median value of $J_{\rm ann}$. The reason for the more constraining nature of the leptonic limits with respect to the hadronic ones is due to the different spectral shape in this mass range (see Fig. 1).

4.1.1 Impact of the uncertainties on the astrophysical factors

Fig. 8 clearly displays the impact of the astrophysical factor uncertainty on the DM limits. The green/yellow shaded area refers to limits obtained accounting for such uncertainties, and the blue/light blue shaded area to those obtained considering the $J_{\rm ann}$ median values only. This choice has no or negligible impact for the classical dSphs DraI and Scl thanks to both the good knowledge of their stellar velocities and the availability of more member stars with respect to

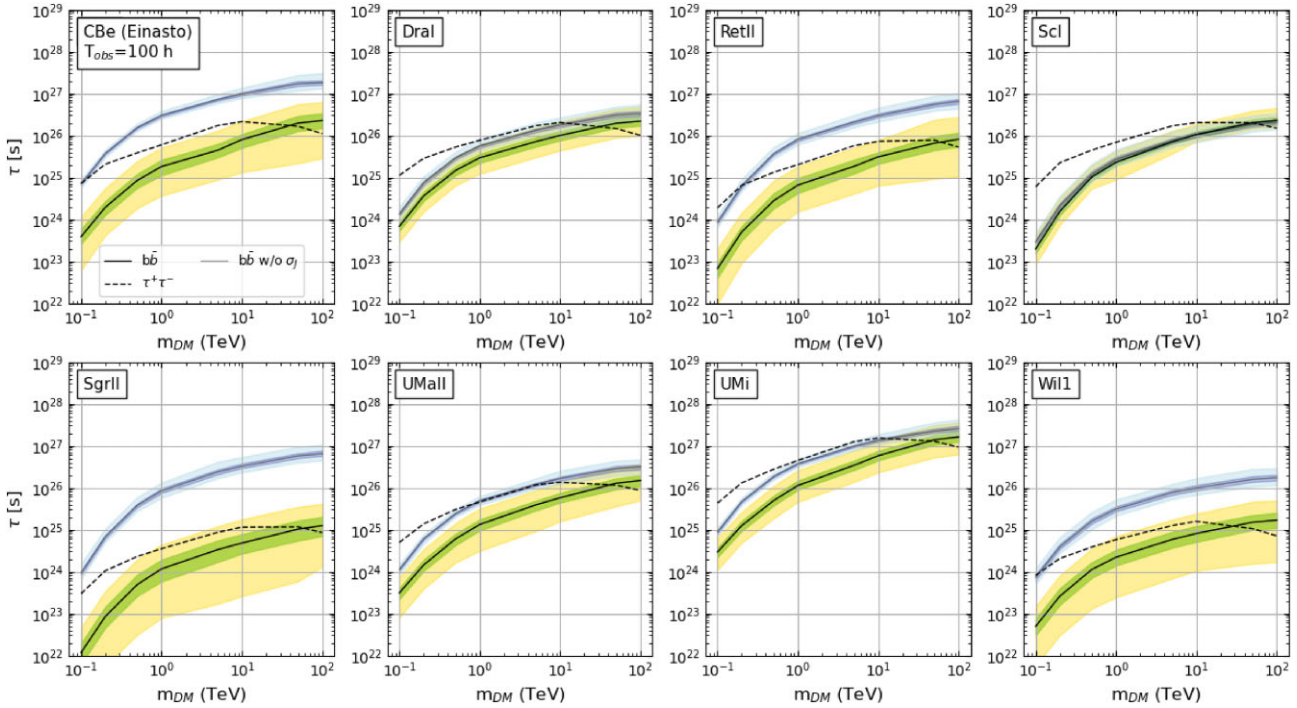

Figure 9. LLs on the particle lifetime for DM (Einasto DM density profile) decaying into the $b\bar{b}$ (solid lines) and $\tau^+\tau^-$ channels (dashed lines). In all plots, the statistical uncertainty bands at 1σ (green shaded areas) and 2σ (yellow shaded areas) obtained including the uncertainties on $J_{\rm dec}$ as in equation (10) are reported on the $b\bar{b}$ limits. The same limits obtained by excluding that uncertainty (blue/light-blue shaded areas and solid grey line) are also shown.

the ultrafaint dSphs. These latter targets exhibit a worsening of the limits by a factor of $\gtrsim$10: this finding has strong implications in terms of both sensitivity reach and especially target selection (see Section 5.5), demonstrating the need to collect high-quality data on dSphs for this kind of studies.

4.1.2 Impact of cuspy and cored DM density profiles

We have shown in Fig. 3 how cored DM density profiles are very similar to the cuspy ones, thus providing astrophysical factors that are comparable to each other within 1σ uncertainties when integrated along the l.o.s. We refer to Table A5 for a depiction of this fact; the limits to the DM parameters obtained for cored DM distribution would therefore be compatible with those shown in Fig. 8, as already found by M. Ackermann et al. (2015) with cored profiles implying changes in the predicted limits by a factor of at most ∼40 per cent. For this reason, we do not report them independently in this paper, always referring to the astrophysical factors obtained for the case of a cuspy DM profile in the following. However, in case of significant detection, N. Hiroshima, M. Hayashida & K. Kohri (2019) demonstrated that CTAO has the capabilities to discriminate between cuspy and cored profiles in dSphs.

4.2 Lower limits on the DM lifetime

The case of decaying DM requires a similar analysis, however: (i) the signal model having the particle DM lifetime τ as free parameter (equation 2); (ii) the spectral photon yield only extending up to $m_{\rm DM}/2$ due to the energy budget of the process; and (iii) the astrophysical factor being the integral of the linear DM density rather than its square (see equation 3) over the l.o.s. and the solid angle, shown in Fig. 5 as a function of the integration angle $\alpha_{\rm int}$. The LLs on the DM particle lifetime, reaching values above 10^{27} s for the prototypical $b\bar{b}$ and $\tau^+\tau^-$ channels, are shown in Fig. 9, with DraI and UMi again providing the strongest constraints taking into account their astrophysical factors uncertainties in place of CBe and UMi when neglecting them.

4.3 Combined results for multiple targets

Although the observational strategy of CTAO on dSphs is not ultimately defined, it was discussed e.g. in CTAO Consortium (2019) that an observing time of ∼100 h will be allocated on one or more dSphs. Considering that the amount of observing time allocated for the CTAO key science programs (KSPs) – with the indirect searches of γ-ray signals from DM annihilation or decay in dSph haloes being one of them – will considerably decrease with time in favour of guest programs, it is reasonable to propose that CTAO invests a total of 500 − 600 h shared between both sites for the observation of dSphs. To discuss the distribution of such a significant amount of time among the optimal dSphs, we present three scenarios: (1) a combination of the observations of all the eight optimal dSphs, observed for 75 h each, taking into account the respective astrophysical factor uncertainties; (2) a combination of 600-h observations of the two overall best targets (300 h/target) taking into account their astrophysical factor uncertainties; and (3) a combination of 600-h observations of the two overall best targets (300 h/target) neglecting their astrophysical factor uncertainties (see below).

4.3.1 Combined results for the annihilating DM scenario

For case (1), we combine the sources by profiling the expected uncertainties on the values of $J_{\rm ann}$ over their lognormal posterior distributions (see equation 10). For case (2), we instead consider the

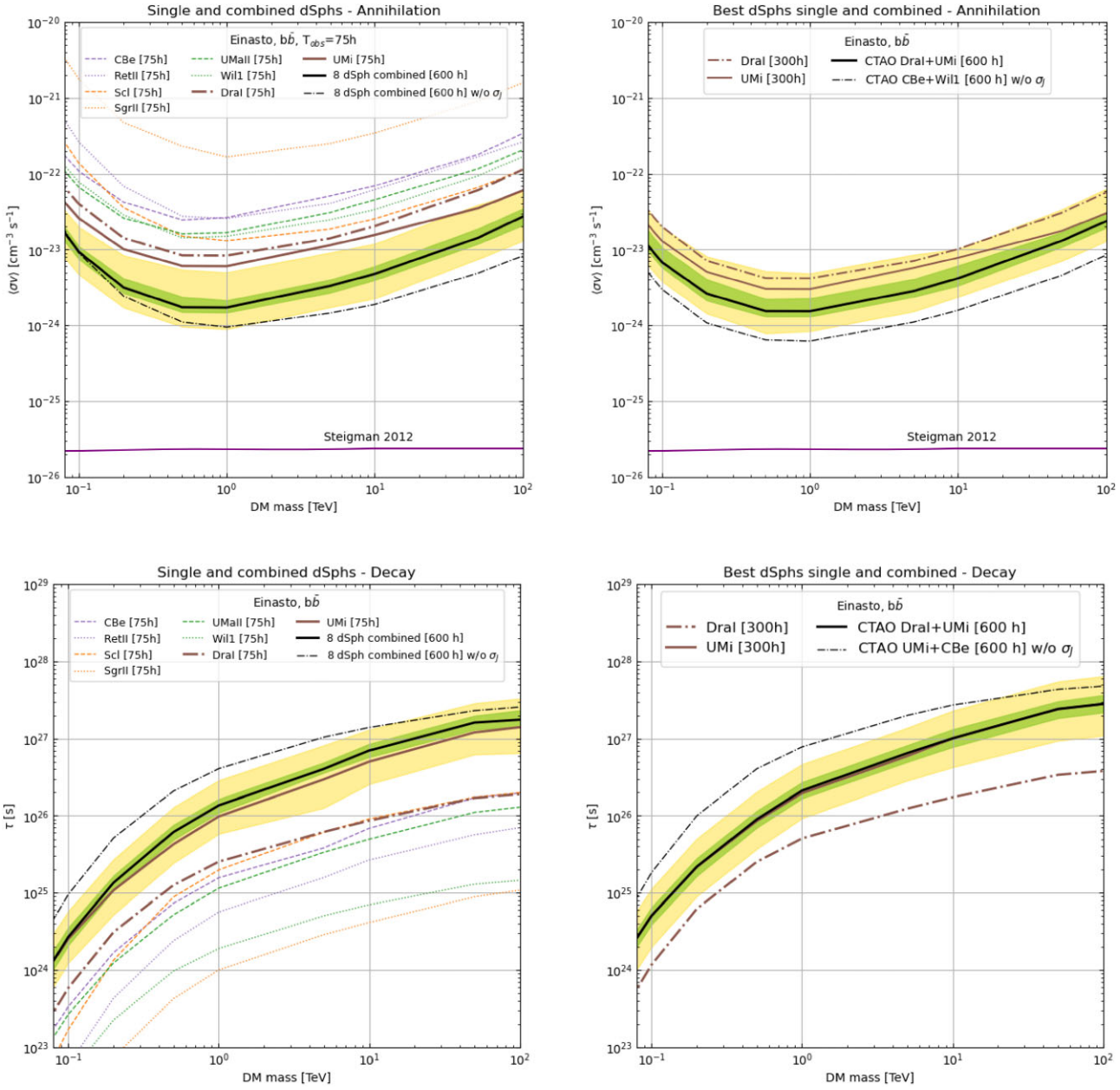

Figure 10. Constraints on the DM annihilation cross section and decay lifetime from combined likelihood analyses, both including and excluding uncertainties in the dSph astrophysical factors. Left panels: combination of the limits from all of the optimal dSphs observed for 75 h each. Right panels: combination of the limits of the two best dSphs observed for 300 h each. In all panels, the uncertainties on the combined cross-section limit due to photon statistics at 1σ (green shaded area) and 2σ CL (yellow shaded area) are reported along with the thermal-relic limit (purple solid line; G. Steigman et al. 2012).

two targets providing the largest expected signal, i.e. DraI and UMi. Finally, Wil1 and CBe are considered for case (3). We report the results in Fig. 10.

Comparing strategies (1) and (2), we find that both allow to reach similar limits, with the combination of two deep observation marginally more sensitive. This is related to the fact that, while the targets with the largest astrophysical factors dominate the limits, the inclusion of the uncertainties in the likelihood maximization process plays a significant role. We remark that, neglecting the astrophysical factor uncertainties, the combined limits of all the optimal dSphs would be somewhat more constraining, and that the best targets would be CBe and Wil1, whose combined limits would be significantly more constraining (dot–dashed lines in the upper right panel of Fig. 10).

Furthermore, we compute the cross-section ULs for the bosonic W^+W^- channel and the leptonic $\mu^+\mu^-$ channel in addition to those for the $b\bar{b}$ and $\tau^+\tau^-$ channels. In Fig. 11, we compare these limits together by analysing the combination of 300-h observation of Wil1 and CBe. This figure shows that the $b\bar{b}$ and $\tau^+\tau^-$ channels are indeed representative of several cases: in fact, the $b\bar{b}$ spectrum is similar to other hadronic or bosonic channels such as W^+W^-. The $\tau^+\tau^-$ hard channel represents the more constraining case, with a lighter leptonic channel such as the $\mu^+\mu^-$ providing weaker constraints but similar in shape. The $\tau^+\tau^-$ channel is the most constraining for both the

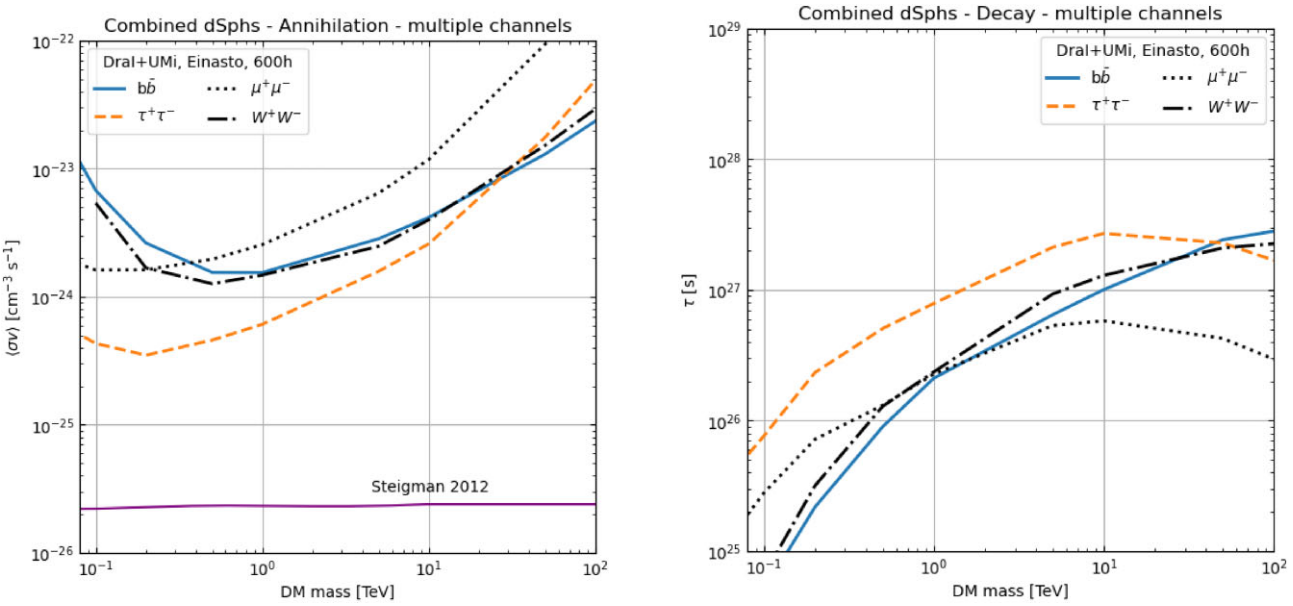

Figure 11. Constraints on the DM annihilation cross-section and decay lifetime for other choices of the SM interaction channel. Left panel: ULs on DM annihilation with 600 h of combined observations of Wil1 and CBe (Einasto DM density profile); the thermal-relic cross-section by G. Steigman et al. (2012, purple solid line) is indicated as reference. Right panel: LLs on the particle lifetime for DM decay with 600 h of combined observations of CBe and UMi (Einasto DM density profile).

annihilation and decay cases, except at very large masses (above ∼40 TeV) where the $b\bar{b}$ channel start to be dominant.

4.3.2 *Combined results for the decaying DM scenario*

We also report LLs on the particle lifetime for DM decay channels that produce the $\mathrm{d}N_\gamma/\mathrm{d}E_\gamma$ photon yield term of the expected DM flux in equation (2), obtained by repeating, for the case of decaying DM, the analysis presented above. Also in this case, the two best targets are DraI and UMi if we take into account the uncertainty on $J_{\rm dec}$ or CBe and UMi if we neglect it. We reach conclusions that are similar to those that hold annihilating case, with the difference that the limits are dominated by UMi alone. We show these results in Fig. 10, also comparing them in Fig. 11 for different decay channels.

5 DISCUSSION

We now discuss the results obtained in Section 4, and place them in the wider context. We discuss the prospects for discovery of new dSphs or for refinement of their astrophysical factors in the next decade (see Section 5.1). We compare our results compared to present and future γ-ray experiments and observatories in Section 5.3, and subsequently describe possible optimizations of the observational strategy in Section 5.5.

5.1 Expected observations of dSphs in the next decade

Over several decades of efforts, it is plausible that only a fraction of all dSphs residing in the MW halo has been discovered so far. Estimating a maximal number of them requires a certain set of assumptions, based on both N-body simulations and theoretical arguments. If we follow O. Newton et al. (2018), we expect for an MW-like galaxy 124^{+40}_{-27} (68 per cent confidence) satellite galaxies brighter than $M_V = 0$ within 300 kpc of the Sun. The prediction is based on the *Aquarius* simulation, from the number of satellites detected by the Sloan Digital Sky Survey (SDSS) and the Dark Energy Survey (DES; E. Sánchez & DES Collaboration 2016). Of the expected 124, 46^{+12}_{-8} are ultrafaint dSphs ($-8 \leq M_V \leq -3$) and 61^{+37}_{-23} are hyperfaint ($M_V \geq -3$). Roughly half the predicted number of ultrafaint dSphs has actually been discovered, and the observation of hyperfaint targets requires a survey ∼4 mag deeper than DES.

In order to improve the modelling of the DM distribution, one needs accurate spectroscopic information to infer the velocity distribution, and ultimately the actual gravitational potential through the Jeans formalism. Also, if the number of identified stars is few tens, any prediction on the dSph astrophysical factor less uncertain than a factor of $10 - 100$ is hard to obtain (see the cases of Seg1 and TriII as examples; see also fig. 3 of A. Chiappo et al. 2019). To date, several observational projects have surveyed in great detail some fraction of the sky in search of dSphs, with a comparable number currently underway or planned:

(i) DES (E. Sánchez & DES Collaboration 2016), that ended in 2019, was an international effort dedicated to map $\mathcal{O}(10^{11})$ galaxies, in order to unveil the nature of the so-called dark energy[17] (R. Caldwell & M. Kamionkowski 2009; L. Amendola & S. Tsujikawa 2010; M. Li et al. 2011; M. Kunz 2012);

(ii) *Gaia* (W. O'Mullane et al. 2000), launched in 2013 and ended in 2025, is a satellite mission aimed at charting a 3D map of the MW, with accurate positional and radial velocity measurements needed to produce a stereoscopic and kinematic census of $\mathcal{O}(10^9)$ stars in our Galaxy and throughout the LG;[18]

(iii) the SDSS (D. G. York et al. 2000) is the first facility providing multi-epoch optical spectroscopy across a large fraction of the sky, as well as now offering contiguous integral-field spectroscopic coverage of the MW and Local Volume galaxies;[19] in past years, its observations allowed the discovery the first ultrafaint dSphs;

[17] See https://www.darkenergysurvey.org/.
[18] See https://sci.esa.int/web/gaia.
[19] See https://www.sdss.org.

(iv) the Hyper Suprime-Cam Subaru Strategic Program (HSC-SSP; H. Aihara et al. 2018) is a three-layered, multi-band (*grizy* plus 4 narrow-band filters) imaging survey with the HSC on the 8.2-m *Subaru* Telescope that took data until 2020[20];

(v) the Panoramic Survey Telescope and Rapid Response System 1 (Pan-STARRS1; H. A. Flewelling et al. 2020) is an optical and near-infrared survey that covered the entire sky north of declination -30°, including the Galactic plane, until 2014.[21]

(vi) the DESI survey (A. Dey et al. 2019) seeks to map the large-scale structure of the Universe over a wide range of look-back times with the Dark Energy Spectroscopic Instrument (B. Flaugher & C. Bebek 2014) mounted since 2019 on the 4-m Mayall Telescope at the Kitt Peak National Observatory, targeting $\sim 3 \times 10^7$ pre-selected galaxies across $\sim$1/3 of the night sky;[22]

(vii) the *Euclid* mission (Y. Mellier et al. 2025) detects main-sequence stars up to Galactocentric radii of $\sim$100 kpc, providing details for dSphs lying in the outer MW halo;[23]

(viii) the WEAVE Project (S. Jin et al. 2023) is a survey plan aimed at exploiting the capabilities of the WEAVE (WHT Enhanced Area Velocity Explorer) multi-object survey spectrograph for the 4.2-m William Herschel Telescope (WHT) at the Observatorio del Roque de los Muchachos (La Palma, Canary Islands), that allows astronomers to take optical spectra of up to $\sim$1000 targets over a 2° FoV in a single exposure with a resolving power of up to 20 000;[24]

(ix) the planned ESA 'Analysis of Resolved Remnants of Accreted galaxies as a Key Instrument for Halo Surveys' (ARRAKIHS) mission will image 50 sq deg of the sky per year down to an unprecedented ultra-low surface brightness simultaneously achieved in two visible bands, providing important insights on the populations of ultrafaint dSphs (ESA ARRAKIHS Consortium 2025).

To catalogue the entire population of dSphs, these surveys are accompanied by follow-ups of DES, in particular the Survey of the Magellanic Stellar History[25] (SMASH; D. L. Nidever & SMASH 2017) since 2012 and the Magellanic Satellites Survey (MagLiteS; A. A. Drlica-Wagner & MagLiteS Team 2017) since 2017 that are dedicated to surveying ample sky regions around the Magellanic Clouds. In addition, future instruments tailored for this specific task will become operational; such efforts include the recently inaugurated 'Vera C. Rubin' Observatory[26] (Ž. Ivezić et al. 2019), and 4MOST (4-metre Multi-Object Spectroscopic Telescope), a wide-field, high-multiplex, fibre-fed, optical spectroscopic survey facility to be mounted on ESO's 4-m-class telescope VISTA[27] (R. S. de Jong et al. 2019), for both of which the first light is expected in 2026.

Spectroscopic measurements are already within reach of facilities such as the Deep Imaging Multi-Object Spectrograph (DeIMOS;[28] S. M. Faber et al. 2003), the Michigan/Magellan Fiber System (M2FS;[29] M. Mateo et al. 2012), and GIRAFFE[30] (F. Royer et al. 2014), all currently operational since $\gtrsim$10 yr. In the future, the E-ELT[31] (R. Gilmozzi & J. Spyromilio 2007), currently under construction at the Cerro Armazones (Chile) site – close to CTAO-S – will also sample dSph member stars with unprecedented sensitivity.

A complementary approach to evaluate the future prospects consists in performing analytical or semi-analytical estimates of the number of MW satellites, with the aim of predicting the abundance of potentially highly DM-dominated dSphs to be discovered in the future. For example, S. Ando et al. (2019) compute the statistics of objects discovered by the Large Synoptic Survey Telescope (LSST) by adopting models of MW halo substructures and phenomenological prescriptions connecting subhaloes to satellite galaxies. In this way, they find that $\sim$1 target with $\log J_{\rm ann}(< 0.5^\circ) \geq 19.4$ is expected 5 per cent of the time, consistent with our computation of the astrophysical factor for CBe. More optimistically, J. Coronado-Blázquez et al. (2021) pointed out, based on predictions from the DM-only *Via Lactea II* simulations (see e.g. T. Kelley et al. 2019, for results from hydrodynamical simulations), that CTAO will likely detect $\gtrsim$5 to $\gtrsim$10 targets with $\log J_{\rm ann}(<0.5^\circ) \gtrsim 19$, and $\sim$1 with $\log J_{\rm ann}(<0.5^\circ) \gtrsim 20$, considering the cumulated exposure over the sky.

Such results further highlight that, with a wide range of spectrophotometric instruments already available and more performing facilities planned for the near future, dedicated observational campaigns for the discovery of dSphs and more detailed investigation of the stellar content of those presently known should become operational before the advent of CTA. The expected results from observations carried out with such facilities will impact for both the discovery of new nearby, low-luminosity dSphs that had remained undetected so far (e.g. A. Drlica-Wagner et al. 2020) and are possibly hosted inside massive DM haloes, and for the better determination of the kinematic properties of (ultra-faint) sources with sparsely populated stellar samples (see Table A2), for which an improvement in the determination of $J_{\rm ann}$ and $J_{\rm dec}$ is anticipated.[32]

5.2 'Champion' dSphs: the case of UMaIII

As discussed above, N-body simulations (e.g. J. Diemand et al. 2008) predict $\mathcal{O}(1)$ DM subhaloes with $J_{\rm ann} \gtrsim 10^{20}$ GeV^2 cm^{-5} in the MW halo (see J. Coronado-Blázquez et al. 2021). If such highly DM-dominated subhaloes have formed dSphs, they would constitute optimal targets for CTAO. In the following we argue that, if the observational data are confirmed, the recent discovery of the dSph U1/Ursa Major III (UMaIII hereafter; S. E. T. Smith et al. 2024) sparks interest, since this object could represent such a 'champion'. S. E. T. Smith et al. (2024) report that UMaIII would be the closest ultrafaint dSph ($d_\odot \sim 10$ kpc), and would possess a velocity dispersion of member stars yielding the highest value of $J_{\rm ann}$ over all known dSphs.[33]

The validity of this prediction is under debate: when in fact the star with the highest impact on the kinematic modelling of this system is removed from the analysis, the velocity spread reduces, completely vanishing when removing the second one L. K. C. Fisher et al. (2025, see also). However, by adopting the $J_{\rm ann}$-to-$d_\odot$ relation (equation 4),

[20] See https://hsc.mtk.nao.ac.jp/ssp/survey/.
[21] See https://panstarrs.stsci.edu/.
[22] See https://www.desi.lbl.gov/.
[23] See https://www.esa.int/Science_Exploration/Space_Science/Euclid.
[24] See http://www.ing.iac.es/weave/index.html.
[25] See https://datalab.noirlab.edu/smash/smash.php.
[26] See https://www.lsst.org/ and https://rubinobservatory.org/.
[27] See https://www.4most.eu/cms/home/.
[28] See https://www2.keck.hawaii.edu/inst/deimos/.
[29] See https://ui.adsabs.harvard.edu/abs/2012SPIE.8446E..4YM/abstract.
[30] See https://www.eso.org/sci/facilities/paranal/instruments/flames/inst/Giraffe.html.
[31] See https://elt.eso.org/.
[32] Preliminary tests show that the Jeans analysis on the dSph kinematics produces uncertainties that scale with $N^{-1/2}$ (i.e. according to a Poissonian statistics), where N is the number of confirmed member stars.
[33] The UMaIII astrophysical factor from M. Crnogorčević & T. Linden (2024) is $\sim$500 times higher than that of Scl, the first discovered dSph.

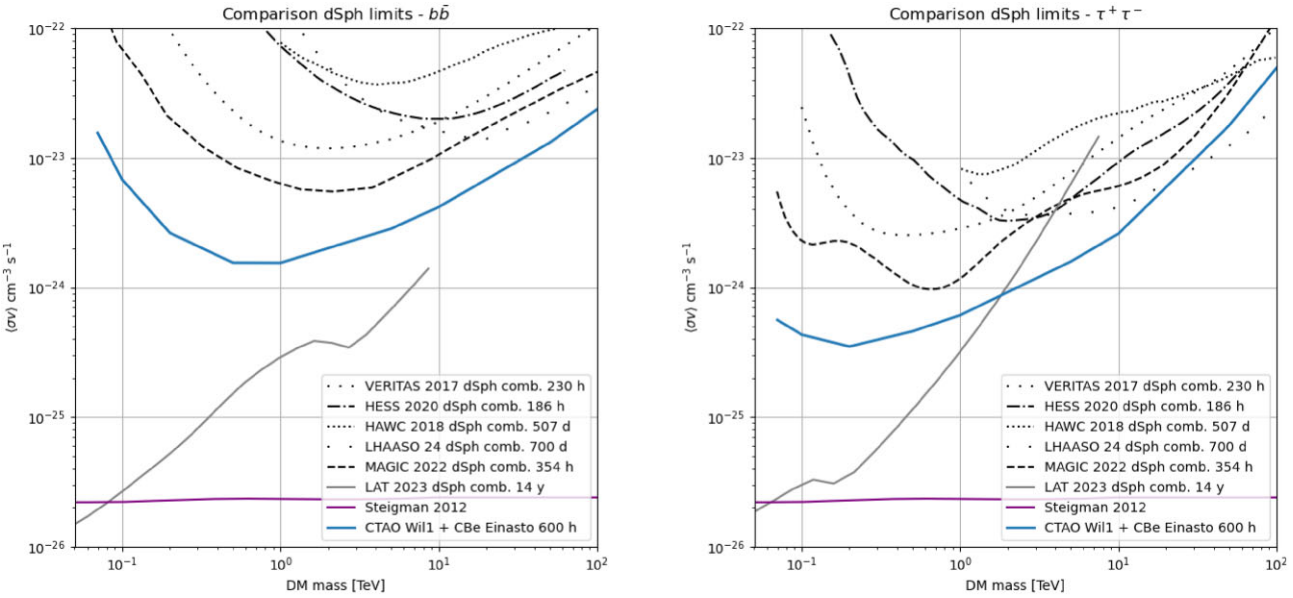

Figure 12. ULs to the DM annihilation cross-section with simulated CTAO observations of dSphs (blue solid lines) compared to the most constraining limits obtained with observations of dSphs by current γ-ray facilities – MAGIC (V. A. Acciari et al. 2022), HAWC (A. Albert et al. 2018), H.E.S.S. (H. Abdallah et al. 2020), *Fermi*-LAT (S. Hoof, A. Geringer-Sameth & R. Trotta 2020), and VERITAS (S. Archambault et al. 2017). The CTAO limits for dSphs are obtained with 600-h combined observations of Wil1 and CBe, assuming an Einasto DM profile. Left panel: limits for the $b\bar{b}$ channel. Right panel: limits for the $\tau^+\tau^-$ channel. In both panels, the value of the thermal-relic cross-section by G. Steigman et al. (2012) is indicated for reference.

M. Crnogorčević & T. Linden (2024) find $J_{\rm ann} \sim 10^{20.9}$ GeV^2 cm^{-5} for UMaIII, with an uncertainty of 0.1 dex only: this allows them to set an extremely robust constraint on the annihilation of DM with *Fermi*-LAT data (M. Crnogorčević & T. Linden 2024). We recall that this is not the first time that a cluster of stars is wrongly identified as the most DM-dominated target, having this already happened with Seg1 (J. D. Simon et al. 2011; V. Bonnivard et al. 2015b) and more recently with TriII (A. Genina & M. Fairbairn 2016; E. N. Kirby et al. 2017).

Given that 'champion' dSphs are predicted by N-body simulations and could possibly be correctly identified by the time in which CTAO will have started its operations, we investigate in the following the prospects of using targets like UMaIII in indirect DM searches. However, at present no robust spectrophotometric data are available from dedicated observing campaign of this source: therefore, we cannot include UMaIII in our analysis, since it would be excluded by the data quality selection. To overcome this issue, we thus limit ourselves to scale the expected limits for the dSphs analysed so far to the value of $J_{\rm ann}$ found by S. E. T. Smith et al. (2024) and M. Crnogorčević & T. Linden (2024).

5.3 Comparison with other limits – annihilating DM

We now first proceed to compare our limits with those obtained with dSph observations from other instruments. We show this comparison in Fig. 12 for the $b\bar{b}$ and the $\tau^+\tau^-$ channels; for conciseness, rather than providing an exhaustive census of all the limits available in the literature, we select only the more recent or more constraining results. To this aim, we use:

(i) data from the combination of 4 dSphs observed with MAGIC between 2011 and 2019 (V. A. Acciari et al. 2022); this data set is composed of 52.1 h on DraI, 49.5 h on CBe, 94.8 h on UMaII, and 157.9 h on Seg1, for a total of 354.3-h exposure time;[34]

(ii) H.E.S.S. data (H. Abdallah et al. 2020) including RetII (18.3 h), TucII (16.4 h), TucIII (39.0 h), TucIV (39.2 h), and GruII (29 h), for a total of ∼186 h;

(iii) VERITAS limits (S. Archambault et al. 2017) obtained from ∼230-h observations of 5 dSphs (Seg1, UMi, DraI, BooI, and Wil1);

(iv) HAWC results (A. Albert et al. 2018) based on the combined results from 15 dSphs (BooI, CVnI/II, CBe, DraI, Her, LeoI/II/IV, Seg1, Sex, UMaI/II, UMi, and TriII) in 507 d of data;

(v) *Fermi*-LAT results (A. McDaniel et al. 2024) obtained with 30 dSphs (the so-called Measured sample) observed for 14 yr.[35]

At the time of CTAO, interesting limits are also expected from annihilating DM in dSphs (J. A. R. Cembranos et al. 2020) from the Square Kilometer Array (R. Braun et al. 2015) and its precursors (A. Kar et al. 2019).

Looking at Fig. 12, we see that the CTAO limits obtained with the combination of the two best targets at hand – DraI and UMi – for a duration of observations of 600 h, would provide limits a factor of ∼10 better than any other current limits achieved by IACTs and shower front detectors. When comparing to *Fermi*-LAT (A. McDaniel et al. 2024), the CTAO limits would be the most constraining above ∼10 TeV for the $b\bar{b}$ channel and above ∼1 TeV for the $\tau^+\tau^-$ case. We advise some caution in making a direct comparison, due to the fact that our limits are obtained profiling over the astrophysical factor uncertainties while some of those with which we compare are not. As discussed in Section 4, neglecting such uncertainties can indeed have a major impact on the final results.

[34]For this data set, the astrophysical factors used for that work are compatible with those used here, except for Seg1.

[35]Wil1 is removed from this analysis due to the claim of strong evidence for tidal disruption and/or non-equilibrium kinematics (B. Willman et al. 2011).

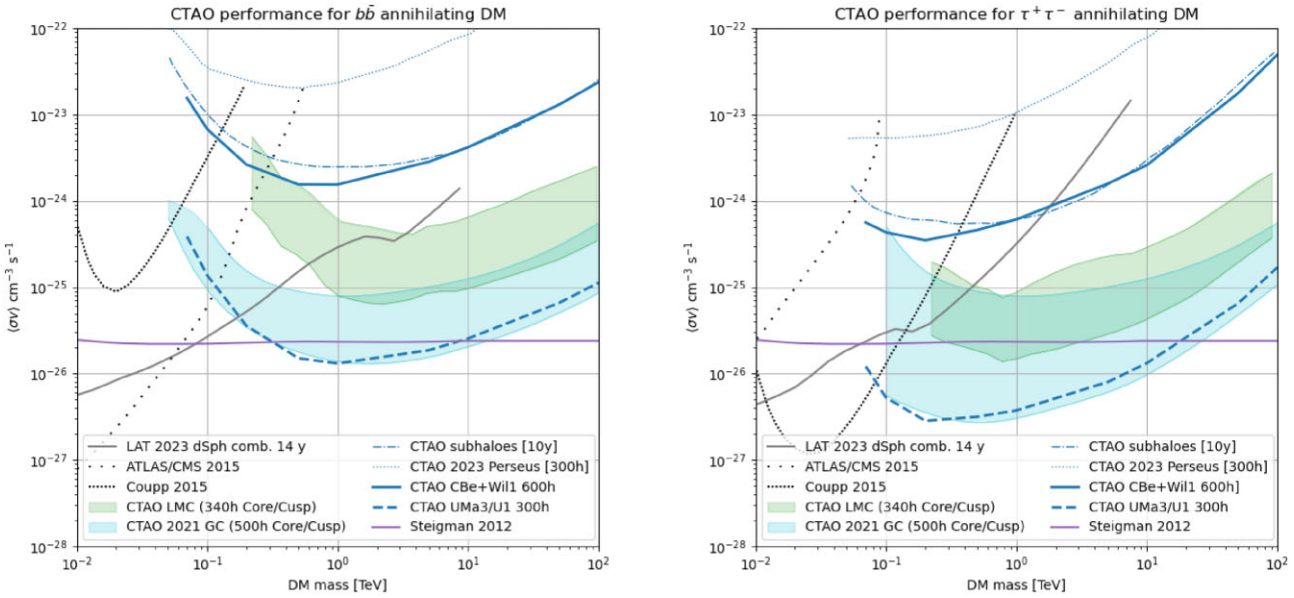

Figure 13. ULs to the DM annihilation cross-section with simulated CTAO observations of dSphs (blue solid lines) compared to the most constraining limits obtained by current γ-ray facilities (*Fermi*-LAT; S. Hoof et al. 2020) and to CTAO prospects on other targets – the LMC (CTAO Consortium 2023), the GC (CTAO Consortium 2021b), the DM subhaloes (J. Coronado-Blázquez et al. 2021), and the Perseus cluster (CTAO Consortium 2024b) – and from direct detection experiments and accelerators (D. Bauer et al. 2015). The CTAO limits for dSphs are obtained with 600-h combined observations of DraI and UMi, assuming an Einasto DM profile. Left panel: cross-section limits for the $b\bar{b}$ channel. Right panel: limits for the $\tau^+\tau^-$ channel. In both panels, the value of the thermal-relic cross-section by G. Steigman et al. (2012) is indicated. The projected limits for UMaIII/U1 discussed in the text are also shown.

In Fig. 13, we also compare the CTAO sensitivity in the $b\bar{b}$ and $\tau^+\tau^-$ channels using dSphs with other relevant indirect DM limits, either obtained for other classes of astrophysical targets that are suitable for DM searches with CTAO or derived with different techniques.[36] Specifically, we report limits obtained with ATLAS/CMS and COUPP by D. Bauer et al. (2015) adapted to the $\langle\sigma v\rangle - m_{\rm DM}$ plane,[37] the 14-yr *Fermi*-LAT limits from A. McDaniel et al. (2024, called MEASURED limit there), the limits predicted for CTAO observations of the GC (called SENS limit there, CTAO Consortium 2021b), those derived from observations of the Perseus galaxy cluster (called SENSMAX limit there CTAO Consortium 2024b) and the LMC (CTAO Consortium 2023, called NFWMEAN limit there); we also add predictions for CTAO in search of DM annihilation signals from dark clumps (called EXPO limit there, J. Coronado-Blázquez et al. 2021). Also here, some caution should be adopted when comparing other CTAO predictions with those obtained in this work, since all of them have been derived for fixed values of the astrophysical factors without profiling over the relative uncertainties.

Fig. 13 reveals that dSph observations with CTAO provide the most constraining limits in the multi-TeV WIMP mass range. The limits obtained with dSphs are significantly more constraining than those obtained for the Perseus cluster and dark clumps, demonstrating the relevance of using such a class of objects as targets for indirect DM searches. The dSph limits are instead less constraining than those predicted for both the GC and the LMC; however, we remark that such sources are subject to larger uncertainties on the DM modelling than dSphs, given the still poor modelling of the interplay between baryons and DM in the MW halo. Also, the assumption of a cored DM density profile in place of a cuspy one alters the predicted bounds up to a factor of $\sim 20\div50$ (CTAO Consortium 2021b). For the LMC observation, the DM signal is expected to be significantly extended ($\sim 10^\circ$) and contaminated by the astrophysical foreground emission (CTAO Consortium 2023). For these reasons, especially in the case of an established DM signal, dSphs would still be attractive targets to corroborate and further study this type of γ-ray emission.

5.4 Comparison with other limits – decaying DM

As done for the annihilation case, we show the comparison for the decaying DM case in Fig. 14, adopting the $b\bar{b}$ and the $\tau^+\tau^-$ as representative channels. We exclude UMaIII from these plots due to its compactness, which – similarly to Scl – would lead to a low integrated signal yield for DM decay. We compare our limits with a selection of recent and constraining results:

(i) M. Cirelli et al. (2012), who analysed the Fornax galaxy cluster as observed by H.E.S.S. and forecast limits for CTAO by adopting an educated guess of 50-h observations;

(ii) M. G. Baring et al. (2016), who analysed six years of *Fermi*-LAT data from 16 dSphs with a stacked analysis. This limits compare well with other *Fermi*-LAT based limits (e.g. S. Ando & K. Ishiwata 2015; C. Blanco & D. Hooper 2019) obtained from the analysis of the diffuse extragalactic γ-ray background emission;

(iii) CTAO prospects on the observation of the Perseus galaxy cluster for 300 h (CTAO Consortium 2024b);

(iv) Z. Cao et al. (2024), reporting limits obtained in 700 d of observations on a combination of dSphs.[38]

Fig. 14 shows that the CTAO limits for dSphs in the $\tau^+\tau^-$ channel are competitive above 10 TeV with respect to the current ones. Interestingly, the limits obtained in this work are orders of magnitude

[36]The search for narrow-line DM signatures with CTAO is reported in a separate work (CTAO Consortium 2024a).
[37]This choice is partially model-dependent.
[38]This combination includes Seg1.

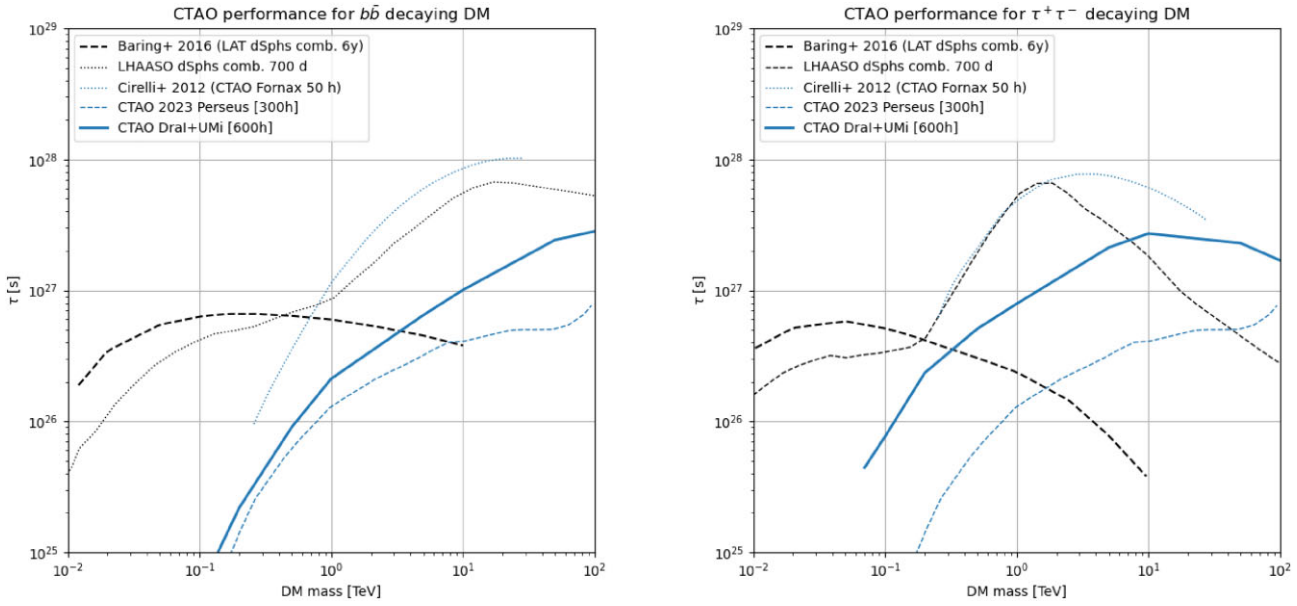

Figure 14. LLs on the DM decay lifetime for the $b\bar{b}$ channel with simulated CTAO observations of dSphs compared to the most constraining limits obtained by current γ-ray facilities – *Fermi*-LAT (M. G. Baring et al. 2016) and LHAASO (Z. Cao et al. 2024) – and the CTAO prospects for the Fornax (M. Cirelli et al. 2012) and the Perseus clusters (CTAO Consortium 2024b). The CTAO limits for dSphs are obtained with 600-h combined observations of CBe and UMi, assuming an Einasto DM profile. Left panel: cross-section limits for the $b\bar{b}$ channel. Right panel: limits for the $\tau^+\tau^-$ channel.

more constraining than those obtained when observing the Perseus galaxy cluster (CTAO Consortium 2024b): this is due to the larger distance of this source compared to our 'champion' dSphs (redshift $z \sim 0.02$; L. E. Bilton & K. A. Pimbblet 2018). A more suited galaxy cluster for decaying DM searches is Fornax ($z \sim 0.005$; P. Firth, M. J. Drinkwater & A. M. Karick 2008); however, the limits reported by M. Cirelli et al. (2012) are mostly based on the adopted educated guesses.

5.5 Observational strategy

The results obtained above allow us to discuss the observational strategy to be proposed for CTAO toward the class of dSphs. Considering the competition with other astrophysical targets and the preliminary scheme of the KSPs (CTAO Consortium 2019), we estimated in Section 4.3 that – although the formal schedule of observations is not fully defined yet and an ample amount of time will be devoted to guest programs, thus leading to a potential overestimation of the allocated observing time – CTAO could plausibly provide to ∼600 h on such sources. Having also shown how the constraints on the DM parameter space are strongly dominated by those objects with the highest astrophysical factors, we point to a strategy in which deep exposures of few 'champion' dSphs are performed. However, the choice of the best dSphs is strongly affected by uncertainties related to the astronomical knowledge of their stellar content and motion (see Appendix A). As discussed in Section 5.1, future astronomical campaigns on dSphs will be extremely relevant to obtain more accurate determinations of the DM density profile for both known dSphs and newly discovered candidates. An alternative strategy could be instead that of observing multiple dSphs to reduce the risk of uncertain astrophysical factors.

6 SUMMARY AND CONCLUSIONS

In this work, we have presented the prospects for the detectability of γ-rays from processes of DM annihilation and decay in dSph haloes with CTA, assuming DM to be composed of non-SM particles belonging to the WIMP class.

6.1 Summary of results

Our main results can be summarized as follows:

(i) We have consistently selected the best targets according to their DM content, starting from a complete list (see Table 2 and Table A1) and narrowing down to the optimal dSphs in terms of observability, expected signal strength and uncertainty on their astrophysical factors. Collecting all the most updated and complete samples of spectrophotometric data of such dSphs, we have made use of the public CLUMPY code to compute the DM distribution in the selected dSph haloes in a common framework of data treatment for both classical and ultrafaint targets (see Section 2.2 and Appendix A), and have compared our astrophysical factors with the results currently available in the literature (see Figs 6 and A2). Our calculations of $J_{\rm ann}$ and $J_{\rm dec}$ are in agreement with what has been found in both single-target and ensemble analyses of the DM content in dSph haloes, with the exception of those known targets that have biased observational data or exhibit tidal disruption features (see Section 2.2) We have also provided updated calculations of the corresponding astrophysical factors $J_{\rm ann}$ and $J_{\rm dec}$ (also known as J- and D-factors). This is of direct relevance for DM searches from dSphs also well outside the context of CTAO.

(ii) The uncertainties on the astrophysical factors due to the poor knowledge of stellar content and motion (extensively discussed in Appendix A) depend on the target, and may amount to more than an order of magnitude in the worst cases. This can in principle significantly bias our estimates, thus demanding deep surveys to

adequately sample the stellar content of this class of targets for both the already known ones and those newly discovered (see Section 5.1).

(iii) We have presented the signal model and analysis pipeline (see Section 3), based on the public GAMMAPY software – the official CTAO analysis code – and discussed the contribution of systematic uncertainties (see Appendix B). These amount to at most 10 per cent, and are subdominant with respect to the uncertainties on the astrophysical factor.

(iv) We have produced limits for annihilating DM both in individual targets (see Fig. 8) and from a combined analysis (see Section 4.3) down to $\langle \sigma v \rangle \sim 5 \times 10^{-25}$ cm^3 s^{-1}, as well as for the case of decaying DM up to $\tau \sim 10^{28}$ s (see Fig. 9), for combined observations of the best dSphs.

(v) The derivation of limits for annihilating or decaying DM with the inclusion of the astrophysical factor uncertainties plays an important role, since it may affect both the achieved sensitivity in the DM parameter space – a worsening of the derived limits by a factor $\gtrsim$10 (see Section 4.1) – and the optimal target selection. We recommend profiling the likelihood over the astrophysical factor uncertainties in all future works to improve the accuracy in assessing the effective reach of the indirect DM searches with the Cherenkov technique.

(vi) Limits at high DM masses obtained for dSphs with CTAO are up to one order of magnitude better than the corresponding limits obtained with current instruments (see Fig. 12). These limits are more constraining than those predicted for CTAO toward the Perseus galaxy cluster thanks to the dSph proximity and lack of significant background emission, but less than those derived from simulated observations of the GC or the LMC due to the intrinsically larger content of DM of such targets; however, the latter two are subject to large systematic uncertainties due to their DM modelling (see Fig. 13).

(vii) In case new DM-dominated dSphs will be discovered as predicted by numerical simulations (see Section 5.1), or the most optimistic astrophysical factors for objects like UMaIII will be confirmed, the CTAO reach with even a single target for annihilating DM will fall well below the thermal-relic limit in reasonable observing times (see Fig. 13).

6.2 Conclusions

In this work we argued that dSphs are a valid class of targets for indirect DM searches in VHE γ-rays, due to (i) the absence of a significant background contamination than in closer targets such as the GC and the LMC, thus providing independent constraints and corroborating evidence in case of signal hints at those targets, and (ii) stronger expected signals with respect to more distant sources such as the galaxy clusters. An optimal exploitation of dSphs for DM searches will, however, rely in future deep spectrophotometric surveys on current (or yet-to-be discovered) dSphs aimed at reducing the uncertainties in the DM modelling, in order to obtain the best set of dSphs to be pointed at in the CTAO era. In such conditions, the best observational strategy will be likely based on deep pointings of few optimal targets rather than shorter snapshots of many objects.

AUTHOR CONTRIBUTIONS

This publication is the result of a collaborative effort within the CTAO Consortium. The project was conceptualized and supervised by MD and FGS, who also defined the methodology and led the draft preparation. FGS carried out the formal analysis of the astrophysical factors using CLUMPY, while GRF performed the DM limits analysis using GAMMAPY and CTOOLS. AM contributed to the validation of the results and the preparation of the manuscript. K. D. Nakashima (FAU-Erlangen) contributed in earlier phases by computing the diffuse γ-ray background and cross-checking the analysis. The initial manuscript drafts were reviewed by A. Chen (Witwatersrand University), M.-Á. Sánchez-Conde (UAM-IFT), and T. Bringmann (Oslo University) on behalf of CTAO-SAPO. The rest of the authors in one way or the other contributed to the development of the CTAO analysis tools and IRFs and participated in the review of the manuscript through internal discussions and approval processes coordinated by the Dark Matter and Exotic Physics Working Group (DMEP-WG) leaders and the CTAO Speakers and Publications Office (CTAO-SAPO).

ACKNOWLEDGEMENTS

We thank the anonymous referee for their helpful comments. We also thank J. Palacio (MPIK), K. D. Nakashima (FAU-Erlangen), and G. D'Amico (UiB and INAF-OAPd) for earlier contributions and discussions about this project. FGS acknowledges financial support from the PRIN MIUR project 'ASTRI/CTA Data Challenge' (PI: P. Caraveo), contract 298/2017, and from the INAF Mini-Grant 2023 'MADaMA – Measuring the Amount of Dark Matter in Astrophysical targets'.

We gratefully acknowledge financial support from the following agencies and organizations: State Committee of Science of Armenia, Armenia; The Australian Research Council, Astronomy Australia Ltd, The University of Adelaide, Australian National University, Monash University, The University of New South Wales, The University of Sydney, Western Sydney University, Australia; Federal Ministry of Education, Science and Research, and Innsbruck University, Austria; Conselho Nacional de Desenvolvimento Científico e Tecnológico (CNPq), Fundação de Amparo à Pesquisa do Estado do Rio de Janeiro (FAPERJ), Fundação de Amparo à Pesquisa do Estado de São Paulo (FAPESP), Fundação de Apoio à Ciência, Tecnologia e Inovação do Paraná - Fundação Araucária, Ministry of Science, Technology, Innovations and Communications (MCTIC), Brasil; Ministry of Education and Science, National RI Roadmap Project DO1-153/28.08.2018, Bulgaria; The Natural Sciences and Engineering Research Council of Canada and the Canadian Space Agency, Canada; ANID PIA/APOYO AFB230003, ANID-Chile Basal grant FB 210003, Núcleo Milenio TITANs (NCN19-058), FONDECYT-Chile grants 1201582, 1210131, 1230345, and 1240904; Croatian Science Foundation, Rudjer Boskovic Institute, University of Osijek, University of Rijeka, University of Split, Faculty of Electrical Engineering, Mechanical Engineering and Naval Architecture, University of Zagreb, Faculty of Electrical Engineering and Computing, Croatia; Ministry of Education, Youth and Sports, MEYS LM2018105, LM2023047, EU/MEYS CZ.02.1.01/0.0/0.0/16_013/0001403, CZ.02.1.01/0.0/0.0/18_046/0016007, CZ.02.1.01/0.0/0.0/16_019/0000754 and CZ.02.01.01/00/22_008/0004632, Czech Republic; Academy of Finland (grant nos 317636 and 320045), Finland; Ministry of Higher Education and Research, CNRS-INSU and CNRS-IN2P3, CEA-Irfu, ANR, Regional Council Ile de France, Labex ENIGMASS, OCEVU, OSUG2020 and P2IO, France; The German Ministry for Education and Research (BMBF), the Max Planck Society, the German Research Foundation (DFG, with Collaborative Research Centres 876 and 1491), and the Helmholtz Association, Germany; Department of Atomic Energy, Department of Science and Technology, India; Istituto Nazionale di Astrofisica (INAF), Istituto Nazionale di Fisica Nucleare (INFN), MIUR, Istituto Nazionale di

Astrofisica (INAF-OABRERA) Grant Fondazione Cariplo/Regione Lombardia ID 2014-1980/RST_ERC, Italy; ICRR, University of Tokyo, JSPS, MEXT, Japan; Netherlands Research School for Astronomy (NOVA), Netherlands Organization for Scientific Research (NWO), Netherlands; University of Oslo, Norway; Ministry of Science and Higher Education, DIR/WK/2017/12, the National Centre for Research and Development and the National Science Centre, UMO-2016/22/M/ST9/00583, Poland; Slovenian Research and Innovation Agency, grants P1-0031, I0-E018, and J1-60014, Slovenia; South African Department of Science and Technology and National Research Foundation through the South African Gamma-Ray Astronomy Programme, South Africa; The Spanish groups acknowledge funds from 'ERDF A way of making Europe', the Spanish Ministry of Science, Innovation and Universities, and the Spanish Research State Agency (AEI) via MCIN/AEI/10.13039/501100011033, grants CNS2023-144504, PDC2023-145839-I00, PID2022-137810NB-C22, PID2022-139117NB-C41/C42/C43/C44, PID2022-136828NB-C41/C42, PID2022-138172NB-C41/C42/C43, PID2021-124581OB-I00, PID2021-125331NB-I00, and budget lines 28.06.000X.411.01 and 28.06.000X.711.04 of PGE 2023, 2024 and 2025; the 'Centro de Excelencia Severo Ochoa' program through grants nos CEX2019-000920-S, CEX2020-001007-S, and CEX2021-001131-S; the 'Unidad de Excelencia María de Maeztu' program through grants nos CEX2019-000918-M and CEX2020-001058-M; the 'Ramón y Cajal' program through grant RYC2021-032991-I; and the 'Juan de la Cierva' program through grants nos JDC2022-048916-I and JDC2022-049705-I. They also acknowledge the projects with refs. PR47/21 TAU and TEC-2024/TEC-182, both funded by the Comunidad de Madrid regional government. Funds were also granted by the 'Consejería de Universidad, Investigación e Innovación' of the regional government of Andalucía (refs. AST22_00001_9 and AST22_0001_16) and 'Plan Andaluz de Investigación, Desarrollo e Innovación' (ref. FQM-322); and by the 'Programa Operativo de Crecimiento Inteligente' FEDER 2014-2020 (refs. ESFRI-2017-IAC-12 and ESFRI-2020-01-IAC-12) and Spanish Ministry of Science, Innovation and Universities, 15 per cent co-financed by 'Consejería de Economía, Industria, Comercio y Conocimiento' of the Gobierno de Canarias regional government. The Generalitat de Catalunya regional government is also gratefully acknowledged via its 'CERCA' program and grants 2021SGR00426 and 2021SGR00679. Spanish groups were also kindly supported by European Union funds via the Horizon Europe Research and innovation programme under grant agreement no. 101131928; NextGenerationEU, grants no. PRTR-C17.I1, CT19/23-INVM-109, and the 'MicroStars' ERC, ref. 101076533. This research used computing and storage resources provided by the Port d'Informació Científica (PIC) data center; Swedish Research Council, Royal Physiographic Society of Lund, Royal Swedish Academy of Sciences, The Swedish National Infrastructure for Computing (SNIC) at Lunarc (Lund), Sweden; State Secretariat for Education, Research and Innovation (SERI) and Swiss National Science Foundation (SNSF), Switzerland; The National Research Foundation of Ukraine (projects 2023.03/0149 and 2023.05/0024), Ukraine; Durham University, Leverhulme Trust, Liverpool University, University of Leicester, University of Oxford, Royal Society, Science and Technology Facilities Council, UK; U.S. National Science Foundation, U.S. Department of Energy, Argonne National Laboratory, Barnard College, University of California, University of Chicago, Columbia University, Georgia Institute of Technology, Institute for Nuclear and Particle Astrophysics (INPAC-MRPI program), Iowa State University, the Smithsonian Institution, VVD is funded by NSF grant AST-1911061, Washington University McDonnell Center for the Space Sciences, The University of Wisconsin and the Wisconsin Alumni Research Foundation, USA.

The research leading to these results has received funding from the European Union's Seventh Framework Programme (FP7/2007-2013) under grant agreement No 262053 and No 317446. This project is receiving funding from the European Union's Horizon 2020 research and innovation programs under agreement no 676134.

DATA AVAILABILITY

This research has made use of GAMMAPY[39] (F. Acero et al. 2024), a community-developed core Python package for TeV γ-ray astronomy, and of the CTAO instrument response functions (version PROD5-V0.1) provided by the CTA Consortium and Observatory[40] (CTAO Consortium 2021a). Most of the analysis is stored as publicly available notebooks in the Online Material (CTAO Consortium 2025). CLUMPY is licensed under the GNU General Public License (GPLv2).

REFERENCES

Aad G. et al., 2016, Phys. Lett. B, 757, 334
Aaltonen T. et al., 2012, Phys. Rev. D, 86, 112002
Abdallah H. et al., 2020, Phys. Rev. D, 102, 062001
Abdollahi S. et al., 2017, Phys. Rev. D, 95, 082007
Abramowski A. et al., 2014, Phys. Rev. D, 90, 112012
Acciari V. A. et al., 2022, Phys. Dark Univ., 35, 100912
Acero F. et al., 2024, Gammapy: Python Toolbox for Gamma-ray Astronomy, Zenodo, available at: https://doi.org/10.5281/zenodo.10726484
Ackermann M. et al., 2012, ApJS, 203, 4
Ackermann M. et al., 2014, Phys. Rev. D, 89, 042001
Ackermann M. et al., 2015, Phys. Rev. Lett., 115, 231301
Ackermann M. et al., 2017, ApJ, 840, 43
Aguirre-Santaella A., Sánchez-Conde M. A., 2024, MNRAS, 530, 2496
Aihara H. et al., 2018, PASJ, 70, S4
Albert A. et al., 2017, ApJ, 834, 110
Albert A. et al., 2018, ApJ, 853, 154
Alvarez-Gaumé L., Polchinski J., Wise M. B., 1983, Nucl. Phys. B, 221, 495
Amendola L., Tsujikawa S., 2010, Dark Energy: Theory and Observations. Cambridge Univ. Press, Cambridge
Ando S., Ishiwata K., 2015, J. Cosmol. Astorpart. Phys., 2015, 024
Ando S. et al., 2019, J. Cosmol. Astropart. Phys., 10, 040
Ando S., Ishiyama T., Hiroshima N., 2019, Galaxies, 7, 68
Ando S., Geringer-Sameth A., Hiroshima N., Hoof S., Trotta R., Walker M. G., 2020, Phys. Rev. D, 102, 061302
Archambault S. et al., 2017, Phys. Rev. D, 95, 082001
Arina C., Di Mauro M., Fornengo N., Heisig J., Jueid A., Ruiz de Austri R., 2024, J. Cosmol. Astorpart. Phys., 2024, 035
Arkani-Hamed N., Dimopoulos S., 2005, J. High Energy Phys., 2005, 073
Arkani-Hamed N., Finkbeiner D. P., Slatyer T. R., Weiner N., 2009, Phys. Rev. D, 79, 015014
Baer H., Tata X., 2022, Weak Scale Supersymmetry. Cambridge Univ. Press, Cambridge
Baes M., van Hese E., 2007, A&A, 471, 419
Baring M. G., Ghosh T., Queiroz F. S., Sinha K., 2016, Phys. Rev. D, 93, 103009
Barrio J. A. et al., 2020, Nucl. Instr. Methods Phys. Res. A, 952, 161588
Bartels R., Krishnamurthy S., Weniger C., 2016, Phys. Rev. Lett., 116, 051102
Bauer C. W., Rodd N. L., Webber B. R., 2021, J. High Energy Phys., 2021, 1
Bauer D. et al., 2015, Phys. Dark Univ., 7-8, 16

[39] See https://www.gammapy.org.
[40] See https://www.cta-observatory.org/science/ctao-performance/ for more details.

Bechtol K. et al., 2015, ApJ, 807, 50
Belokurov V. et al., 2006, ApJ, 647, L111
Beneke M., Bharucha A., Dighera F., Hellmann C., Hryczuk A., Recksiegel S., Ruiz-Femenia P., 2016, J. High Energy Phys., 03, 119
Bergström L., Ullio P., Buckley J. H., 1998, Astropart. Phys., 9, 137
Bertone G., Hooper D., 2018, Rev. Mod. Phys., 90, 045002
Bertschinger E., 1998, ARA&A, 36, 599
Bilton L. E., Pimbblet K. A., 2018, MNRAS, 481, 1507
Binney J., Tremaine S., 2008, Galactic Dynamics, 2nd edn. Princeton Univ. Press, Princeton
Birkedal A., Noble A., Perelstein M., Spray A., 2006, Phys. Rev. D, 74, 035002
Blanco C., Hooper D., 2019, J. Cosmol. Astorpart. Phys., 2019, 019
Boettcher E. et al., 2013, AJ, 146, 94
Bonnivard V., Combet C., Maurin D., Walker M. G., 2015a, MNRAS, 446, 3002
Bonnivard V. et al., 2015b, MNRAS, 453, 849
Bonnivard V. et al., 2015c, ApJ, 808, L36
Bonnivard V., Hütten M., Nezri E., Charbonnier A., Combet C., Maurin D., 2016a, Comput. Phys. Commun., 200, 336
Bonnivard V., Maurin D., Walker M. G., 2016b, MNRAS, 462, 223
Braun R., Bourke T., Green J. A., Keane E., Wagg J., 2015, Proc. Sci., Advancing Astrophysics with the Square Kilometre Array (AASKA14). SISSA, Trieste, PoS#174
Bringmann T., Weniger C., 2012, Phys. Dark Univ., 1, 194
Bringmann T., Doro M., Fornasa M., 2009, J. Cosmol. Astorpart. Phys., 2009, 016
Bringmann T., Calore F., Galea A., Garny M., 2017, J. High Energy Phys., 09, 041
Brown T. M. et al., 2012, ApJ, 753, L21
Burkert A., 1995, ApJ, 447, L25
Caldwell R., Kamionkowski M., 2009, Nature, 458, 587
Calore F., Cholis I., Weniger C., 2015, J. Cosmol. Astorpart. Phys., 2015, 038
Cao Z. et al., 2021, Nature, 594, 33
Cao Z. et al., 2024, Phys. Rev. Lett., 133, 061001
Carlson E., Profumo S., 2014, Phys. Rev. D, 90, 023015
Cembranos J. A. R., de la Cruz-Dombriz A., Gammaldi V., Lineros R. A., Maroto A. L., 2013, J. High Energy Phys., 09, 077
Cembranos J. A. R., De La Cruz-Dombriz Á., Gammaldi V., Méndez-Isla M., 2020, Phys. Dark Univ., 27, 100448
Chandra V. et al., 2022, ApJ, 940, 127
Charbonnier A. et al., 2011, MNRAS, 418, 1526
Charbonnier A., Combet C., Maurin D., 2012, Comput. Phys. Commun., 183, 656
Chiappo A., Cohen-Tanugi J., Conrad J., Strigari L. E., 2019, MNRAS, 488, 2616
Cholis I., Evoli C., Calore F., Linden T., Weniger C., Hooper D., 2015, J. Cosmol. Astorpart. Phys., 12, 005
Cholis I., Zhong Y.-M., McDermott S. D., Surdutovich J. P., 2022, Phys. Rev. D, 105, 103023
Cirelli M. et al., 2011, J. Cosmol. Astorpart. Phys., 03, 051
Cirelli M., Moulin E., Panci P., Serpico P. D., Viana A., 2012, Phys. Rev. D, 86, 083506
Cirelli M., Strumia A., Zupan J., 2024, preprint (arXiv:2406.01705)
Clowe D., Bradač M., Gonzalez A. H., Markevitch M., Randall S. W., Jones C., Zaritsky D., 2006, ApJ, 648, L109
Conn B. C., Jerjen H., Kim D., Schirmer M., 2018, ApJ, 852, 68
Coronado-Blázquez J., Doro M., Sánchez-Conde M. A., Aguirre-Santaella A., 2021, Phys. Dark Univ., 32, 100845
Crnogorčević M., Linden T., 2024, Phys. Rev. D, 109, 083018
Crocker R. M. et al., 2022, Nat. Astron., 6, 1317
CTAO Consortium, 2013, Astropart. Phys., 43, 3
CTAO Consortium, 2019, Science with the Cherenkov Telescope Array. World Scientific Publishing, Singapore
CTAO Consortium, 2021a, CTAO Instrument Response Functions - prod5 version v0.1, https://doi.org/10.5281/zenodo.5499840
CTAO Consortium, 2021b, J. Cosmol. Astorpart. Phys., 2021, 057
CTAO Consortium, 2023, MNRAS, 523, 5353
CTAO Consortium, 2024a, J. Cosmol. Astorpart. Phys., 2024, 047
CTAO Consortium, 2024b, J. Cosmol. Astorpart. Phys., 2024, 004
CTAO Consortium, 2024c, J. Cosmol. Astorpart. Phys., 2024, 081
CTAO Consortium, 2025, Supplementary Online Material [this work]. Zenodo platform, https://zenodo.org/records/17079907
Da Vela P., Stamerra A., Neronov A., Prandini E., Konno Y., Sitarek J., 2018, Astropart. Phys., 98, 1
Dall'Ora M. et al., 2012, ApJ, 752, 42
Dambis A. K., Berdnikov L. N., Kniazev A. Y., Kravtsov V. V., Rastorguev A. S., Sefako R., Vozyakova O. V., 2013, MNRAS, 435, 3206
Daylan T., Finkbeiner D. P., Hooper D., Linden T., Portillo S. K. N., Rodd N. L., Slatyer T. R., 2016, Phys. Dark Univ., 12, 1
de Jong J. T. A., Rix H. W., Martin N. F., Zucker D. B., Dolphin A. E., Bell E. F., Belokurov V., Evans N. W., 2008, AJ, 135, 1361
de Jong R. S. et al., 2019, The Messenger, 175, 3
de Naurois M., Mazin D., 2015, C. R. Phys., 16, 610
de Oña Wilhelmi E., López-Coto R., Aharonian F., Amato E., Cao Z., Gabici S., Hinton J., 2024, Nat. Astron., 8, 425
Dey A. et al., 2019, AJ, 157, 168
Diemand J., Kuhlen M., Madau P., Zemp M., Moore B., Potter D., Stadel J., 2008, Nature, 454, 735
Donath A. et al., 2023, A&A, 678, A157
Doro M., Sánchez-Conde M. A., Hütten M., 2021, preprint (arXiv:2111.01198)
Drlica-Wagner A. et al., 2015a, ApJ, 809, L4
Drlica-Wagner A. et al., 2015b, ApJ, 813, 109
Drlica-Wagner A. et al., 2016, ApJ, 833, L5
Drlica-Wagner A. et al., 2020, ApJ, 893, 47
Drlica-Wagner A., MagLiteS Team, 2017, in APS Meeting Abstracts, p. J5.001
Edwards T. D. P., Weniger C., 2017, preprint (arXiv:1712.05401)
Edwards T. D. P., Weniger C., 2018, J. Cosmol. Astorpart. Phys., 02, 021
Einasto J., 1965, Trudy Astrofizicheskogo Instituta Alma-Ata, 5, 87
Errani R., Navarro J. F., 2021, MNRAS, 505, 18
Errani R., Navarro J. F., Peñarrubia J., Famaey B., Ibata R., 2022, MNRAS, 519, 384
ESA ARRAKIHS Consortium, 2025, ARRAKIHS Phase 2 Report (v0.9.2), available at: https://www.cosmos.esa.int/documents/7423467/7423486/ESA-F2-ARRAKIHS-Phase-2-PUBLIC-v0.9.2.pdf
Evans N. W., Ferrer F., Sarkar S., 2004, Phys. Rev. D, 69, 123501
Faber S. M. et al., 2003, in Iye M., Moorwood A. F. M., eds, Proc. SPIE Conf. Ser., Vol. 4841, Instrument Design and Performance for Optical/Infrared Ground-based Telescopes, SPIE, Bellingham, p. 1657
Feng J. L., 2010, ARA&A, 48, 495
Feng J. L., Kaplinghat M., Yu H.-B., 2010, Phys. Rev. D, 82, 083525
Firth P., Drinkwater M. J., Karick A. M., 2008, MNRAS, 389, 1539
Fisher L. K. C., Goldstein I. S., Kumar J., Strigari L. E., 2025, preprint (arXiv:2508.03823)
Flaugher B., Bebek C., 2014, in Ramsay S. K., McLean I. S., Takami H., eds, Proc. SPIE Conf. Ser., Vol. 9147, Ground-based and Airborne Instrumentation for Astronomy V, SPIE, Bellingham, p. 91470S
Flewelling H. A. et al., 2020, ApJS, 251, 7
Fomin V. P., Stepanian A. A., Lamb R. C., Lewis D. A., Punch M., Weekes T. C., 1994, Astropart. Phys., 2, 137
Gaia Collaboration, 2018, A&A, 616, A12
Gaia Collaboration, 2020a, A&A, 637, C3
Gaia Collaboration, 2020b, A&A, 642, C1
Gao L., Frenk C. S., Jenkins A., Springel V., White S. D. M., 2012, MNRAS, 419, 1721
Garling C. et al., 2018, ApJ, 852, 44
Genina A., Fairbairn M., 2016, MNRAS, 463, 3630
Geringer-Sameth A., Koushiappas S. M., Walker M., 2015, ApJ, 801, 74
Gilmozzi R., Spyromilio J., 2007, The Messenger, 127, 11
Gondolo P., Gelmini G., 1991, Nucl. Phys. B, 360, 145
Harvey D., Massey R., Kitching T., Taylor A., Tittley E., 2015, Science, 347, 1462
Hayashi E. et al., 2004, MNRAS, 355, 794
Hayashi K., Chiba M., 2012, ApJ, 755, 145

Hayashi K., Chiba M., 2015, ApJ, 810, 22
Hayashi K., Ichikawa K., Matsumoto S., Ibe M., Ishigaki M. N., Sugai H., 2016, MNRAS, 461, 2914
Hernitschek N. et al., 2016, ApJ, 817, 73
Hernquist L., 1990, ApJ, 356, 359
Hiroshima N., Hayashida M., Kohri K., 2019, Phys. Rev. D, 99, 123017
Hisano J., Matsumoto S., Nojiri M. M., 2004, Phys. Rev. Lett., 92, 031303
Homma D. et al., 2016, ApJ, 832, 21
Homma D. et al., 2018, PASJ, 70, S18
Homma D. et al., 2019, PASJ, 71, 94
Hoof S., Geringer-Sameth A., Trotta R., 2020, J. Cosmol. Astorpart. Phys., 02, 012
Hooper D., Profumo S., 2007, Phys. Rep., 453, 29
Hütten M., Kerszberg D., 2022, Galaxies, 10, 92
Hütten M., Combet C., Maier G., Maurin D., 2016, J. Cosmol. Astorpart. Phys., 2016, 047
Hütten M., Combet C., Maurin D., 2019, Comput. Phys. Commun., 235, 336
Ibarra A., Tran D., Weniger C., 2013, Int. J. Mod. Phys. A, 28, 1330040
Ibata R. A., Wyse R. F. G., Gilmore G., Irwin M. J., Suntzeff N. B., 1997, AJ, 113, 634
Iocco F., Benito M., 2017, Phys. Dark Univ., 15, 90
Iocco F., Mangano G., Miele G., Pisanti O., Serpico P. D., 2009, Phys. Rep., 472, 1
Iorio G. et al., 2023, MNRAS, 524, 426
Irwin M., Hatzidimitriou D., 1995, MNRAS, 277, 1354
Ivezić Ž. et al., 2019, ApJ, 873, 111
Jin S. et al., 2023, MNRAS, 530, 2688
Jones M. G., Bennet P., Mutlu-Pakdil B., Sand D. J., Spekkens K., Crnojević D., Karunakaran A., Zaritsky D., 2021, ApJ, 919, 72
Jungman G., Kamionkowski M., Griest K., 1996, Phys. Rep., 267, 195
Kar A., Mitra S., Mukhopadhyaya B., Choudhury T. R., Tingay S., 2019, Phys. Rev. D, 100, 043002
Karczmarek P. et al., 2015, AJ, 150, 90
Karukes E. V., Benito M., Iocco F., Trotta R., Geringer-Sameth A., 2020, J. Cosmol. Astorpart. Phys., 2020, 033
Kazantzidis S., Mayer L., Mastropietro C., Diemand J., Stadel J., Moore B., 2004, ApJ, 608, 663
Kelley T., Bullock J. S., Garrison-Kimmel S., Boylan-Kolchin M., Pawlowski M. S., Graus A. S., 2019, MNRAS, 487, 4409
Khachatryan V. et al., 2015, Eur. Phys. J. C, 75, 235
Kim D., Jerjen H., 2015, ApJ, 808, L39
Kim D. et al., 2016, ApJ, 833, 16
Kirby E. N., Cohen J. G., Simon J. D., Guhathakurta P., Thygesen A. O., Duggan G. E., 2017, ApJ, 838, 83
Knödlseder J. et al., 2016, A&A, 593, A1
Koch A. et al., 2009, ApJ, 690, 453
Koposov S. E. et al., 2011, ApJ, 736, 146
Koposov S. E. et al., 2015b, ApJ, 811, 62
Kuhlen M., Vogelsberger M., Angulo R., 2012, Phys. Dark Univ., 1, 50
Koposov S. E. et al., 2018, MNRAS, 479, 5343
Koposov S. E., Belokurov V., Torrealba G., Evans N. W., 2015a, ApJ, 805, 130
Kunz M., 2012, C. R. Phys., 13, 539
Lacroix T., Silk J., Moulin E., BÅ‘hm C., 2016, Phys. Rev. D, 94, 123008
Laevens B. P. M. et al., 2015a, ApJ, 802, L18
Laevens B. P. M. et al., 2015b, ApJ, 813, 44
Lee B. W., Weinberg S., 1977, Phys. Rev. Lett., 39, 165
Lee S. K., Lisanti M., Safdi B. R., Slatyer T. R., Xue W., 2016, Phys. Rev. Lett., 116, 051103
Lelli F., McGaugh S. S., Schombert J. M., 2016, AJ, 152, 157
Li M., Li X.-D., Wang S., Wang Y., 2011, Commun. Theor. Phys., 56, 525
Longeard N. et al., 2020, MNRAS, 491, 356
LST Coll., 2019, in Proc. Sci., 36th International Cosmic Ray Conference (ICRC2019), SISSA, Trieste, PoS#653.
Macias O., Gordon C., Crocker R. M., Coleman B., Paterson D., Horiuchi S., Pohl M., 2018, Nat. Astron., 2, 387
MAGIC Collaboration, 2020, A&A, 635, A158
Majewski S. R., Skrutskie M. F., Weinberg M. D., Ostheimer J. C., 2003, ApJ, 599, 1082
Makarova L. N., Makarov D. I., Karachentsev I. D., Tully R. B., Rizzi L., 2017, MNRAS, 464, 2281
Maldacena J. M., 1998, Adv. Theor. Math. Phys., 2, 231
Markwardt C. B., 2009, in Bohlender D. A., Durand D., Dowler P., eds, ASP Conf. Ser., Vol. 411, Astronomical Data Analysis Software and Systems XVIII, p. 251
Martin N. F. et al., 2015, ApJ, 804, L5
Martin N. F., de Jong J. T. A., Rix H.-W., 2008, ApJ, 684, 1075
Martinez G. D., 2015, MNRAS, 451, 2524
Martínez-Vázquez C. E. et al., 2015, MNRAS, 454, 1509
Mateo M., Bailey J. I., Crane J., Shectman S., Thompson I., Roederer I., Bigelow B., Gunnels S., 2012, in McLean I. S., Ramsay S. K., Takami H., eds, Proc. SPIE Conf. Ser., Vol. 8446, Ground-based and Airborne Instrumentation for Astronomy IV, SPIE, Bellingham, p. 84464Y
Mau S. et al., 2020, ApJ, 890, 136
Mayer L., 2010, Adv. Astron., 2010, 278434
McConnachie A. W., 2012, AJ, 144, 4
McDaniel A., Ajello M., Karwin C. M., Di Mauro M., Drlica-Wagner A., Sànchez-Conde M. A., 2024, Phys. Rev. D, 109, 063024
Medina G. E. et al., 2018, ApJ, 855, 43
Mellier Y. et al., 2025, A&A, 697, A1
Moliné Á., Sánchez-Conde M. A., Palomares-Ruiz S., Prada F., 2017, MNRAS, 466, 4974
Mollitor P., Nezri E., Teyssier R., 2015, MNRAS, 447, 1353
Montanari A., Moulin E., 2024, Searching for Dark Matter with Imaging Atmospheric Cherenkov Telescopes. Springer, Cham
Muñoz R. R., Geha M., Willman B., 2010, AJ, 140, 138
Musella I. et al., 2009, ApJ, 695, L83
Mutlu-Pakdil B. et al., 2018, ApJ, 863, 25
Navarro J. F., Frenk C. S., White S. D. M., 1997, ApJ, 490, 493
Newton O., Cautun M., Jenkins A., Frenk C. S., Helly J., 2018, MNRAS, 479, 2853
Neyman J. et al., 1933, Philos. T. R. Soc. Lond. Ser. A , 231, 289
Nidever D. L., SMASH, 2017, in American Astronomical Society Meeting Abstracts, Vol. 229, p. 416.04
O'Mullane W., Hazell A., Bennett K., Bartelmann M., Vuerli C., 2000, in Manset N., Veillet C., Crabtree D., eds, ASP Conf. Ser. Vol. 216, Astronomical Data Analysis Software and Systems IX, p. 419
Okamoto S., Arimoto N., Yamada Y., Onodera M., 2012, ApJ, 744, 96
Pace A. B., Strigari L. E., 2019, MNRAS, 482, 3480
Particle Data Group, 2020, Prog. Theor. Exp. Phys., 2020, 083C01
Peñarrubia J., Benson A. J., Walker M. G., Gilmore G., McConnachie A. W., Mayer L., 2010, MNRAS, 406, 1290
Petrović J., Serpico P. D., Zaharijaš G., 2014, J. Cosmol. Astorpart. Phys., 2014, 052
Pianta C., Capuzzo-Dolcetta R., Carraro G., 2022, ApJ, 939, 3
Pinzke A., Pfrommer C., Bergström L., 2011, Phys. Rev. D, 84, 123509
Planck Collaboration I, 2014, A&A, 571, A1
Planck Collaboration XIII, 2016, A&A, 594, A13
Riess A. G. et al., 2004, ApJ, 607, 665
Ripepi V. et al., 2014, MNRAS, 437, 2307
Royer F., Jégouzo I., Haigron R., Tajahmady F., Plassard F., 2014, The Messenger, 158, 21
Ruhland C., Bell E. F., Rix H.-W., Xue X.-X., 2011, ApJ, 731, 119
Sánchez E., DES Collaboration], 2016, Nucl. Part. Phys. Proc., 273-275, 302
Sánchez-Conde M. A., Prada F., 2014, MNRAS, 442, 2271
Sánchez-Conde M. A., Cannoni M., Zandanel F., Gómez M. E., Prada F., 2011, J. Cosmol. Astorpart. Phys., 2011, 011
Sand D. J., Strader J., Willman B., Zaritsky D., McLeod B., Caldwell N., Seth A., Olszewski E., 2012, ApJ, 756, 79
Sesar B. et al., 2014, ApJ, 793, 135
Shapley H., 1938, Harvard College Obs. Bull., 908, 1
Simon J. D., Geha M., 2007, ApJ, 670, 313
Simon J. D. et al., 2011, ApJ, 733, 46
Simon J. D. et al., 2015, ApJ, 808, 95

Simon J. D. et al., 2020, ApJ, 892, 137
Smirnov J., Beacom J. F., 2019, Phys. Rev. D, 100, 043029
Smith S. E. T. et al., 2024, ApJ, 961, 92
Spencer M. E., Mateo M., Walker M. G., Olszewski E. W., McConnachie A. W., Kirby E. N., Koch A., 2017, AJ, 153, 254
Spencer M. E., Mateo M., Olszewski E. W., Walker M. G., McConnachie A. W., Kirby E. N., 2018, AJ, 156, 257
Springel V. et al., 2008, MNRAS, 391, 1685
Srednicki M., Watkins R., Olive K. A., 1988, Nucl. Phys. B, 310, 693
Steigman G., Dasgupta B., Beacom J. F., 2012, Phys. Rev. D, 86, 023506
Stetson P. B., Fiorentino G., Bono G., Bernard E. J., Monelli M., Iannicola G., Gallart C., Ferraro I., 2014, PASP, 126, 616
Strigari L. E., Bullock J. S., Kaplinghat M., Simon J. D., Geha M., Willman B., Walker M. G., 2008, Nature, 454, 1096
Strigari L. E., Koushiappas S. M., Bullock J. S., Kaplinghat M., Simon J. D., Geha M., Willman B., 2008, ApJ, 678, 614
Torrealba G., Koposov S. E., Belokurov V., Irwin M., 2016a, MNRAS, 459, 2370
Torrealba G. et al., 2016b, MNRAS, 463, 712
Torrealba G. et al., 2018, MNRAS, 475, 5085
Torrealba G. et al., 2019, MNRAS, 488, 2743
Tagliaferri G. et al., 2022, in Marshall H. K., Spyromilio J., Usuda T., eds, Proc. SPIE Conf. Ser., Vol. 12182, Ground-based and Airborne Telescopes IX. SPIE, Bellingham, p. 121820K
Tully R. B. et al., 2013, AJ, 146, 86
Valcheva A. T., Ovcharov E. P., Lalova A. D., Nedialkov P. L., Ivanov V. D., Carraro G., 2015, MNRAS, 446, 730
van Albada T. S., Sancisi R., 1986, Philos. T. R. Soc. Lond. Ser. A, 320, 447
Venville T. A. A., Duffy A. R., Crocker R. M., Macias O., Tepper-García T., 2024, MNRAS, 527, 5324
Viana A. et al., 2012, ApJ, 746, 77
Walker M. G., Mateo M., Olszewski E. W., 2009a, AJ, 137, 3100
Walker M. G., Mateo M., Olszewski E. W., Peñarrubia J., Wyn Evans N., Gilmore G., 2009c, ApJ, 704, 1274
Walker M. G., Mateo M., Olszewski E. W., Sen B., Woodroofe M., 2009b, AJ, 137, 3109
Walker M. G., Olszewski E. W., Mateo M., 2015a, MNRAS, 448, 2717
Walker M. G., Mateo M., Olszewski E. W., Bailey, John I. I., Koposov S. E., Belokurov V., Evans N. W., 2015b, ApJ, 808, 108
Watkins L. L., van der Marel R. P., Sohn S. T., Evans N. W., 2019, ApJ, 873, 118
Weekes T. C. et al., 1989, ApJ, 342, 379
Wilks S. S., 1938, Ann. Math. Stat., 9, 60
Willman B., Strader J., 2012, AJ, 144, 76
Willman B., Geha M., Strader J., Strigari L. E., Simon J. D., Kirby E., Ho N., Warres A., 2011, AJ, 142, 128
York D. G. et al., 2000, AJ, 120, 1579
Yuan Q., Zhang B., 2014, J. High Energy Astrophys., 3, 1
Zanin R. et al., 2022, in Proc. Sci., 37th International Cosmic Ray Conference. SISSA, Trieste, PoS#005
Zavala J., Frenk C. S., 2019, Galaxies, 7, 81
Zeldovich Y. B., Klypin A., Khlopov M. Y., Chechetkin V. M., 1980, Sov. J. Nucl. Phys., 31, 664
Zhao H., 1996, MNRAS, 278, 488

APPENDIX A: DERIVATION OF THE ASTROPHYSICAL FACTORS FOR THE CTAO OPTIMAL DSPHS

Hereafter, we describe the details of the input data sets and the operational set-up of the MCMC Jeans analysis that has been performed with the CLUMPY software in order to make the target selection and derive the astrophysical factors of the optimal dSphs for the DM searches with CTA. This appendix completes the information reported in Section 2.2.

A1 Original source selection and discarded targets

In Section 2.2, we have presented our target selection based on distance criteria and quality of stellar information. Out of a starting sample of 64 dSphs candidates, we have narrowed down the initial list first to 35 surviving candidates, reported in Table 2 and with a second selection to 14 plausible targets for both hemispheres, reported in Table 3. For completeness, we also report in Table A1, the list of 29 targets that were excluded according to the first selection cut.

A2 CLUMPY set-up for the computation of the astrophysical factors

We follow the prescriptions by V. Bonnivard et al. (2015b) to derive the astrophysical factors of dSph haloes in a self-consistent and conservative way. In Section 2.2, we have discussed the retrieval of the stellar information for each target from literature data of the 35 targets that survived our first selection cut.

A2.1 Brightness profiles

For these selected targets, we attempted a fit the brightness density $n^*(r)$ of each galaxy with a 3D Zhao–Hernquist profile (L. Hernquist 1990; H. Zhao 1996):

$$n^*(r) = \frac{n_s^*}{\left(\frac{r}{r_s^*}\right)^{\gamma^*}\left[1+\left(\frac{r}{r_s^*}\right)^{\alpha^*}\right]^{\frac{\beta^*-\gamma^*}{\alpha^*}}}, \tag{A1}$$

projected onto the corresponding circularized[41] 2D surface brightness profile $\Sigma(r)$. The spatial distribution of the baryonic content over the dSph volume inferred in this way is used in CLUMPY as a proxy for the DM spatial distribution to solve the Jeans equation (5).

We performed this fit using the IDL package MPFIT (C. B. Markwardt 2009), requesting that the final profiles give finite numbers of stars – and hence finite dSph brightnesses – once integrated up to infinity. This in turn translates to constraints on the inner slopes $\gamma^* < 3$ and outer slopes $\beta^* > 3$. Such choices forced us to remove Segue 2, Tucana II, Tucana III, and Tucana IV from the sample of optimal targets, since no binned surface brightness data were at present available for these dSphs, and Boötes II, for which no profile with finite luminosity can be obtained.[42]

A2.2 Stellar kinematics

For the dSph stellar kinematics, we were forced to remove from the analysis those candidates that did not have adequately populated stellar samples to obtain a significant MCMC fit, i.e. the targets with number of confirmed member stars $N_{\rm mem} < N_{\rm par}$ ($N_{\rm par}$ being the number of free parameters in the fitting procedure, which is set to 7: 3 for the DM density profile, and 4 for the velocity anisotropy in our framework). This further constraint led us to exclude Boötes III, Carina II, Carina III, Laevens 3, Cetus II, Eridanus III, Horologium I, Horologium II, Indus I, Pictor I, Phoenix II, Tucana V, and Virgo I, since such targets had no spectroscopic measurements or

[41] $r_{\rm circ} = r\sqrt{1-\epsilon}$, with ϵ the dSph eccentricity.
[42] This is hinting to a severe tidal disruption of the Boötes II baryonic content, due to its potential association with the Sagittarius stellar stream (V. Chandra et al. 2022), although an inaccurate measurement of the surface brightness due to its intrinsic faintness (N. F. Martin et al. 2008) is equally possible.

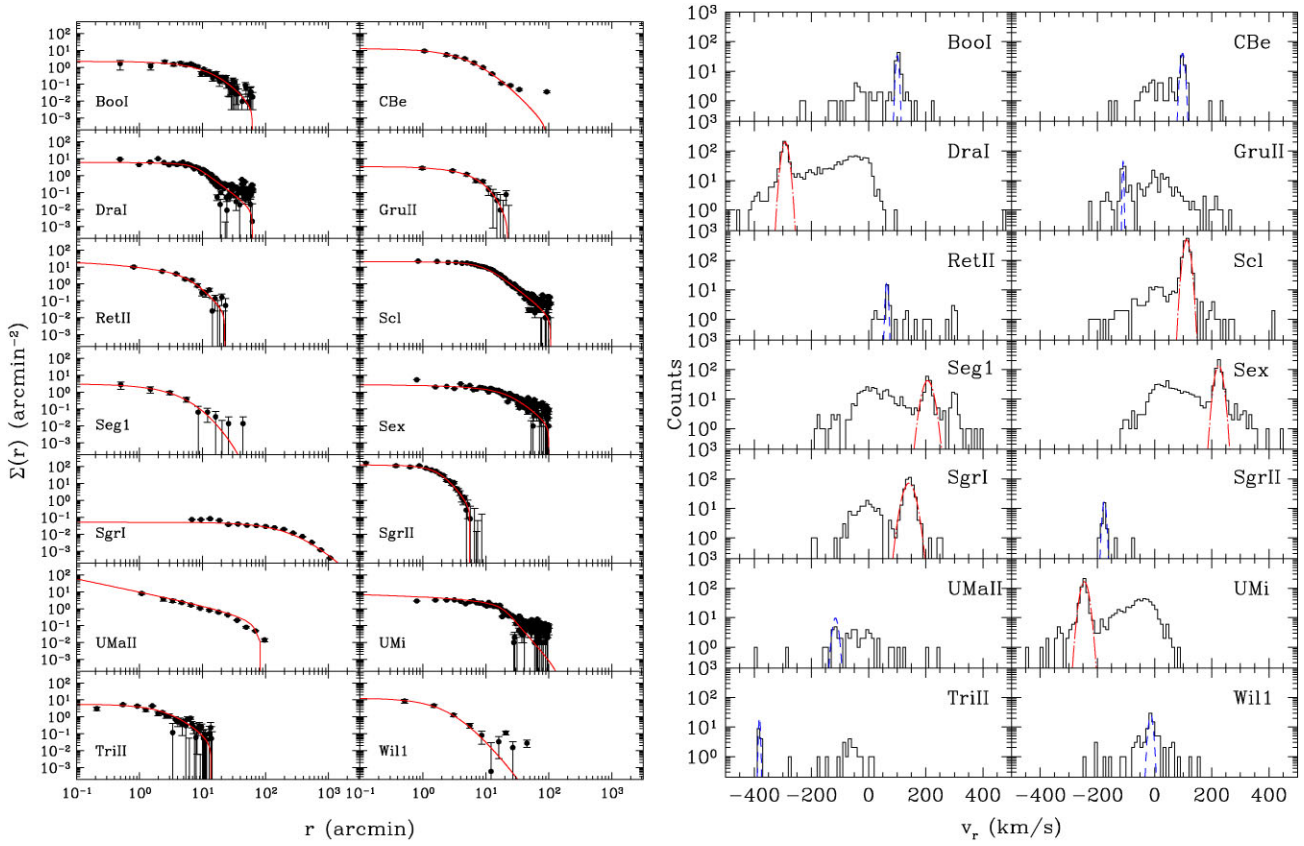

Figure A1. Left panels: best-fitting integrated brightness profiles $\Sigma(r)$ of the dSphs that pass the selection on the astrometric data availability as a function of the object's projected (2D) radial coordinate r from the dSph centroid. In each panel, the projected 3D profile resulting from the fit (red line) is shown superimposed on the corresponding background-subtracted data set (black dots). Right panels: distributions of radial velocities for the most updated stellar samples available for each optimal dSph (black solid histograms; see Table A2 for the references). For each dSph, a Gaussian is shown to represent the velocity distribution of confirmed member stars obtained either from the application of the EM algorithm by M. G. Walker et al. (2009b, red dot–dashed lines) or from the binary classification extracted from the relevant literature (blue dashed lines; see Table A2 for the references).

spectroscopic samples containing $\leq$5 member candidates (A. Koch et al. 2009; S. E. Koposov et al. 2015b).

To take into account non-radial components of the stellar velocities – that hint to a partial, although not dominant, rotational support of the dSph structure – we adopted in CLUMPY the most conservative priors by V. Bonnivard et al. (2015a) for the treatment of the velocity anisotropy, using the Baes & van Hese profile (M. Baes & E. van Hese 2007):

$$\beta_{\rm ani}(r) = \frac{\beta_0 + \beta_\infty (r/r_a)^\eta}{1 + (r/r_a)^\eta}\,, \tag{A2}$$

with four free parameters (central anisotropy β_0, asymptotic anisotropy β_∞, anisotropy scale radius r_a, and sharpness index η).

A2.3 Stellar association

To select only fiducial member stars for each target, we processed the stellar kinematics data sets of the classical dSphs, plus those of Segue 1 and Sagittarius I, through the expectation–maximization (EM) algorithm by M. G. Walker et al. (2009b). We also applied additional static cuts on the spectroscopic stellar parameters in the case of Draco I (M. G. Walker et al. 2015a) and Segue 1 (V. Bonnivard et al. 2016b). This procedure was feasible only for those objects that had sufficiently populated ($N \gtrsim 100$) stellar samples; for the remaining ultrafaint dSphs, we adopted binary (0/1) memberships already available in the literature. It is to be noted that no spatial cuts were applied to the data that were processed with the EM algorithm: in fact, since for all targets we aim at computing precise astrophysical factor profiles up to large angular distances from the dSph centroid in order to exploit the large FoV of the CTAO telescopes (see Section 2.2), we did not preliminarily remove any candidate member star based on their coordinates. This is clearly biasing the $J_{\rm ann}$ and $J_{\rm dec}$ calculation for some sources, like Sagittarius I, that show significant non-equilibrium features; nevertheless, we maintain them in our analysed sample flagging them adequately (see Table A5).

Due to the relatively low number of members (<50) for many of the analysed dSphs, we chose the CLUMPY unbinned analysis method (V. Bonnivard et al. 2015b, c), which runs over the velocity data of the single member stars. After this selection, we were left with a sample of 14 targets; for them, the brightness profiles and the distribution of stellar velocities are reported in Fig. A1. We report the number of member stars identified in this way for such dSphs in Table A2. Note that the scale number density n_s^* in equation (A1) has been converted to a brightness density ρ_s^* scaling the volume integral of the stellar number density profile to the dSph V-band absolute magnitude.

A2.4 DM density profiles

To compute the DM density profiles, we chose both a cuspy Einasto profile (J. Einasto 1965) with three free parameters (DM scale density

Table A1. Same as Table 2, but for those targets that do not satisfy our first selection cut (in alphabetical order).

Name	Abbr.	Type	RA (hh mm ss)	Dec. (dd mm ss)	Distance (kpc)	ZA_{culm} N (deg)	ZA_{culm} S (deg)	Month	Ref.
Andromeda XVIII	AndXVIII	uft	00 02 14.5	+ 45 05 20	1330 ± 104	16.3	69.7	Sept	1,2
Antlia II	AntII	uft	09 35 33.7	−36 46 12	132 ± 6	65.8	12.5	Feb	3
Aquarius II	AqrII	uft	22 33 55.1	−09 19 48	108 ± 3	38.3	15.8	Aug	4
Boötes IV	BoöIV	uft	15 34 45.5	+ 43 43 48	209 ± 20	14.2	67.5	May	5
Canes Venatici I	CVnI	uft	13 28 03.5	+ 33 33 21	216 ± 8	4.8	58.2	Apr	1,6
Canes Venatici II	CVnII	uft	12 57 10.0	+ 34 19 15	159 ± 8	5.6	58.9	Apr	1,6
Carina I	CarI	cls	06 41 36.7	−50 57 58	106 ± 1	79.7	26.3	Dec	1,7
Centaurus I	CenI	uft	12 38 21.5	−40 54 00	116 ± 2	70.0	16.7	Apr	8
Cetus I	CetI	uft	00 26 11.0	−11 02 40	748 ± 31	39.8	13.6	Sept	1,9
Cetus III	CetIII	uft	02 05 19.3	−04 16 12	251 ± 19	32.5	20.8	Oct	10
Columba I	ColI	uft	05 31 26.4	−28 01 48	182 ± 18	56.8	3.4	Dec	11
Crater II	CrtII	uft	11 49 14.5	−18 24 36	118 ± 1	47.5	5.8	Mar	12
Eridanus II	EriII	uft	03 44 21.5	−43 31 48	330 ± 16	72.3	18.9	Nov	13
Fornax	For	cls	02 39 59.3	−34 26 57	146 ± 1	63.2	9.8	Oct	1,7
Grus I	GruI	uft	22 56 42.4	−50 09 48	120 ± 17	78.9	25.5	Sept	14
Hercules	Her	uft	16 31 02.0	+ 12 47 30	137 ± 11	16.0	37.4	May	1,15
Hydra II	HyaII	uft	12 21 42.1	−31 59 07	134 ± 10	60.7	7.4	Mar	16
Indus II	IndII	uft	20 38 52.8	−46 09 36	214 ± 16	74.9	21.5	Aug	11
Leo I	LeoI	cls	10 08 28.1	+ 12 18 23	272 ± 10	16.5	36.9	Feb	1,17
Leo II	LeoII	cls	11 13 28.8	+ 22 09 06	240 ± 9	6.6	46.8	Mar	1,18
Leo IV	LeoIV	uft	11 32 57.0	−00 32 00	151 ± 4	29.3	24.1	Mar	1,19
Leo V	LeoV	uft	11 31 09.6	+ 02 13 12	169 ± 5	26.5	26.9	Mar	1,19
Leo T	LeoT	uft	09 34 53.4	+ 17 03 05	377 ± 28	11.7	41.7	Feb	1,20
Pegasus III	PegIII	uft	22 24 25.2	+ 05 24 36	215 ± 12	22.5	40.0	Aug	21
Phoenix I	PheI	uft	01 51 06.3	−44 26 41	427 ± 31	73.2	19.8	Oct	1,20
Pictor I	PicI	uft	04 43 48.0	−50 16 48	126 ± 24	79.0	25.7	Nov	13
Pisces II	PscII	uft	22 58 31.0	+ 05 57 09	182 ± 13	22.8	30.6	Sept	1,22
Tucana I	TucI	uft	22 41 49.6	−64 25 10	855 ± 35	–	39.8	Sept	1,9
Ursa Major I	UMaI	uft	10 34 52.8	+ 51 55 12	105 ± 2	23.2	76.6	Mar	1,23

Notes. References: [1]A. W. McConnachie (2012), [2]L. N. Makarova et al. (2017), [3]G. Torrealba et al. (2019), [4]G. Torrealba et al. (2016b), [5]D. Homma et al. (2019), [6]S. Okamoto et al. (2012), [7]P. Karczmarek et al. (2015), [8]S. Mau et al. (2020), [9]A. K. Dambis et al. (2013), [10]D. Homma et al. (2018), [11]A. Drlica-Wagner et al. (2015b), [12]G. Torrealba et al. (2016a), [13]K. Bechtol et al. (2015), [14]S. E. Koposov et al. (2015a), [15]C. Garling et al. (2018), [16]N. F. Martin et al. (2015), [17]P. B. Stetson et al. (2014), [18]R. B. Tully et al. (2013), [19]G. E. Medina et al. (2018), [20]V. Ripepi et al. (2014), [21]D. Kim et al. (2016), [22]D. J. Sand et al. (2012), and [23]T. M. Brown et al. (2012).

ρ_s, DM scale radius r_s, and DM sharpness index α), and a cored Burkert profile (A. Burkert 1995) with only scale density and radius as free parameters (see equation 6). Such choices imply MCMC fits with a total of 7 and 6 free parameters, respectively. The priors adopted for such free parameters are the same listed in V. Bonnivard et al. (2015a). On such parameter sets, we run 200 independent MC chains of 10^5 realizations each for every target. From the resulting posterior distributions of profile parameters, we derive their average best-fitting values, reporting them in Tables A3 and A4 along with the corresponding uncertainties at 68 per cent CL.

A2.5 Tidal radii

We then derived the distribution of tidal radii $R_{\rm tid}$ for each dSph from the output profiles as made by V. Bonnivard et al. (2015b), iteratively solving the tidal equation (V. Springel et al. 2008; P. Mollitor et al. 2015):

$$R_{\rm tid} = \left[\frac{M_{\rm dSph}}{\left(2 - \frac{{\rm d}\ln M_{\rm MW}}{{\rm d}\ln r}\Big|_{d_{\rm GC}} \right) \cdot M_{\rm MW}(< d_{\rm GC})} \right]^{1/3} \times d_{\rm GC}\,, \quad \text{(A3)}$$

where $M_{\rm dSph}$ is the total dSph DM mass, $M_{\rm MW}$ is the MW mass (here assumed to be 10^{12} $M_\odot$; L. L. Watkins et al. 2019), and $d_{\rm GC}$ is the dSph Galactocentric distance (A. W. McConnachie 2012). We also report the average values of $R_{\rm tid}$, along with the corresponding uncertainties at 68 per cent CL, in Tables A3 and A4 for the two adopted DM density profiles, respectively.

A2.6 Boost to the astrophysical factors from DM substructures

N-body simulations and the cold, collisionless nature of WIMPs predict that MW-like DM haloes form by hierarchical clustering of smaller substructures, that are generally referred to as DM subhaloes (M. Kuhlen, M. Vogelsberger & R. Angulo 2012; J. Zavala & C. S. Frenk 2019). The effect of substructures on DM searches has been subject to strong debates in the past (e.g. A. Pinzke, C. Pfrommer & L. Bergström 2011; M. A. Sánchez-Conde et al. 2011; L. Gao et al. 2012; M. A. Sánchez-Conde & F. Prada 2014; Á. Moliné et al. 2017; S. Ando et al. 2019). Depending on the target, the subhalo contribution can in fact strongly increase the astrophysical factor in the annihilation case where the signal yield depends on the integration of a squared DM density from extremely compact and dense subhaloes (see equation 3). Such a contribution is modelled according to the subhalo number density, the subhalo radial distribution within the host halo, and the so-called concentration parameter. Such functions are obtained using data from N-body simulations such as *Via Lactea II* and *Aquarius* (J. Diemand et al. 2008; V. Springel et al. 2008; A. Aguirre-Santaella & M. A. Sánchez-

Table A2. Parameters of the 3D brightness profiles (see Fig. A1) for the selected dSphs.

Name	Site	M_V (mag)	ϵ	ρ_s^* (10^5 $L_\odot$ kpc^{-3})	r_s^* (kpc)	α^*	β^*	γ^*	Ref.
BoöI	N	-6.3 ± 0.2	0.39 ± 0.06	1.14 ± 0.21	0.461 ± 0.021	1.1	7.7	0.0	1,2
CBe	N	-4.1 ± 0.5	0.38 ± 0.14	1.08 ± 0.50	0.0740 ± 0.0035	1.1	5.4	0.0	1,3
DraI	N	-8.8 ± 0.3	0.31 ± 0.02	4.5 ± 1.3	0.1473 ± 0.0079	6.8	3.8	0.0	1,4
GruII	S	-3.9 ± 0.2	~ 0.2	1.58 ± 0.29	0.166 ± 0.016	1.3	7.6	0.0	5
RetII	S	-3.6 ± 0.2	0.6 ± 0.2	2.04 ± 0.19	0.0408 ± 0.0026	3.5	4.7	1.1	6
Scl	S	-11.1 ± 0.5	0.32 ± 0.03	23 ± 11	0.2100 ± 0.0050	3.2	4.0	0.6	1,4
Seg1	N	-1.5 ± 0.8	0.48 ± 0.13	1.21 ± 0.89	0.0739 ± 0.0064	1.1	9.2	0.2	1,7
Sex	S	-9.3 ± 0.5	0.35 ± 0.05	0.56 ± 0.26	0.493 ± 0.018	2.7	4.0	0.6	1,4
SgrI	S	-13.5 ± 0.3	0.64 ± 0.02	0.277 ± 0.076	1.869 ± 0.060	1.1	4.9	0.0	1,8
SgrII	S	-5.2 ± 0.4	~ 0.2	42.9 ± 3.9	0.0371 ± 0.0028	3.5	5.7	0.1	9,10
TriII	N	-1.8 ± 0.5	~ 0.2	7.3 ± 3.4	0.0342 ± 0.0023	1.2	5.3	0.0	11
UMaII	N	-4.2 ± 0.6	0.63 ± 0.05	49.4 ± 27.3	0.0265 ± 0.0015	0.1	2.1	2.0	1,3
UMi	N	-8.8 ± 0.5	0.56 ± 0.05	21.7 ± 10.0	0.336 ± 0.010	4.0	7.3	0.7	1,4
Wil1	N	-2.7 ± 0.8	0.47 ± 0.08	4.4 ± 3.3	0.0251 ± 0.0046	1.2	5.9	0.0	1,7

Notes. References: [1]A. W. McConnachie (2012); [2]V. Belokurov et al. (2006); [3]R. R. Muñoz, M. Geha & B. Willman (2010); [4]M. Irwin & D. Hatzidimitriou (1995); [5]A. Drlica-Wagner et al. (2015b); [6]K. Bechtol et al. (2015); [7]N. F. Martin, J. T. A. de Jong & H.-W. Rix (2008); [8]S. R. Majewski et al. (2003); [9]B. P. M. Laevens et al. (2015b); [10]B. Mutlu-Pakdil et al. (2018); [11]B. P. M. Laevens et al. (2015a); [12]S. E. Koposov et al. (2011); [13]J. D. Simon & M. Geha (2007); [14]M. G. Walker et al. (2015a); [15]J. D. Simon et al. (2020); [16]M. G. Walker et al. (2015b); [17]M. G. Walker et al. (2009a); [18]J. D. Simon et al. (2011); [19]R. A. Ibata et al. (1997); [20]N. Longeard et al. (2020); [21]E. N. Kirby et al. (2017); [22]M. E. Spencer et al. (2018); and [23]B. Willman et al. (2011).

Table A3. Average best-fitting Einasto profile parameters for the sample of optimal dSphs.

Name	ρ_s (10^7 $M_\odot$ kpc^{-3})	r_s (kpc)	α	$R_{\rm tid}$ (kpc)	$\chi^2/n_{\rm d.o.f.}$
CBe	4.3 ± 2.8	$6.1^{+4.1}_{-5.7}$	$0.60^{+0.32}_{-0.24}$	$6.3^{+19.0}_{-4.3}$	76.3/52
Dral	$1.3^{+1.6}_{-1.0}$	$0.91^{+0.89}_{-0.33}$	$0.25^{+0.23}_{-0.10}$	$4.83^{+1.16}_{-0.83}$	642.9/462
RetII	$4.2^{+6.7}_{-3.3}$	$0.47^{+3.26}_{-0.33}$	$0.63^{+0.23}_{-0.31}$	$1.7^{+4.5}_{-1.0}$	21.5/11
Scl	$6.1^{+3.4}_{-2.6}$	$0.31^{+0.12}_{-0.10}$	$0.54^{+0.30}_{-0.31}$	$2.95^{+0.55}_{-0.30}$	1501.4/1113
SgrII	$9.4^{+20.9}_{-9.2}$	$0.49^{+4.80}_{-0.41}$	$0.45^{+0.34}_{-0.25}$	$3.7^{+13.9}_{-2.7}$	27.7/14
UMaII	$1.7^{+13.6}_{-1.4}$	$0.96^{+1.68}_{-0.80}$	$0.56^{+0.35}_{-0.36}$	$2.1^{+1.7}_{-1.0}$	30.9/13
UMi	$0.80^{+0.92}_{-0.51}$	$3.8^{+3.3}_{-1.5}$	$0.53^{+0.25}_{-0.20}$	$14.7^{+6.6}_{-4.1}$	682.4/460
Wil1	23^{+82}_{-21}	$0.12^{+2.25}_{-0.10}$	$0.39^{+0.38}_{-0.20}$	$1.20^{+4.08}_{-0.51}$	52.1/37

Table A4. Average best-fitting Burkert profile parameters for the sample of optimal dSphs.

Name	ρ_s (10^7 $M_\odot$ kpc^{-3})	r_s (kpc)	$R_{\rm tid}$ (kpc)	$\chi^2/n_{\rm d.o.f.}$
CBe	57^{+22}_{-27}	$1.7^{+3.7}_{-1.6}$	19^{+55}_{-16}	76.3/53
Dral	38^{+24}_{-16}	$0.32^{+0.15}_{-0.10}$	$4.30^{+0.86}_{-0.54}$	643.5/463
RetII	38^{+55}_{-21}	$0.28^{+5.32}_{-0.22}$	$5.8^{+19.3}_{-5.1}$	21.6/12
Scl	$40.8^{+8.4}_{-8.9}$	$0.247^{+0.048}_{-0.026}$	$3.71^{+0.30}_{-0.18}$	1501.6/1114
SgrII	260^{+140}_{-170}	$0.36^{+2.52}_{-0.31}$	$4.2^{+36.4}_{-2.8}$	27.9/15
UMaII	16^{+181}_{-13}	$0.43^{+3.60}_{-0.34}$	$2.2^{+6.5}_{-1.0}$	31.0/14
UMi	$16.3^{+2.6}_{-2.1}$	$1.62^{+1.01}_{-0.47}$	$15.3^{+8.6}_{-3.9}$	682.5/461
Wil1	290^{+440}_{-230}	$0.070^{+2.770}_{-0.038}$	$1.35^{+26.35}_{-0.48}$	52.5/38

Conde 2024). When integrating all of the subhalo contributions, one gets a boost factor $\mathcal{B}$ on the astrophysical factor such as:

$$J'(<\alpha) = [1 + \mathcal{B}(<\alpha)]\, J(<\alpha)\,, \tag{A4}$$

where J' is the astrophysical factor integrated over a certain aperture angle α, taking into account both the subhalo mass distribution and the concentration-to-mass relation. The net signal enhancement produced by substructures can thus be factorized with $\mathcal{B}$, as shown in equation (A4).

In the annihilation case, $\mathcal{B}$ is relevant for large and massive objects, such as galaxy clusters, and less relevant for the dSphs. This is also due to the fact that dSphs are affected by tidal stripping on their outer rims, which truncates the dSph DM density profile at large radii removing in this way a significant amount of substructures that are mainly located in these regions (Á. Moliné et al. 2017). Depending on the dSph, the boost factor can be of the order of at most $\mathcal{B} \sim 0.3$ (see e.g. fig. 7 of Á. Moliné et al. 2017); for this reason, we decide to arbitrarily set $\mathcal{B} = 0$ for our discussion. This choice is further motivated by the intrinsic uncertainties on $J_{\rm ann}$ (or $J_{\rm dec}$) of the main halo that dominate over this factor; in addition, since the value of $\mathcal{B}$ linearly affects our results, it is easily modifiable for future analyses with different assumptions on the boost factor. Finally, for the case of decaying DM, the boost factor is even more negligible, because $J_{\rm dec}$ integrates the linear DM density (see equation 3).

A2.7 Astrophysical factors

We finally computed the profiles of $J_{\rm ann}(<\alpha_{\rm int})$ and $J_{\rm dec}(<\alpha_{\rm int})$ as functions of the integration angle $\alpha_{\rm int}$ from the dSph centre by running the CLUMPY executable over the posterior distributions of the DM profile parameters. From such profiles, we extracted the full radial dependence of $J_{\rm ann}$ and $J_{\rm dec}$, as well as their values at the typical reference values of $\alpha_{\rm int} = 0.1^\circ$ – close to the average CTAO angular resolution (see Table 1) – and 0.5°.

A3 Comparison with the results from the literature

In general, the determination of astrophysical factors for dSph haloes is affected by several uncertainties and systematics. If not recognized and appropriately removed or mitigated, such spurious contributions may significantly alter the analysis of the dSph stellar kinematics, leading to a wrong estimate of the DM content. The major sources of uncertainties and systematics affecting $J_{\rm ann}$ and $J_{\rm dec}$ values are:

Table A5. Astrophysical factors for DM annihilation and decay of the 14 dSphs remaining after the second selection criterion, integrated up to 0.1° and 0.5° for both the Einasto and Burkert DM density profiles (see the text for details), along with the corresponding uncertainties at 68 per cent CL. For profiles yielding unconstrained values, ULs are given at a 95 per cent CL. In the table, all the astrophysical factors for DM annihilation ($J_{\rm ann}$) in logarithmic GeV^2 cm^{-5} and all those for DM decay ($J_{\rm dec}$) in logarithmic GeV cm^{-2}.

	Einasto				Burkert			
Name	log $J_{\rm ann}$ ($<0.1°$)	log $J_{\rm ann}$ ($<0.5°$)	log $J_{\rm dec}$ ($<0.1°$)	log $J_{\rm dec}$ ($<0.5°$)	log $J_{\rm ann}$ ($<0.1°$)	log $J_{\rm ann}$ ($<0.5°$)	log $J_{\rm dec}$ ($<0.1°$)	log $J_{\rm dec}$ ($<0.5°$)
BoöI	$17.8^{+0.4}_{-0.3}$	$18.5^{+0.7}_{-0.5}$	$17.2^{+0.4}_{-0.2}$	$18.4^{+0.6}_{-0.4}$	$18.0^{+0.6}_{-0.6}$	$19.3^{+0.7}_{-0.6}$	$17.6^{+0.5}_{-0.4}$	$19.0^{+0.6}_{-0.5}$
CBe	$18.7^{+0.4}_{-0.5}$	$19.6^{+0.8}_{-0.7}$	$17.6^{+0.6}_{-0.3}$	$18.9^{+0.8}_{-0.5}$	$18.9^{+0.8}_{-0.4}$	$20.3^{+0.8}_{-1.1}$	$18.2^{+0.5}_{-0.8}$	$19.6^{+0.5}_{-1.1}$
DraI	$18.3^{+0.3}_{-0.2}$	$18.7^{+0.1}_{-0.1}$	$17.3^{+0.1}_{-0.1}$	$18.3^{+0.1}_{-0.1}$	$18.1^{+0.2}_{-0.2}$	$18.7^{+0.1}_{-0.1}$	$17.3^{+0.1}_{-0.1}$	$18.3^{+0.1}_{-0.1}$
GruII	$14.9^{+1.0}_{-1.3}$	$15.5^{+1.1}_{-2.0}$	$15.5^{+0.7}_{-1.8}$	$16.2^{+1.2}_{-3.1}$	$\lesssim 15.6$	$\lesssim 18.0$	$\lesssim 16.3$	$\lesssim 18.0$
RetII	$18.3^{+0.3}_{-0.3}$	$19.0^{+0.8}_{-0.5}$	$17.3^{+0.4}_{-0.3}$	$18.5^{+0.6}_{-0.7}$	$18.6^{+0.2}_{-0.7}$	$20.1^{+0.1}_{-1.5}$	$18.2^{+0.1}_{-1.1}$	$18.9^{+0.7}_{-1.2}$
Scl	$18.2^{+0.3}_{-0.2}$	$18.4^{+0.2}_{-0.1}$	$17.2^{+0.1}_{-0.1}$	$17.9^{+0.1}_{-0.1}$	$17.9^{+0.1}_{-0.1}$	$18.3^{+0.1}_{-0.1}$	$17.2^{+0.1}_{-0.1}$	$18.0^{+0.1}_{-0.1}$
Seg1	$16.2^{+1.7}_{-2.4}$	$16.9^{+1.6}_{-3.4}$	$16.2^{+1.2}_{-1.0}$	$17.3^{+1.5}_{-1.8}$	$\lesssim 18.0$	$\lesssim 21.1$	$\lesssim 17.5$	$\lesssim 21.1$
Sex	$17.3^{+0.6}_{-0.8}$	$18.0^{+0.3}_{-0.3}$	$17.1^{+0.1}_{-0.1}$	$18.3^{+0.1}_{-0.1}$	$16.6^{+0.3}_{-0.1}$	$17.9^{+0.1}_{-0.1}$	$17.0^{+0.1}_{-0.1}$	$18.3^{+0.1}_{-0.1}$
‡SgrI	$18.2^{+1.0}_{-2.1}$	$18.9^{+0.7}_{-1.4}$	$17.1^{+0.3}_{-0.7}$	$18.3^{+0.3}_{-0.6}$	$\lesssim 16.2$	$\lesssim 18.0$	$\lesssim 16.5$	$\lesssim 18.0$
SgrII	$18.6^{+1.0}_{-0.8}$	$18.9^{+1.7}_{-1.0}$	$17.4^{+0.8}_{-0.7}$	$18.3^{+1.1}_{-1.1}$	$19.2^{+0.9}_{-0.6}$	$19.6^{+1.7}_{-1.1}$	$17.8^{+0.8}_{-0.6}$	$18.7^{+1.3}_{-1.1}$
TriII	$16.0^{+2.2}_{-3.7}$	$16.6^{+2.4}_{-4.5}$	$16.1^{+1.3}_{-2.7}$	$16.9^{+1.6}_{-3.9}$	$\lesssim 18.6$	$\lesssim 21.6$	$\lesssim 17.8$	$\lesssim 21.6$
†UMaII	$18.1^{+0.7}_{-0.7}$	$18.9^{+0.5}_{-0.4}$	$17.3^{+0.3}_{-0.2}$	$18.4^{+0.3}_{-0.3}$	$17.8^{+1.2}_{-0.8}$	$18.9^{+0.5}_{-0.6}$	$17.3^{+0.2}_{-0.3}$	$18.4^{+0.4}_{-0.4}$
UMi	$18.2^{+0.1}_{-0.1}$	$19.3^{+0.2}_{-0.2}$	$17.6^{+0.1}_{-0.1}$	$18.9^{+0.2}_{-0.1}$	$18.2^{+0.1}_{-0.1}$	$19.4^{+0.2}_{-0.1}$	$17.7^{+0.2}_{-0.1}$	$19.0^{+0.2}_{-0.1}$
†Wil1	$18.9^{+0.4}_{-0.4}$	$19.2^{+0.7}_{-0.5}$	$17.3^{+0.4}_{-0.3}$	$18.0^{+1.0}_{-0.5}$	$19.0^{+0.7}_{-0.4}$	$19.3^{+1.5}_{-0.6}$	$17.4^{+1.0}_{-0.3}$	$18.1^{+1.7}_{-0.5}$

Notes. †Kinematically altered targets. ‡Kinematically altered targets with non-negligible γ-ray background emission.

Table A6. Ranking of the optimal dSphs, based on their relative values of $J_{\rm ann}$ (Einasto profile) integrated up to the reported angular sizes. The angle $\alpha_{\rm tid} = \arctan(R_{\rm tid}/{\rm d}_\odot)$ corresponds to the projection of the tidal radius $R_{\rm tid}$ (see Table 3) at the dSph distance $\rm d_\odot$. Our final ranking is the one reported in the 0.1° column.

Name	0.1°	0.5°	1°	$\alpha_{\rm tid}$
BooI	10th	8th	8th	8th
CBe	2nd	1st	1st	2nd
DraI	4th	7th	9th	10th
RetII	5th	4th	4th	3rd
Scl	6th	10th	10th	11th
Sex	11th	11th	11th	9th
SgrI	9th	9th	7th	7th
SgrII	3rd	5th	6th	6th
UMaII	8th	6th	5th	5th
UMi	7th	2nd	2nd	1st
Wil1	1st	3rd	3rd	4th

(i) *Difficulty/impossibility to obtain tangential components of the member star velocities*. The possibility to neglect the rotational support in dSph dynamics, quantified by the dispersion of stellar proper motions, is key to considering such objects as DM dominated; in fact, the presence of a non-negligible stellar-velocity tangential component may significantly alter the distribution of measured radial velocities, thus artificially increasing an intrinsically low DM amount. However, since the typical proper motion of a dSph is roughly of $0.2-0.5$ mas yr^{-1} and the inner radial velocity dispersion is of the order of 10 km s^{-1}, the proper-motion dispersion of the dSph member stars is of the order of 0.01 mas yr^{-1}; for bright stars ($G<15$), this amount is already at the limit of current and future stellar surveys, such as the *Gaia* second (DR2; Gaia Collaboration 2018, 2020a, b) and early third data release[43] (EDR3).

[43]See https://www.cosmos.esa.int/web/gaia/earlydr3.

(ii) *Stellar velocity dispersion dominated by tidal forces*. Another source of alteration of the dSph stellar velocity dispersion comes from the risk that the analysed dwarf galaxy does not reside inside a gravitationally undisturbed DM minihalo of primordial origin, but is rather a remnant of a bigger object that has been tidally disrupted by close encounters with the MW. In the first case, the measured radial velocity dispersion σ_r is (J. Binney & S. Tremaine 2008):

$$\sigma_r^{\rm (DM)} = \sqrt{\frac{G M_{\rm DM}}{3 R_{\rm tid}}}\,, \tag{A5}$$

whereas in the second case one gets:

$$\sigma_r^{\rm (tid)} = \sqrt{\frac{2 G M_{\rm MW} R_{\rm tid}}{3 d_{\rm GC}^2}}\,. \tag{A6}$$

It is therefore clear that, lacking hints of ongoing tidal interaction in the target, a large σ_r can potentially lead to its wrong attribution to an extreme DM domination; a clear example is offered by the SgrI dSph, which exhibits a rather large – although uncertain – value of $J_{\rm ann}$ (but see T. A. A. Venville et al. 2024). The current deep stellar surveys may help to identify tidally disrupted sources by detecting the stellar streams produced by the gravitational encounters of the dSph with the MW (e.g. A. Drlica-Wagner et al. 2015b; B. Mutlu-Pakdil et al. 2018), thus allowing the re-analysis (or exclusion) of targets located within such features; this might likely be the case of SgrII, which presumably lies inside the trailing arm of the Sagittarius stream (B. P. M. Laevens et al. 2015b).

(iii) *Contamination of member samples by foreground stars*. Since the dSphs are often viewed in projection only, with no or very few hints about surrounding stellar structures, foreground population of stars with age and metallicity that balance the distance difference with respect to the dSph cannot be distinguished through photometric measurements. Therefore, the measurement of spectroscopic velocities is crucial in order to fully disentangle the dSph stellar population by foreground contamination. The erroneous inclusion

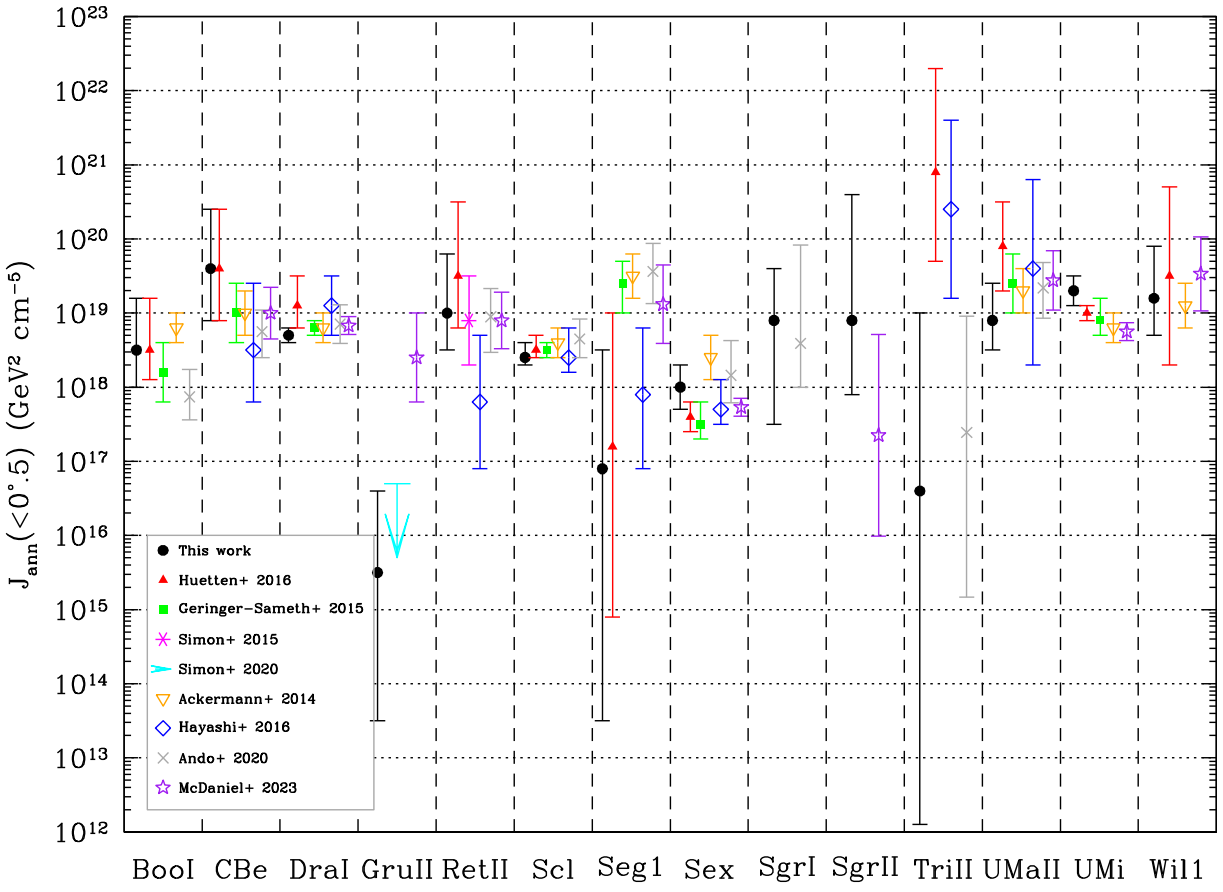

Figure A2. Same as in Fig. 6, but within 0.5° of integration (see the legend M. Ackermann et al. 2014; A. Geringer-Sameth et al. 2015; J. D. Simon et al. 2015, 2020; K. Hayashi et al. 2016; M. Hütten et al. 2016; S. Ando et al. 2020; A. McDaniel et al. 2024).

of such spurious populations may deeply alter the calculation of correct dSph astrophysical factors: this is the case of Seg1, which had a $J_{ann} \gtrsim 10^{19}$ GeV^2 cm^{-5} (e.g. M. Ackermann et al. 2014; A. Geringer-Sameth et al. 2015) until the discovery by J. D. Simon et al. (2011) of high-velocity foreground stars ($v \sim 300$ km s^{-1}) superimposed on the dSph structure, which led V. Bonnivard et al. (2015a, 2016b) to the revision of its DM content ($J_{ann} \ll 10^{18}$ GeV^2 cm^{-5}).

(iv) *Missing consideration of the dSph triaxiality*. Undisturbed dSphs are often treated as if they possessed a quasi-spheroidal symmetry, which allows the application of the spherical Jeans analysis with a negligible approximation on the real dSph geometry. However, such an assumption is in contrast with both (i) the observed non-spherical distribution of luminous matter in both classical and ultrafaint dSphs (M. Irwin & D. Hatzidimitriou 1995; A. W. McConnachie 2012), and (ii) the prediction of non-spherical DM haloes in Λ-CDM models of structure formation (K. Hayashi et al. 2016). Axisymmetric studies of the mass distribution in dSphs actually predict triaxial dark haloes (K. Hayashi & M. Chiba 2012, 2015); based on this evidence, K. Hayashi et al. (2016) adopted such models to derive the values of J_{ann} and J_{dec} for dSphs. They found that the median values of such quantities computed in this way are in general lower than those obtained with the assumption of spherical haloes, and with larger error bars; an increase of ∼0.4 dex in the uncertainties at 68 per cent probability is also evidenced by V. Bonnivard et al. (2015b) when taking into account the DM halo triaxiality.

Considering such potential issues, we check the consistency of our set of astrophysical factors for the selected optimal dSphs by comparing them to the values available in the literature for both $\alpha_{int} = 0.1°$ and 0.5°. To this aim, we collect all the relevant estimates of J_{ann} at such integration angles obtained from the analysis of the dSph kinematics (M. Ackermann et al. 2014; V. Bonnivard et al. 2015b, c; A. Geringer-Sameth et al. 2015; J. D. Simon et al. 2015, 2020; A. Genina & M. Fairbairn 2016; K. Hayashi et al. 2016; S. Ando et al. 2020). For sources lacking an estimate of $J_{ann}(< 0.1°)$ but having values of J_{ann} derived at larger integration angles (e.g. 0.2° or 0.5°), such as GruII (J. D. Simon et al. 2020) and RetII (J. D. Simon et al. 2015), we extrapolate them to $\alpha_{int} = 0.1°$ based on such values. We show the comparison between our values of $J_{ann}(< 0.1°)$ and those from the literature in Fig. 6, as well as between our $J_{ann}(< 0.5°)$ estimates and the literature in Fig. A2. Such plots reveals that, prior to the analysis by V. Bonnivard et al. (2015c), the astrophysical factor of Seg1 was overestimated by a factor of >100 due to the inclusion in its member sample of the spurious stellar population with $\langle v_r \rangle \sim 300$ km s^{-1} (see Fig. A1). An even more severe overestimation by >4 orders of magnitude was made for TriII due to poorly determined kinematics of its member stars (E. N. Kirby et al. 2017). The need for selecting clean kinematic samples in gravitationally undisturbed objects to obtain a reliable measurement of the DM amount in a dSph halo is again well exemplified by the case of SgrI, which would be classified as a DM-dominated source ($J_{ann} \gtrsim 10^{18}$ GeV^2 cm^{-5}) if the gravitational disturbance due to its proximity to the dense Galactic bulge were not known.

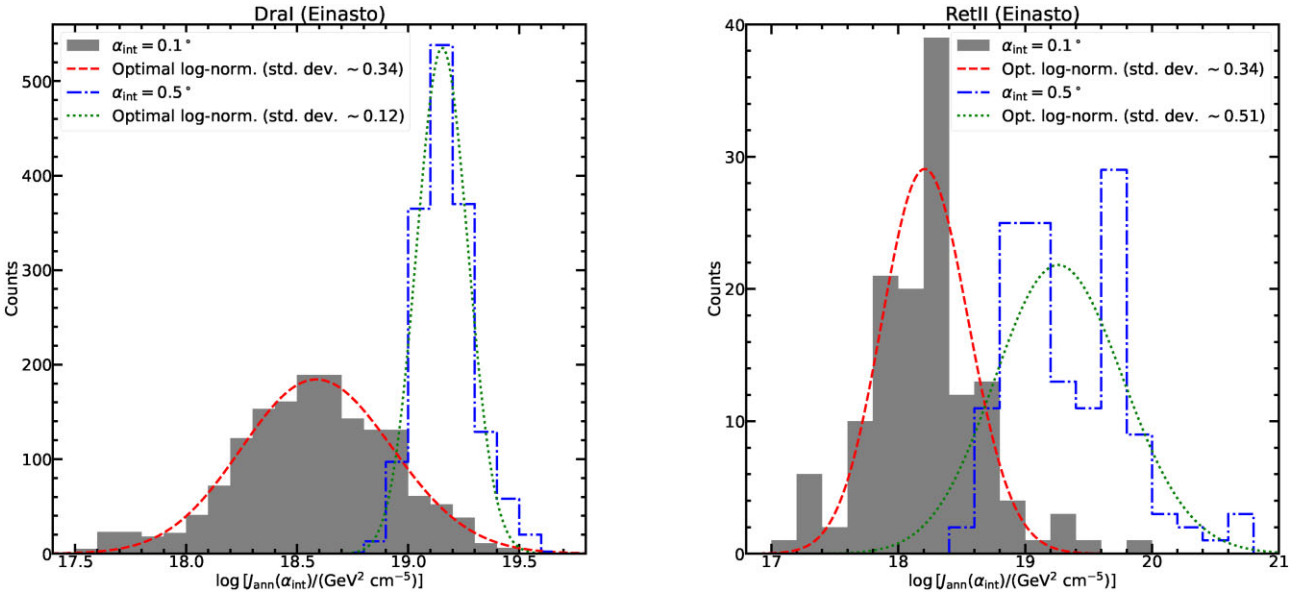

Figure A3. Examples of posterior distributions for the annihilation astrophysical factors of DraI (left panel) and RetII (right panel) using the Einasto DM density profile. In both panels, histograms are computed at integration angles of 0.1° and 0.5°. The optimal lognormal curves are shown superimposed to the relative histogram, along with the corresponding standard deviations (see the legend).

A4 Ranking for source extension

As a final consistency check on our dSph selection, we report in Table A6, the positional ranking of every source of interest, based on their relative J_{ann} within a specified integration angle. As can be inferred by this table, once excluding SgrI due to its well-known altered dynamical status (see Appendix A3), the only target that significantly challenges our selection of optimal sources is BooI; such an object has in fact a larger J_{ann} with respect to Scl for integration angles up to 0.5°, and also with respect to DraI when integrating up to 1°. However, this does not happen at the prioritized integration angle of 0.1°, and only affects the bottom of our ranking – with the position of the best six sources (CBe, RetII, SgrII, UMaII, UMi, and Wil1) not being significantly altered. Since the first ranked objects at any integration angle will likely be the only ones observed by CTAO during the first part of its scientific operations, we leave unaltered our selection of optimal targets presented above.

APPENDIX B: STUDIES ON SOURCES OF SYSTEMATIC UNCERTAINTIES

In this appendix, we evaluate the impact of some analysis choices on our results. In detail, in Appendix B3, we discuss the effect of the dSph extension; in Appendix B4, we compare the results obtained with different apertures of the integration region; in Appendix B5, we describe the performance of the ON/OFF method, in comparison with the template-background one; in Appendix B6, we discuss the effect of IRF systematics; and finally, in Appendix B7, we compare our results with those obtained with other publicly available tools like CTOOLS and SWORDFISH.

B1 Statistical uncertainties on the astrophysical factor

Our calculation of the astrophysical factors with the CLUMPY software (see Section 2) allows us to compute the posterior distributions of the values of J_{ann} and J_{dec} at arbitrary values of the integration angle α_{int} (see Appendix A). However, as shown in Figs 4 and 5 and described in Appendix A, such an analysis results in relevant uncertainties affecting the values of J_{ann} and J_{dec}, especially at large integration angles. An accurate estimate of such systematics is influenced by several factors, mostly related to the quality of the photometric and spectroscopic data available for each target, as well as the working hypothesis on the DM distribution around the source (anisotropy, triaxiality, etc., as discussed in Appendix A).

As an example, in Fig. A3, we report the histograms of such posterior distributions for the DraI and RetII DM haloes – modelled with the Einasto DM density profile – at two different integration angles (0.1° and 0.5°). We note that the distributions appear log-normal, with extended tails towards both small and large values of the astrophysical factor. In addition, the general dependence of such distributions on the integration angle is opposite for classical (with large stellar statistics) and ultrafaint dSphs (with $\lesssim$50 member stars), with the former tending to narrow around a saturation value of the astrophysical factor for increasing α_{int} and the latter becoming more spread out at large integration angles. Therefore, we conclude that there is no unique reference for a statistical distribution of the uncertainties on the astrophysical factors, making their inclusion in equation (10) non-trivial.

In this work, in line with what is done in CTAO Consortium (2024a), we use a lognormal distribution as our benchmark for the statistical uncertainties on the astrophysical factors, with a width equal to the average of the upper and lower 1σ uncertainties computed at an integration angle of 0.5° (see Fig. A3). We use the distributions parametrized in this way for each dSph in equation (10); a full treatment of these uncertainties in a 2D approach could be explored in a future publication.

B2 Effect of tidal stripping on the DM density profile

We have detailed in Appendix A3 how tidal forces can dominate the stellar velocity dispersions in dSphs. Even in case of DM-dominated sources as those analysed in this paper, tidal interactions can still strip their outer envelope of the more loosely bound DM particles,

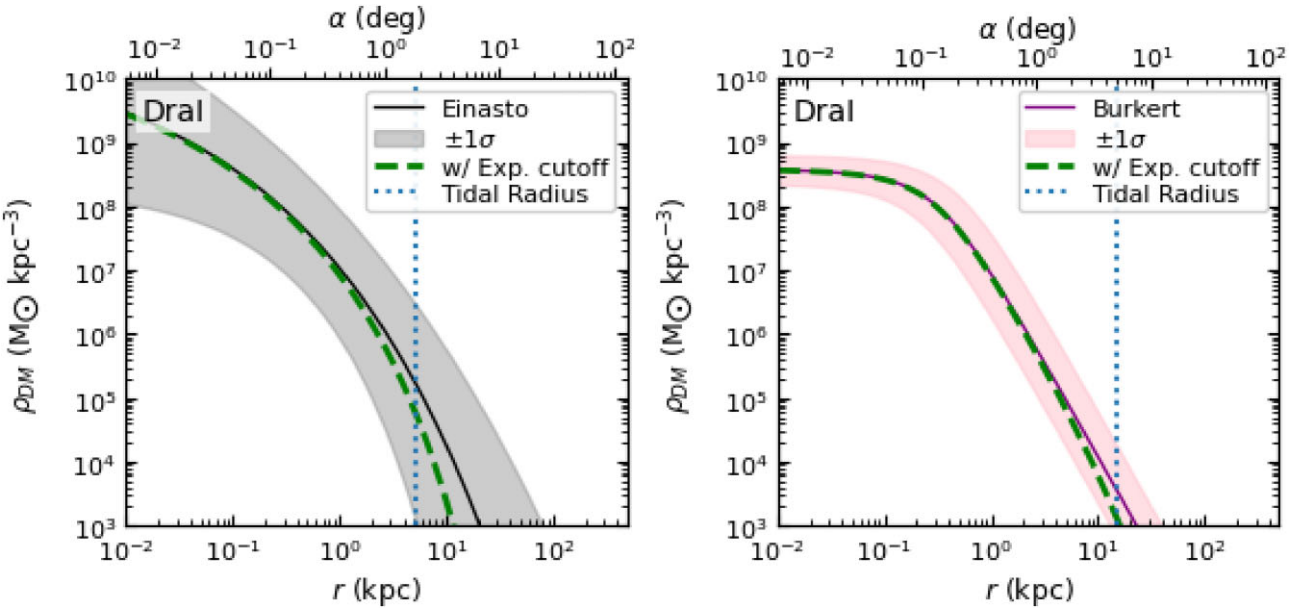

Figure B1. Impact of the exponential cut-off produced by tidal interactions on the DM density profiles for the representative case of DraI. In both panels, the median profiles modified by the functional form presented in equation (B1) (R. Errani & J. F. Navarro 2021) are shown superimposed to the clumpy best-fitting median profiles along with the corresponding uncertainties at 68 per cent CL. The respective tidal radii are also indicated.

leading to cut-off DM density profiles with respect to the theoretical expectations (E. Hayashi et al. 2004; S. Kazantzidis et al. 2004; J. Peñarrubia et al. 2010). We already account for a degree of tidal stripping in the dSph haloes by stopping the integration of $J_{\rm ann}$ and $J_{\rm dec}$ at the tidal angle $\alpha_{\rm tid}$ (see Section 2.2 and Appendix A4); here, we instead evaluate potential biases introduced with this technique with respect to a proper modelling of stripped halo profiles. Following R. Errani & J. F. Navarro (2021), we thus multiply the DM density profiles $\rho_{\rm Ein/Bur}(r)$ presented in equation (6) by an exponential cut-off:

$$\rho_{\rm DM}(r) = \rho_{\rm Ein/Bur}(r) \times \frac{e^{-r/R_{\rm tid}}}{(1 + r_{\rm s}/R_{\rm tid})^{0.3}}, \tag{B1}$$

with $r_{\rm s}$ and $R_{\rm tid}$ selected according to the accounted profile. We show the impact of such a cut-off on the DM density profiles in Fig. B1 for the representative case of DraI.

We then compare the integrals of $J_{\rm ann}$ truncated to $R_{\rm tid}$ with no exponential cut-off to the values obtained by integrating the entire DM density profiles defined in equation (B1): we find that the latter are systematically lower than the former by $\sim$0.2 dex on average for the Einasto shape, and by $\sim$0.1 dex for the Burkert functional form. Lower astrophysical factors clearly affect the expected γ-ray signal, thus worsening the detection prospects; however, we note that a (systematic) $\lesssim$0.2-dex change in the value of $J_{\rm ann}$ or $J_{\rm dec}$ produces an effect that falls at most within the (statistical) 2σ uncertainty of the limits on the DM parameters presented in Figs 8–10. In addition, the magnitude of the signal loss becomes significant only when integrating up to large angular regions that approach $\alpha_{\rm tid}$. We therefore conclude that the impact of tidally induced cut-offs on the $J_{\rm ann}$ and $J_{\rm dec}$ values may be mitigated by adopting appropriate observing strategies – e.g. focusing on the innermost regions of the dSph haloes or dividing the FoV into adequately defined RoIs (see Section 3.1).

B3 Source extension

A target is considered extended if its size is larger than the telescope angular resolution. This quantity is approximately defined as the standard deviation of the telescope PSF, i.e. the distribution of photons in the focal plane from a perfectly par-axial beam. The PSF is normally modelled as a double Gaussian.[44] If the angular distribution of the detected events coincides with the PSF, and thus no extension can be determined, the target is considered to be point-like; in this condition, the ON/OFF analysis (see Appendix B5) is the most accurate. Conversely, the template method is better suited for an extended source.

In general, the telescope acceptance changes as a function of the source position in the FoV – the farther from the telescope optical axis, the worse the acceptance. Therefore, for the analysis of an extended source one has to convolve the signal with the corresponding acceptance, which normally possesses circular symmetry; in this way, 'acceptance' rings can be defined. In the case of an unknown source extension, the search for signals depends on the definition of the RoI in the ON/OFF method. The optimal dSphs selected in this work are all mildly extended, as shown in Table 4 (see also Figs 4 and 5). Our results indicate that, together with some very compact objects like DraI for the DM annihilation scenario and Scl for the DM decay one, there are significantly extended targets such as UMi and CBe, confirming the advantage of a template background analysis for all of the selected sources.

B4 Impact of the aperture of the acceptance region

In Appendix B5, we mentioned the use of a FoV of 2×2 deg^2 for the computation of event counts; to evaluate the impact that different choices of the FoV extensions have on our results, we

[44] P. Da Vela et al. (2018) demonstrated that a more accurate modelling of the PSF is through a King function, but this is not relevant for the purpose of this work.

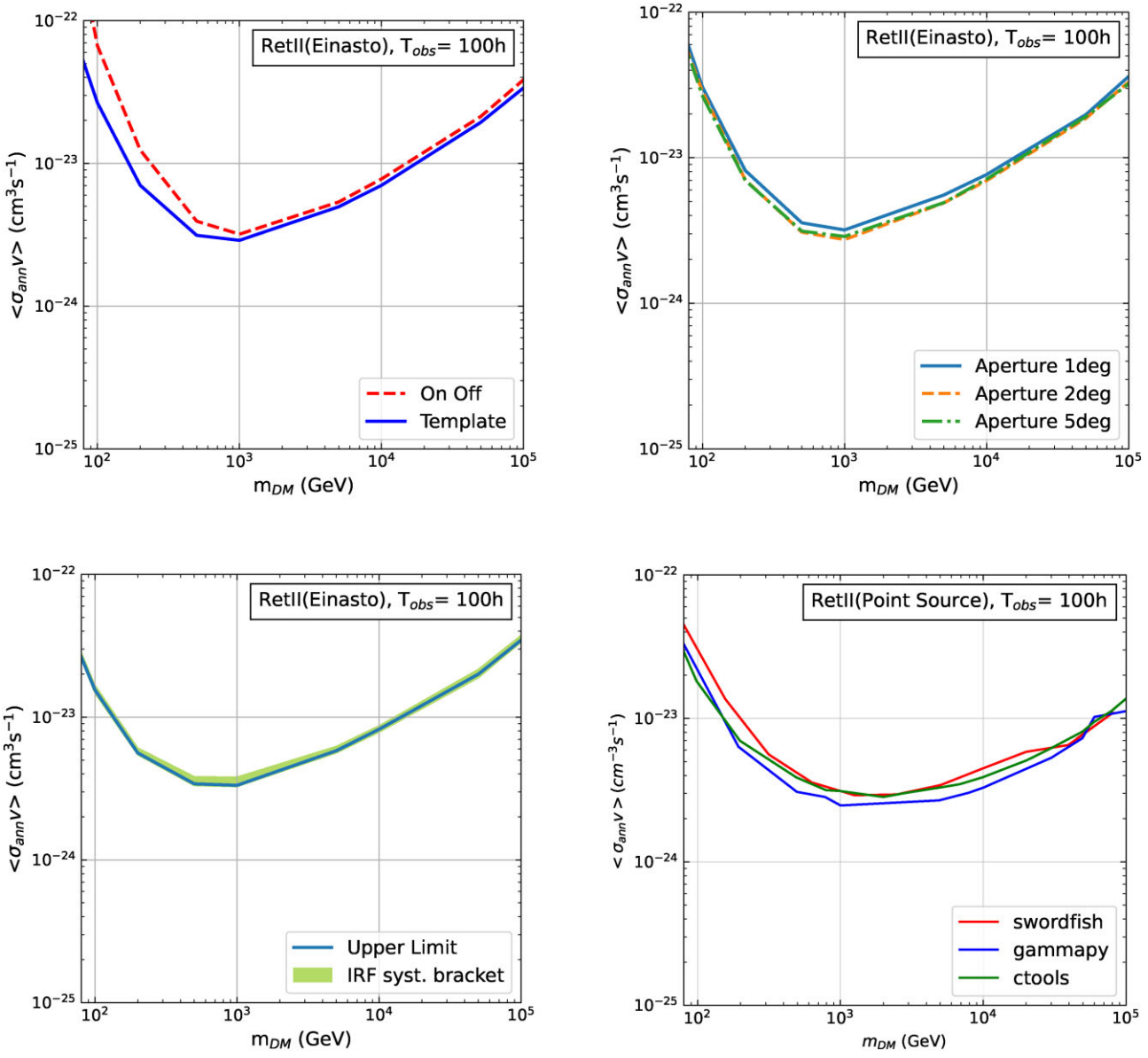

Figure B2. Checks on systematic uncertainties potentially affecting the derivation of particle DM parameters. Top-left panel: comparison of the cross-section limits obtained using a template-based method and an ON/OFF analysis. Top-right panel: comparison of the limits for different FoV sizes – 1×1 deg^2, 2×2 deg^2, and 5×5 deg^2. Bottom-left panel: limits derived taking into account the IRF systematics. Bottom-right panel: comparison of limits computed with different codes for Cherenkov γ-ray analysis – GAMMAPY, CTOOLS, and SWORDFISH. In all panels, the ULs are computed assuming 100-h observations of the RetII dSph (Einasto astrophysical factor) for DM annihilating in the $b\bar{b}$ channel.

produce likewise analyses on sky regions of 1×1 and 5×5 deg^2, respectively. In Fig. B2 (top right), we present the comparison between such choices; one can see that different FoV sizes have no or negligible effect on the derivation of the DM limits. Therefore, we conclude that the choice of a different aperture size with respect to our benchmark does not significantly impact our results.

B5 Comparison of ON/OFF and template analysis

In Section 3, we stated our choice to use the so-called template background method for our analysis. Within this framework, the background counts are estimated through a model over the entire FoV. This model is currently generated through the analysis of MC simulations reproducing the expected behaviour of the CTAO arrays, and cannot be validated before actual data from the instruments will be available. The alternative method for the background estimate is the commonly used ON/OFF method, in which background counts in an ON region – i.e. the region containing the source emitting γ-rays – are computed from a separate (OFF) background control region where no signal is expected. Normally, several OFF regions are identified in the FoV to increase the precision of the background intensity and shape measurements.

Since the background is measured rather than modelled, this technique has the advantage of being more accurate than the template

method; however, it starts to be difficult to apply when the source is moderately to strongly spatially extended. The dSphs with moderate extension are borderline, and thus an ON/OFF analysis is still possible for such targets; therefore, we tested the two methods on the sample dSph RetII. In Fig. B2 (top left), we compare the template and ON/OFF analyses of 100-h observations of a DM Einasto distribution in the RetII halo, assuming WIMPs of $m_{\rm DM} = 2.5$ TeV annihilating into the $b\bar{b}$ channel. The template analysis is computed over an aperture of 2×2 deg^2, whereas the ON/OFF analysis is computed over 5 background control regions of 0.11° each.

One can see that the two methods agree well between 300 GeV and 2 TeV, i.e. in the region with the largest expected instrumental sensitivity; the template method is better performing over the ON/OFF analysis below 300 GeV and above 2 TeV. Such a behaviour is expected, since at low energies, the amount of residual background is large and the background classification is more complex – thus allowing the background model to improve the accuracy and precision of the analysis, and ultimately the sensitivity – and at high energies, the statistic of events is lower – thus a more precise background estimate produces a higher signal-to-noise ratio. The actual difference in performance between the two analysis methods will be possible to be accurately evaluated only when real CTAO data will be collected, but we conclude that the choice of one analysis procedure over the other does not greatly impact our main results.

B6 Systematics on the instrument response functions

An accurate reconstruction of signal and background counts would require the use of IRFs for the specific sky direction and atmospheric conditions, that are not available at the moment. For this reason, we do not directly include the systematic uncertainties of the IRFs into the likelihood formalism (see equation 8); instead, we evaluate their impact by bracketing IRFs. This approach follows the procedure developed by the *Fermi*-LAT Collaboration (M. Ackermann et al. 2012). We have biased the energy reconstruction by 6 per cent, the effective area by 5 per cent, and the background rate by 0.8 per cent, corresponding to $\pm 1\sigma$ estimates matching the projected systematic uncertainties for CTA. Although potentially inaccurate, such an approximation allows us to bracket the maximum systematic uncertainties in this pre-operation prediction. We present the results in the bottom-left panel of Fig. B2, evidencing how systematic errors from IRFs are well below the Poisson statistic fluctuations.

In addition, regarding the background counts, we estimate that they can be determined with systematics below 1 per cent (CTAO Consortium 2021a), therefore becoming potentially relevant for observations longer than 100 h. This term should also be included in equation (8); however, considering that it is subdominant with respect to other instrumental systematics uncertainties discussed here and the uncertainties on the astrophysical factors, we neglect it for the purposes of this work.

B7 Comparison of results obtained with other codes

Finally, we compare in Fig. B2 (bottom right), the DM limits obtained with GAMMAPY (F. Acero et al. 2024), for the template method, with those obtained with the independent open-source analysis pipeline CTOOLS, based on the well-known *Fermi*-LAT tools and also valid to be used with CTAO data (J. Knödlseder et al. 2016). We also make predictions of the null hypothesis using the Asimov data set generated with the open-source SWORDFISH (T. D. P. Edwards & C. Weniger 2018; T. D. P. Edwards & C. Weniger 2017), used in other CTAO projects (CTAO Consortium 2021b). In the bottom-right panel of Fig. B2, we show how – also taking into account the uncertainty on the DM limits produced by the IRF systematics – the results obtained with such additional software are in very good agreement with those presented in this work.

[1]*Department of Physics, Tokai University, 4-1-1, Kita-Kaname, Hiratsuka, Kanagawa 259-1292, Japan*
[2]*Institute for Cosmic Ray Research, University of Tokyo, 5-1-5, Kashiwa-no-ha, Kashiwa, Chiba 277-8582, Japan*
[3]*Institute for Particle Physics and Astrophysics, ETH Zürich, Otto-Stern-Weg 5, CH-8093 Zürich, Switzerland*
[4]*INFN and Università degli Studi di Siena, Dipartimento di Scienze Fisiche, della Terra e dell'Ambiente (DSFTA), Sezione di Fisica, Via Roma 56, I-53100 Siena, Italy*
[5]*Université Paris-Saclay, Université Paris Cité, CEA, CNRS, AIM, F-91191 Gif-sur-Yvette Cedex, France*
[6]*FSLAC IRL 2009, CNRS/IAC, E-38205 La Laguna, Tenerife, Spain*
[7]*Department of Physics and Astronomy, University of Alabama, Tuscaloosa, Gallalee Hall, Box 870324, Tuscaloosa, AL 35487-0324, USA*
[8]*Université Côte d'Azur, Observatoire de la Côte d'Azur, CNRS, Laboratoire Lagrange, Bâtiment Fizeau, 28 Av. Valrose Parc Valrose, 06108, F-06000 Nice, France*
[9]*Laboratoire Leprince-Ringuet, CNRS/IN2P3, École Polytechnique, Institut Polytechnique de Paris, F-91120 Palaiseau, France*
[10]*Departament de Física Quàntica i Astrofísica, Institut de Ciències del Cosmos, Universitat de Barcelona, IEEC-UB, Martí i Franquès, 1, E-08028 Barcelona, Spain*
[11]*Instituto de Astrofísica de Andalucía – CSIC, Glorieta de la Astronomía s/n, E-18008 Granada, Spain*
[12]*Institute for Computational Cosmology and Department of Physics, Durham University, South Road, Durham DH1 3LE, UK*
[13]*Pontificia Universidad Católica de Chile, Av. Libertador Bernardo O'Higgins 340, CL-8331150 Santiago, Chile*
[14]*Universidad Nacional Autónoma de México, Delegación Coyoacán, 04510 Ciudad de México, Mexico*
[15]*Département de Physique Nucléaire et Corpusculaire, University de Genève, Faculté de Sciences, CH-1205 Genève, Switzerland*
[16]*Sorbonne Université, CNRS/IN2P3, Laboratoire de Physique Nucléaire et de Hautes Energies, LPNHE, 4 place Jussieu, F-75005 Paris, France*
[17]*LUX, Observatoire de Paris, Université PSL, Sorbonne Université, CNRS, 5 place Jules Janssen, F-2190 Meudon, France*
[18]*INAF – Osservatorio Astrofisico di Arcetri, Largo E. Fermi 5, I-50125 Firenze, Italy*
[19]*INFN Sezione di Perugia and Università degli Studi di Perugia, Via A. Pascoli, I-06123 Perugia, Italy*
[20]*INFN Sezione di Napoli, Via Cintia, ed. G, I-80126 Napoli, Italy*
[21]*Università degli Studi di Napoli 'Federico II' - Dipartimento di Fisica 'E. Pancini', Complesso Universitario di Monte Sant'Angelo, Via Cintia, I-80126 Napoli, Italy*
[22]*INAF – Osservatorio Astronomico di Roma, Via di Frascati 33, I-00078 Monteporzio Catone, Italy*
[23]*International Institute of Physics, Universidade Federal do Rio Grande do Norte, 59078-970 Natal, RN, Brasil*
[24]*Departamento de Física, Universidade Federal do Rio Grande do Norte, 59078-970 Natal, RN, Brasil*
[25]*INFN Sezione di Padova, Via Marzolo 8, 35131 Padova, Italy*
[26]*Instituto de Física Teórica UAM/CSIC and Departamento de Física Teórica, Universidad Autónoma de Madrid, c/ Nicolás Cabrera 13-15, Campus de Cantoblanco UAM, E-28049 Madrid, Spain*
[27]*Instituto de Física, Universidade de São Paulo, Rua do Matão Travessa R Nr.187, CEP 05508-090 Cidade Universitária, São Paulo, Brazil*
[28]*Department of Physics, Chemistry & Material Science, University of Namibia, Private Bag 13301, NA-10005 Windhoek, Namibia*
[29]*Centre for Space Research, North-West University, Potchefstroom 2520, South Africa*

[30]*School of Physics and Astronomy, Monash University, Melbourne, VIC 3800, Australia*
[31]*IPARCOS-UCM, Instituto de Física de Partículas y del Cosmos, and EMFTEL Department, Universidad Complutense de Madrid, E-28040 Madrid, Spain*
[32]*Faculty of Science and Technology, Universidad del Azuay, Av. 24 de Mayo 7-44, ECU-010204 Cuenca, Ecuador*
[33]*Faculty of Physics and Astronomy, Astronomical Institute (AIRUB), Ruhr University Bochum, Universitätsstraße 150, D-44801 Bochum, Germany*
[34]*Instituto de Astrofísica de Canarias and Departamento de Astrofísica, Universidad de La Laguna, C/ Via Lactea s/n, E-38205 La Laguna, Tenerife, Spain*
[35]*Università degli Studi di Trento, Via Calepina, 14, I-38122 Trento, Italy*
[36]*INFN Sezione di Bari and Università degli Studi di Bari, via Orabona 4, I-70124 Bari, Italy*
[37]*Friedrich-Alexander-Universität Erlangen-Nürnberg, Erlangen Centre for Astroparticle Physics, Nikolaus-Fiebiger-Str. 2, D-91058 Erlangen, Germany*
[38]*INFN Sezione di Padova and Università degli Studi di Padova, Via Marzolo 8, I-35131 Padova, Italy*
[39]*Institut für Physik & Astronomie, Universität Potsdam, Karl-Liebknecht-Strasse 24/25, D-14476 Potsdam, Germany*
[40]*University of the Witwatersrand, 1 Jan Smuts Avenue, Braamfontein, 2000 Johannesburg, South Africa*
[41]*Institut für Theoretische Physik, Lehrstuhl IV: Plasma-Astroteilchenphysik, Ruhr-Universität Bochum, Universitätsstraße 150, D-44801 Bochum, Germany*
[42]*Center for Astrophysics | Harvard & Smithsonian, 60 Garden St, Cambridge, MA 02138, USA*
[43]*Department of Physics, Humboldt University Berlin, Newtonstr. 15, D-12489 Berlin, Germany*
[44]*Deutsches Elektronen-Synchrotron, Platanenallee 6, D-15738 Zeuthen, Germany*
[45]*CIEMAT, Avda. Complutense 40, E-28040 Madrid, Spain*
[46]*Max-Planck-Institut für Physik, Boltzmannstr. 8, D-85748 Garching, Germany*
[47]*Pidstryhach Institute for Applied Problems in Mechanics and Mathematics, NASU, 3B Naukova Street, Lviv UA-79060, Ukraine*
[48]*Center for Astrophysics and Cosmology (CAC), University of Nova Gorica, SI-5270 Nova Gorica, Slovenia*
[49]*Université Savoie Mont Blanc, CNRS, Laboratoire d'Annecy de Physique des Particules – IN2P3, F-74000 Annecy, France*
[50]*ASI – Space Science Data Center, Via del Politecnico s.n.c., I-00133 Rome, Italy*
[51]*Politecnico di Bari, via Orabona 4, I-70124 Bari, Italy*
[52]*INFN Sezione di Bari, via Orabona 4, I-70126 Bari, Italy*
[53]*Institut de Fisica d'Altes Energies (IFAE), The Barcelona Institute of Science and Technology, Campus UAB, E-08193 Bellaterra (Barcelona), Spain*
[54]*FZU – Institute of Physics of the Czech Academy of Sciences, Na Slovance 1999/2, CZ-182 00 Praha 8, Czech Republic*
[55]*INAF – Osservatorio Astronomico di Brera, Via Brera 28, I-20121 Milano, Italy*
[56]*INFN Sezione di Pisa, Edificio C–Polo Fibonacci, Largo Bruno Pontecorvo 3, I-56127, Pisa*
[57]*University School for Advanced Studies IUSS Pavia, Palazzo del Broletto, Piazza della Vittoria 15, I-27100 Pavia, Italy*
[58]*Faculty of Electrical Engineering and Computing, University of Zagreb, Unska 3, 10000 Zagreb, Croatia*
[59]*Department of Physics, University of Oslo, Sem Saelandsvei 24 – PO Box 1048 Blindern, N-0316 Oslo, Norway*
[60]*INAF – Osservatorio di Astrofisica e Scienza dello spazio di Bologna, Via Piero Gobetti 93/3, I-40129 Bologna, Italy*
[61]*Dublin City University, Glasnevin, Dublin 9, Ireland*
[62]*Dublin Institute for Advanced Studies, 31 Fitzwilliam Place, Dublin 2, Ireland*
[63]*Lamarr Institute, TU Dortmund, Joseph-von-Fraunhofer-Str. 25, D-44227 Dortmund, Germany*
[64]*Armagh Observatory and Planetarium, College Hill, Armagh BT61 9DB, UK*
[65]*School of Physics, University of New South Wales, Sydney NSW 2052, Australia*
[66]*Cherenkov Telescope Array Observatory, Saupfercheckweg 1, D-69117 Heidelberg, Germany*
[67]*Unitat de Física de les Radiacions, Departament de Física, and CERES-IEEC, Universitat Autònoma de Barcelona, Edifici C3, Campus UAB, E-08193 Bellaterra, Spain*
[68]*Department of Physics, Faculty of Science, Kasetsart University, 50 Ngam Wong Wan Rd., Lat Yao, Chatuchak, Bangkok 10900, Thailand*
[69]*National Astronomical Research Institute of Thailand, 191 Huay Kaew Rd., Suthep, Muang, Chiang Mai 50200, Thailand*
[70]*INAF – Osservatorio Astronomico di Capodimonte, Via Salita Moiariello 16, I-80131 Napoli, Italy*
[71]*Universidade Cidade de São Paulo, Núcleo de Astrofísica, R. Galvão Bueno 868, Liberdade, São Paulo, SP 01506-000, Brazil*
[72]*Department of Physics, Sapienza, University of Roma, Piazzale A. Moro 5, I-00185 Roma, Italy*
[73]*INAF – Istituto di Astrofisica Spaziale e Fisica Cosmica di Milano, Via A. Corti 12, I-20133 Milano, Italy*
[74]*CCTVal, Universidad Técnica Federico Santa María, Avenida España 1680, CL-2340000 Valparaíso, Chile*
[75]*Aix Marseille Université, CNRS/IN2P3, CPPM, F-13284 Marseille, France*
[76]*Université Paris Cité, CNRS, Astroparticule et Cosmologie, F-75013 Paris, France*
[77]*Centre for Advanced Instrumentation, Department of Physics, Durham University, South Road, Durham DH1 3LE, UK*
[78]*Department of Physics and Astronomy, University of California, Los Angeles, CA 90095, USA*
[79]*INFN Sezione di Torino, Via P. Giuria 1, I-10125 Torino, Italy*
[80]*Dipartimento di Fisica, Università degli Studi di Torino, Via Pietro Giuria 1, I-10125 Torino, Italy*
[81]*Dipartimento di Fisica e Chimica 'E. Segrè', Università degli Studi di Palermo, Via Archirafi 36, I-90123 Palermo, Italy*
[82]*INFN Sezione di Catania, Via S. Sofia 64, I-95123 Catania, Italy*
[83]*Universidade Federal Do Paraná – Setor Palotina, Departamento de Engenharias e Exatas, Rua Pioneiro, 2153, Jardim Dallas, CEP: 85950-000 Palotina, Paraná, Brazil*
[84]*IRFU, CEA, Université Paris-Saclay, Bât 141, F-91191 Gif-sur-Yvette, France*
[85]*INAF – Osservatorio Astrofisico di Catania, Via S. Sofia, 78, I-95123 Catania, Italy*
[86]*Department of Physics, Clarendon Laboratory, University of Oxford, Parks Road, Oxford OX1 3PU, UK*
[87]*Universidad de Valparaíso, Blanco 951, CL-2340000 Valparaiso, Chile*
[88]*University of Wisconsin, Madison, 500 Lincoln Drive, Madison, WI 53706, USA*
[89]*INAF – Istituto di Radioastronomia, Via Gobetti 101, I-40129 Bologna, Italy*
[90]*INAF – Istituto Nazionale di Astrofisica, Viale del Parco Mellini 84, I-00136 Rome, Italy*
[91]*Instituto de Astronomia, Geofísica e Ciências Atmosféricas – Universidade de São Paulo, Cidade Universitária, R. do Matão, 1226, CEP 05508-090, São Paulo, SP, Brazil*
[92]*INFN Sezione di Trieste and Università degli Studi di Udine, Via delle Scienze 208, I-33100 Udine, Italy*
[93]*Instituto de Física de São Carlos, Universidade de São Paulo, Av. Trabalhador São-carlense, 400 – CEP 13566-590 São Carlos, SP, Brazil*
[94]*Universidad de Alcalá – Space & Astroparticle Group, Facultad de Ciencias, Campus Universitario Ctra. Madrid-Barcelona, Km. 33.600, E-28871 Alcalá de Henares (Madrid), Spain*
[95]*Max-Planck-Institut für Kernphysik, Saupfercheckweg 1, D-69117 Heidelberg, Germany*
[96]*Institut für Astronomie und Astrophysik, Universität Tübingen, Sand 1, D-72076 Tübingen, Germany*
[97]*Department of Physics and Technology, University of Bergen, Museplass 1, 5007 Bergen, Norway*

[98]*Department of Astronomy and Astrophysics, University of Chicago, 5640 S Ellis Ave, Chicago, IL 60637, USA*
[99]*Astroparticle Physics, Department of Physics, TU Dortmund University, Otto-Hahn-Str. 4a, D-44227 Dortmund, Germany*
[100]*Escuela de Ingeniería Eléctrica, Facultad de Ingeniería, Pontificia Universidad Católica de Valparaíso, Avenida Brasil 2147, Valparaíso, Chile*
[101]*Santa Cruz Institute for Particle Physics and Department of Physics, University of California, Santa Cruz, 1156 High Street, Santa Cruz, CA 95064, USA*
[102]*Escola de Artes, Ciências e Humanidades, Universidade de São Paulo, Rua Arlindo Bettio, CEP 03828-000, 1000 São Paulo, Brazil*
[103]*Astronomical Observatory of Taras Shevchenko National University of Kyiv, 3 Observatorna Street, Kyiv UA-04053, Ukraine*
[104]*Department of Physics and Astronomy, University of Utah, Salt Lake City, UT 84112-0830, USA*
[105]*Department of Physics and Astronomy, The University of Manitoba, Winnipeg, Manitoba R3T 2N2, Canada*
[106]*RIKEN, Institute of Physical and Chemical Research, 2-1 Hirosawa, Wako, Saitama 351-0198, Japan*
[107]*INFN Sezione di Roma La Sapienza, P.le Aldo Moro 2, I-00185 Roma, Italy*
[108]*Western Sydney University, Locked Bag 1797, Penrith, NSW 2751, Australia*
[109]*INAF – Istituto di Astrofisica e Planetologia Spaziali (IAPS), Via del Fosso del Cavaliere 100, I-00133 Roma, Italy*
[110]*Physics Program, Graduate School of Advanced Science and Engineering, Hiroshima University, 739-8526 Hiroshima, Japan*
[111]*Department of Physics, Nagoya University, Chikusa-ku, Nagoya 464-8602, Japan*
[112]*Department of Information Technology, Escuela Politécnica Superior, Universidad San Pablo-CEU, CEU Universities, Campus Montepríncipe, Boadilla del Monte, Madrid E-28668, Spain*
[113]*INFN Sezione di Roma Tor Vergata, Via della Ricerca Scientifica 1, I-00133 Rome, Italy*
[114]*Alikhanyan National Science Laboratory, Yerevan Physics Institute, 2 Alikhanyan Brothers St., 0036 Yerevan, Armenia*
[115]*Centro Brasileiro de Pesquisas Físicas, Rua Xavier Sigaud 150, RJ 22290-180 Rio de Janeiro, Brazil*
[116]*INAF – Osservatorio Astronomico di Palermo 'G.S. Vaiana', Piazza del Parlamento 1, I-90134 Palermo, Italy*
[117]*Universidad Andrés Bello, Av. Fernández Concha 700, CL-7580012 Las Condes, Santiago, Chile*
[118]*Núcleo de Astrofísica e Cosmologia (Cosmo-ufes) & Departamento de Física, Universidade Federal do Espírito Santo (UFES), Av. Fernando Ferrari, 514, 29065-910 Vitória-ES, Brazil*
[119]*Astrophysics Research Center of the Open University (ARCO), The Open University of Israel, PO Box 808, Ra'anana 4353701, Israel*
[120]*Department of Physics, The George Washington University, Washington, DC 20052, USA*
[121]*CTAO, Via Piero Gobetti 93/3, 40129 Bologna, Italy*
[122]*CTAO, Science Data Management Centre (SDMC), Platanenallee 6, D-15738 Zeuthen, Germany*
[123]*Institute of Space Sciences (ICE, CSIC), and Institut d'Estudis Espacials de Catalunya (IEEC), and Institució Catalana de Recerca I Estudis Avançats (ICREA), Campus UAB, Carrer de Can Magrans, s/n, E-08193 Cerdanyola del Vallés, Spain*
[124]*General Education Center, Yamanashi-Gakuin University, Kofu, Yamanashi 400-8575, Japan*
[125]*School of Physics, Chemistry and Earth Sciences, University of Adelaide, Adelaide SA 5005, Australia*
[126]*Sendai College, National Institute of Technology, 4-16-1 Ayashi-Chuo, Aoba-ku, Sendai City, Miyagi 989-3128, Japan*
[127]*Department of Physics, Faculty of Engineering Science, Yokohama National University, Yokohama 240–8501, Japan*
[128]*Faculty of Science, Joint Laboratory of Optics of Palacký University and Institute of Physics of the Czech Academy of Sciences, Palacký University Olomouc, 17. listopadu 1192/12, CZ-779 00 Olomouc, Czech Republic*
[129]*Josip Juraj Strossmayer University of Osijek, Trg Ljudevita Gaja 6, 31000 Osijek, Croatia*
[130]*CETEMPS Dipartimento di Scienze Fisiche e Chimiche, Università degli Studi dell'Aquila and GSGC-LNGS-INFN, Via Vetoio 1, L'Aquila I-67100, Italy*
[131]*Research Center for Advanced Particle Physics, Kyushu University, 744 Motooka, Nishi-ku, Fukuoka 819-0395, Japan*
[132]*Chiba University, 1-33, Yayoicho, Inage-ku, Chiba-shi, Chiba 263-8522, Japan*
[133]*Department of Earth and Space Science, Graduate School of Science, Osaka University, Toyonaka 560-0043, Japan*
[134]*Astronomical Observatory, Jagiellonian University, ul. Orla 171, PL-30-244 Cracow, Poland*
[135]*Landessternwarte, Zentrum für Astronomie der Universität Heidelberg, Königstuhl 12, D-69117 Heidelberg, Germany*
[136]*IRAP, Université de Toulouse, CNRS, CNES, UPS, 9 avenue Colonel Roche, F-31028 Toulouse, Cedex 4, France*
[137]*Astronomical Institute of the Czech Academy of Sciences, Bocni II, CZ-1401 - 14100 Prague, Czech Republic*
[138]*Faculty of Science and Engineering, Waseda University, Shinjuku, Tokyo 169-8555, Japan*
[139]*School of Physics, Aristotle University, Thessaloniki, 54124 Thessaloniki, Greece*
[140]*Universität Innsbruck, Institut für Astro- und Teilchenphysik, Technikerstr. 25/8, A-6020 Innsbruck, Austria*
[141]*Nicolaus Copernicus Astronomical Center, Polish Academy of Sciences, ul. Bartycka 18, PL-00-716 Warsaw, Poland*
[142]*National Astronomical Observatory of Japan (NAOJ), Division of Science, 2-21-1, Osawa, Mitaka, Tokyo 181-8588, Japan*
[143]*Institute of Particle and Nuclear Studies, KEK (High Energy Accelerator Research Organization), 1-1 Oho, Tsukuba 305-0801, Japan*
[144]*INAF – Istituto di Astrofisica Spaziale e Fisica Cosmica di Palermo, Via U. La Malfa 153, I-90146 Palermo, Italy*
[145]*School of Physics and Astronomy, University of Leicester, Leicester LE1 7RH, UK*
[146]*Università degli Studi di Catania, Dipartimento di Fisica e Astronomia 'Ettore Majorana', Via S. Sofia 64, I-95123 Catania, Italy*
[147]*Anton Pannekoek Institute/GRAPPA, University of Amsterdam, Science Park, 904 NL-1098 XH Amsterdam, the Netherlands*
[148]*Department of Physics and Astronomy, University of Turku, Finland, FI-20014, Finland*
[149]*INFN Sezione di Trieste and Università degli Studi di Trieste, Via Valerio 2, I-34127 Trieste, Italy*
[150]*Escuela Politécnica Superior de Jaén, Universidad de Jaén, Campus Las Lagunillas s/n, Edif. A3, E-23071 Jaén, Spain*
[151]*Department of Astronomy, University of Geneva, Chemin d'Ecogia 16, CH-1290 Versoix, Switzerland*
[152]*Saha Institute of Nuclear Physics, A CI of Homi Bhabha National Institute, Kolkata 700064, West Bengal, India*
[153]*Department of Biology and Geology, Physics and Inorganic Chemistry, C/ Tulipán, s/n. 28933 Móstoles (Faculty of Experimental Sciences and Technology), Spain*
[154]*UCM-ELEC Group, EMFTEL Department, University Complutense of Madrid, 28040 Madrid, Spain*
[155]*Universidade Tecnológica Federal do Paraná, Av. Sete de Setembro, 3165 - Rebouças CEP 80230-901, Curitiba - PR, Brasil*
[156]*Macroarea di Scienze MMFFNN, Università di Roma Tor Vergata, Via della Ricerca Scientifica 1, I-00133 Rome, Italy*
[157]*Universität Hamburg, Institut für Experimentalphysik, Luruper Chaussee 149, D-22761 Hamburg, Germany*
[158]*Kavli Institute for Particle Astrophysics and Cosmology, Stanford University, Stanford, CA 94305, USA*
[159]*Kavli Institute for Particle Astrophysics and Cosmology, Department of Physics and SLAC National Accelerator Laboratory, Stanford University, 2575 Sand Hill Road, Menlo Park, CA 94025, USA*
[160]*IPARCOS Institute, Faculty of Physics (UCM), E-28040 Madrid, Spain*
[161]*School of Allied Health Sciences, Kitasato University, Sagamihara, Kanagawa 228-8555, Japan*

[162] *Department of Physics, Yamagata University, Yamagata, Yamagata 990-8560, Japan*
[163] *The Henryk Niewodniczański Institute of Nuclear Physics, Polish Academy of Sciences, ul. Radzikowskiego 152, PL-31-342 Cracow, Poland*
[164] *Faculty of Physics, University of Białystok, ul. K. Ciołkowskiego 1L, PL-15-245 Białystok, Poland*
[165] *Faculty of Engineering, Kanagawa University, 3-27-1 Rokukakubashi, Kanagawa-ku, Yokohama-shi, Kanagawa 221-8686, Japan*
[166] *Institute of Particle & Nuclear Physics, Charles University, V Holešovičkách 2, CZ-180 00 Prague 8, Czech Republic*
[167] *Institute for Space–Earth Environmental Research, Nagoya University, Furo-cho, Chikusa-ku, Nagoya 464-8601, Japan*
[168] *Kobayashi–Maskawa Institute for the Origin of Particles and the Universe, Nagoya University, Furo-cho, Chikusa-ku, Nagoya 464-8602, Japan*
[169] *Graduate School of Technology, Industrial and Social Sciences, Tokushima University, Tokushima 770-8506, Japan*
[170] *University of Pisa, Largo B. Pontecorvo 3, I-56127 Pisa, Italy*
[171] *INAF – Osservatorio Astronomico di Padova, Vicolo dell'Osservatorio 5, I-35122 Padova, Italy*
[172] *INAF – Osservatorio Astronomico di Padova and INFN Sezione di Trieste, gr. coll. Udine, Via delle Scienze 208, I-33100 Udine, Italy*
[173] *Institute for Theoretical Physics and Astrophysics, Universität Würzburg, Campus Hubland Nord, Emil-Fischer-Str. 31, D-97074 Würzburg, Germany*
[174] *Dipartimento di Scienze Fisiche e Chimiche, Università degli Studi dell'Aquila and GSGC-LNGS-INFN, Via Vetoio 1, L'Aquila I-67100, Italy*
[175] *Departamento de Física, Facultad de Ciencias Básicas, Universidad Metropolitana de Ciencias de la Educación, Avenida José Pedro Alessandri 774, CL-7760409 Ñuñoa, Santiago, Chile*
[176] *Instituto de Estudios Astrofísicos, Facultad de Ingeniería y Ciencias, Universidad Diego Portales, Av. Ejército Libertador 441, 8370191 Santiago, Chile*
[177] *Departamento de Astronomía, Universidad de Concepción, Barrio Universitario S/N, CL-8300 Concepción, Chile*
[178] *Hiroshima Astrophysical Science Center, Hiroshima University, Higashi-Hiroshima, Hiroshima 739-8526, Japan*
[179] *Faculty of Engineering, Gifu University, 1-1 Yanagido, Gifu 501-1193, Japan*
[180] *Laboratory for High Energy Physics, École Polytechnique Fédérale, CH-1015 Lausanne, Switzerland*
[181] *Departamento de Física, Universidad de Santiago de Chile (USACH), Av. Victor Jara 3493, CL-9170124 Estación Central, Santiago, Chile*
[182] *Main Astronomical Observatory of the National Academy of Sciences of Ukraine, Zabolotnoho str., 27, UA-03143 Kyiv, Ukraine*
[183] *Faculty of Space Technologies, AGH University of Krakow, Aleja Mickiewicza 30, Kraków PL-30-059, Poland*
[184] *Academic Computer Centre CYFRONET AGH, ul. Nawojki 11, PL-30-950 Kraków, Poland*
[185] *Observatório Nacional, Rio de Janeiro - RJ 20921-400, Brazil*
[186] *Faculty of Electronics and Information Technology, Institute of Electronic Systems, Warsaw University of Technology, Nowowiejska 15/19, PL-00-665 Warsaw, Poland*
[187] *Department of Physical Sciences, Aoyama Gakuin University, Fuchinobe, Sagamihara, Kanagawa 252-5258, Japan*
[188] *School of Physics and Astronomy, Sun Yat-sen University, CN-519000 Zhuhai, China*
[189] *Curtin University, Kent St, Bentley WA 6102, Australia*
[190] *Institute for Nuclear Research and Nuclear Energy, Bulgarian Academy of Sciences, 72 boul. Tsarigradsko chaussee, 1784 Sofia, Bulgaria*
[191] *Port d'Informació Científica, Edifici D, Carrer de l'Albareda, 08193 Bellaterrra (Cerdanyola del Vallès), Spain*
[192] *INAF – Osservatorio Astronomico di Cagliari, Via della Scienza 5, I-09047 Selargius (CA), Italy*
[193] *Kapteyn Astronomical Institute, University of Groningen, Landleven 12, NL-9747 AD, Groningen, the Netherlands*
[194] *Departamento de Física, Universidad Técnica Federico Santa María, Avenida España, 1680 Valparaíso, Chile*

This paper has been typeset from a TEX/LATEX file prepared by the author.